

PROSPECTS FOR HIGGS BOSON & TOP QUARK MEASUREMENTS AND APPLICATIONS OF DIGITAL CALORIMETRY AT FUTURE LINEAR COLLIDERS

A. Winter

*Thesis submitted for the degree of
Doctor of Philosophy*



Particle Physics Group,
School of Physics and Astronomy,
University of Birmingham.

May 24, 2018

ABSTRACT

Within the next few years a decision must be made by the global community on what type of high energy colliders should be built in the post LHC era. Here we present studies showing what might be achieved if a linear lepton collider such as Compact Linear Collider (CLIC) is chosen. Two physics studies are presented showing the precision achievable in the electroweak sector when operating at 1.4 TeV. Firstly the measurement of $\sigma_{H\nu\bar{\nu}} \times BR(H \rightarrow WW^*)$, an integral component for model independent Higgs measurements, is described using the semileptonic decay channel and is shown to yield a statistical precision of 1.3% for 1.5 ab^{-1} of data. A differential measurement of the top quark forward backward asymmetry is also performed as a probe of the electroweak form factors of the $t\bar{t}X$ vertex yielding a statistical precision of $\mathcal{O}(1\%)$ for 1.5 ab^{-1} of data. Lastly, the potential for using a novel design of a Digital Electromagnetic Calorimeter (DECAL) at the International Linear Collider (ILC) is studied showing that an energy resolution of $\frac{\sigma_E}{E} = \frac{16.1\%}{\sqrt{E}} \oplus \frac{0.5\%}{E} \oplus 0.4\%$ can be achieved, similar to what is seen for the standard design choice, when using $30 \mu\text{m}$ pitch pixels with a $12 \mu\text{m}$ epitaxial thickness.

DECLARATION OF AUTHORS CONTRIBUTION

The work presented here has been carried out within the CLIC and Calorimeter for Linear Collider Experiment (CALICE) collaborations however all the work presented here is solely the authors own work unless otherwise stated. The two physics studies presented in Chapters 4 and 5 were performed using the ILCSoft framework used for all analyses at ILC and CLIC and used event samples generated centrally by CLIC, however the reconstruction and event selection techniques used were chosen and implemented by the author. The study related to the Higgs sector has already been published in a paper summarising the potential for Higgs measurements[1] at CLIC and a similar paper showing the potential for top quark measurements that will include the results from Chapter 5 is currently under review[2].

For the work presented in Chapter 6 the DigiMAPS package was used for adding additional levels of realism to the simulation studies. This package was originally developed by Anne-Marie Magnan as part of the CALICE collaboration and was adapted by the author to change how pixel noise was implemented and to allow for variations in the threshold between pixels. This work is in the process of being written into a paper by the author.

ACKNOWLEDGEMENTS

Motto or dedication

Contents

1	Introduction	1
2	Experiments	5
2.1	ILC	6
2.1.1	Energy Staging	7
2.1.2	Beam Production, Acceleration and Focusing	9
2.1.3	Positron Production	10
2.2	CLIC	10
2.2.1	Energy Staging	12
2.2.2	Acceleration Technology	13
2.3	Linear Collider Analysis Framework	15
2.3.1	Event Generation	15
2.3.2	Pandora Particle Flow Algorithm	16
2.4	Detectors	17
2.4.1	ILD	17
2.4.1.1	Vertexing	19
2.4.1.2	Tracking	20
2.4.1.3	Calorimetry	23
2.4.1.4	ECAL	26
2.4.1.5	HCAL	28
2.4.1.6	Muon Detection	28
2.4.1.7	Very Forward Region	29
2.4.2	CLIC ILD	30
3	Theory	31
3.1	The Standard Model	31
3.2	The Higgs Boson and the Origin of Mass	35
3.3	Higgs Measurements at CLIC	37
3.3.1	Higgsstrahlung	38
3.3.2	Model Independent Extraction of Higgs Couplings	39
3.4	Top Quark Physics	44
4	Higgs to WW^* at 1.4 TeV	49
4.1	Event Generation	51
4.2	Event Reconstruction	52
4.2.1	Lepton Identification	53
4.2.2	Jet Finding	54

4.3	Flavour Tagging	57
4.4	Event Selection	58
4.4.1	Boosted Decision Trees	59
4.5	Systematics	67
4.6	Impact on CLIC Higgs Measurements	69
4.7	Conclusion	70
5	Top Physics	72
5.1	Introduction	72
5.2	Event Reconstruction	76
5.2.1	Lepton Finding	76
5.2.2	Fat Jet Finding	81
5.2.2.1	Jet Association	83
5.2.3	Jet Substructure	91
5.2.3.1	N-subjettiness	91
5.2.3.2	Subjet Angular Distributions	94
5.2.3.3	Jet Multiplicity	94
5.2.4	s' Reconstruction	97
5.2.4.1	Transverse/Longitudinal Association	97
5.2.4.2	Analytic Mass Constraint	100
5.2.4.3	Collinearity	101
5.2.4.4	Kinematic Fitting	102
5.2.5	Flavour Tagging	105
5.3	Methods For Calculating A_{FB}^t	107
5.4	Event Selection	110
5.4.1	Preselection	111
5.4.2	Quality Cuts	111
5.4.3	BDT Selection	115
5.5	Extraction of A_{FB}^t and cross section	117
5.6	Systematics	123
5.6.1	Background Normalization	123
5.6.2	Background Shape	124
5.6.3	Luminosity	125
5.6.4	Bias Towards Generator A_{FB}^t	126
5.6.5	Unquantified Effects	130
5.6.6	Summary	132
5.7	Improvements	132
5.8	Conclusions	134
6	Digital Calorimetry	136
6.1	Introduction	136
6.2	Event Generation and Detector Simulation	138
6.3	Pixel Design Optimization	141
6.4	DigiMAPs	149
6.4.1	Pixel Design Optimization Revisited	153
6.5	Future Improvements	158

6.6 Conclusion	159
7 Conclusion	161
.1 Appendix A: Higgs Results	172
Appendices	172
.2 Appendix B: Top Results	175

List of Tables

2.1	ILC Beam Parameters	8
2.2	CLIC beam parameters	11
2.3	Properties of the CLIC vertex detector assuming three pairs of layers [26]	20
3.1	Particles of the Standard Model	32
3.2	Predicted Higgs Coupling Modifications for BSM theories	44
5.1	Top Pair Decay Modes	73
5.2	Samples used in the -80% electron beam polarization study	75
5.3	Samples used in the +80% electron beam polarization study	75
5.4	Methods used for identifying which fat jet corresponds to the hadronically decaying top.	88
5.5	Precision attainable on A_{FB}^t during the -80% electron polarization stage assuming perfect event reconstruction for the simple counting method vs the fit method for extraction	110
5.6	Efficiency for signal and background processes following pre-selection cuts for -80% polarization	112
5.7	Efficiency for signal and background processes following pre-selection cuts for +80% polarization	112
5.8	Efficiency for signal and background processes following pre-selection and quality cuts for -80% polarization.	114
5.9	Efficiency for signal and background processes following pre-selection and quality cuts for +80% polarization.	114
5.10	Efficiency for signal and background processes being classified as $E > 1200$ GeV following all stages of selection, and the expected number of events for 750 fb^{-1} for -80% polarization	118
5.11	Efficiency for signal and background processes being classified as $E > 1200$ GeV following all stages of selection and the expected number of events for 750 fb^{-1} for +80% polarization	119
5.12	Values and statistical uncertainties for A_{FB}^t and cross section as extracted from performing a fit to $\cos \theta$ for each energy and polarization.	122
5.13	Values and statistical uncertainties for A_{FB}^t and cross section as extracted from the alternative version of the analysis performed by Lars Rickard Ström.	123
5.14	Systematic uncertainties for A_{FB}^t and cross section arising from theoretical uncertainties on the background normalization.	124

5.15	Systematic uncertainties for A_{FB}^t and cross section arising from theoretical uncertainties on the background shape.	125
5.16	Systematic uncertainties for A_{FB}^t and cross section arising from finite precision on integrated luminosity.	126
5.17	Systematic uncertainties accounting for bias in A_{FB}^t from signal efficiency corrections	130
5.18	Summary of statistical and systematic uncertainties for both polarizations and all energy ranges	133
5.19	Final summary of the expected precisions attainable from the $t\bar{t}$ analysis.	135
7.1	Final summary of the expected precisions attainable from the $t\bar{t}$ analysis.	162
2	Efficiency for signal and background processes being classified as $900 < E < 1200$ GeV following all stages of selection, and the expected number of events for 750 fb^{-1} for -80% polarization	179
3	Efficiency for signal and background processes being classified as $900 < E < 1200$ GeV following all stages of selection and the expected number of events for 750 fb^{-1} for +80% polarization	180
4	Efficiency for signal and background processes being classified as $400 < E < 900$ GeV following all stages of selection, and the expected number of events for 750 fb^{-1} for -80% polarization	181
5	Efficiency for signal and background processes being classified as $400 < E < 900$ GeV following all stages of selection and the expected number of events for 750 fb^{-1} for +80% polarization	182

List of Figures

2.1	The ILC Experiment	6
2.2	Schematic of the ILC accelerator layout	8
2.3	Superconducting Cavities For The ILC	9
2.4	The CLIC Experiment	11
2.5	Cross Sections For Supersymmetric Processes at CLIC	14
2.6	ILD Detector	18
2.7	ILD Vertex Detector	20
2.8	Silicon Tracking Systems For ILD	22
2.9	ECAL Structure	27
2.10	HCAL Structure	28
3.1	Cross Sections For Higgs Production Mechanisms	37
3.2	The Higgstrahlung Process	38
3.3	Reconstructed recoil mass from Higgsstrahlung process	39
3.4	Expected statistical uncertainties for Higgs measurements at 350GeV at CLIC assuming unpolarised beams	41
3.5	Expected statistical uncertainties for Higgs measurements at 1.4TeV and 3TeV at CLIC assuming unpolarised beams	42
3.6	Expected precision on model independent measurements of the Higgs couplings	42
3.7	Expected precision on model dependent measurements of the Higgs couplings at CLIC	43
3.8	Expected precision on model dependent measurements of the Higgs couplings at CMS	43
3.9	Dominant top production mechanism at electron positron colliders . .	45
3.10	Expected precision on CP conserving electroweak form factors at future colliders	48
4.1	Cross Sections For Higgs Production Mechanisms	50
4.2	Semileptonic decay channel for WW* decays of Higgs produced through WW-fusion	51
4.3	Samples used for the H \rightarrow WW* analysis	52
4.4	Parameters used for loose lepton selection	53
4.5	Jet Reconstruction Optimization	55
4.6	Reconstructed Higgs Mass For Optimum Jet Radius	55
4.7	Reconstructed Higgs Mass	56
4.8	B-Tagging Purity vs Efficiency	57
4.9	Reconstructed Higgs mass for signal and background events	59

4.10	Energy of the hadronically decaying W	60
4.11	Energy of the hadronically decaying W Boson for signal and background events	60
4.12	Number of reconstructed loose selected lepton for signal and background events	61
4.13	Missing energy of signal and background events	61
4.14	Missing energy of signal and $e\gamma$ events	62
4.15	Reconstructed W mass for signal and background events	62
4.16	Preselection efficiencies	63
4.17	Example of a decision tree	63
4.18	Classifier BDT response	65
4.19	Samples Used	67
4.20	Expected precision on input quantites for the Higgs width measurement	70
5.1	Semileptonic $t\bar{t}$ decay	72
5.2	Dominant single top production mode	74
5.3	Charge Tagging Efficiency	77
5.4	Angular dependence of lepton finding for particles vs antiparticles	78
5.5	Lepton Momentum Vs Angle	79
5.6	Lepton efficiency for $ee \rightarrow H\nu\nu, H \rightarrow WW \rightarrow qql\nu$	80
5.7	Charge Tagging Efficiency After 20GeV Lepton Momentum Cut	80
5.8	Separation between W and b jet from top decay	81
5.9	Effect of the Valencia β parameter	83
5.10	Performance of jet finding algorithms	84
5.11	Performance of Valencia algorithm for high energy events	84
5.12	Comparison of reconstructed top decay angle to generator level	85
5.13	Reconstructed fat jet mass	85
5.14	Reconstructed vs generator top decay angles with truth level cuts	87
5.15	Reconstructed $\cos\theta$ distribution for various jet association methods	89
5.16	Mean and width from fitting $\Delta\cos\theta_{Gen.-Reco.}$ to a gaussian	90
5.17	Efficiency for reconstructing the hadronically decaying top in the correct $\cos\theta$ bin	91
5.18	Diagrammatic representation of N-subjettiness	92
5.19	Leptonic fat jet τ_2/τ_1	94
5.20	Angular separation of highest and lowest energy subjets	95
5.21	Jet multiplicity of the hadronic fat jet	95
5.22	Expected $\sqrt{s'}$ spectrum for $t\bar{t}$ at 1.4 TeV	96
5.23	Angular energy distribution of initial state photons	98
5.24	Reconstructed $\sqrt{s'}$ vs generator $\sqrt{s'}$ for transverse/longitudinal association method	99
5.25	Reconstructed $\sqrt{s'}$ vs generator $\sqrt{s'}$ for mass constraint method	99
5.26	Mass of reconstructed leptonic top when using mass constraint method	100
5.27	Collinearity of $t\bar{t}$ pair	103
5.28	Reconstructed $\sqrt{s'}$ vs generator $\sqrt{s'}$ for collinearity method	103
5.29	Reconstructed $\sqrt{s'}$ vs generator $\sqrt{s'}$ for kinematic fit method	105
5.30	B-Tagging Purity vs Efficiency	106

5.31	B-Tagging performance	107
5.32	Predicted forward backward asymmetry as a function of collision energy	108
5.33	Generator level $\cos \theta$ distributions for each energy bin	109
5.34	Effect of quality selection on agreement of $\cos \theta$ reco. vs gen.	115
5.35	Boosted Decision Tree (BDT) performance for all four classifiers . . .	117
5.36	Final corrected angular distributions from which A_{FB}^t and σ_{Total} are extracted	121
5.37	Efficiency for reconstructing signal events in the correct $\cos \theta$ bins . .	127
5.38	Efficiency for reconstructing signal events in the correct $\cos \theta$ bins . .	127
5.39	Correlation between the reconstructed and generator A_{FB}^t for each $\sqrt{s'}$ bin, -80% polarization.	129
6.1	Typical layout of a CMOS sensor	138
6.2	Complimentary Metal-Oxide Semiconductor (CMOS) Monolithic Active Pixel Sensors (MAPS) sensor including deep p well implant to prevent parasitic losses to the PMOS transistor[65]	139
6.3	Example of how EM showers look in a DECAL with $10 \times 10 \mu\text{m}^2$ pixels for various photon energies.	140
6.4	Energy deposited in a $100 \times 100 \mu\text{m}^2$ pitch, 12 μm thick pixel by a 10 GeV photon. The landau fit and resulting choice of threshold are also shown.	141
6.5	Calibration curves describing the relationship between the number of pixel hits observed and the energy of the incident particle for various pixel configurations.	143
6.6	Energy resolution curves describing the variation of the energy resolution with the energy scale	143
6.7	Stochastic term of the energy resolution fits for all pixel configurations	144
6.8	Noise term of the energy resolution fits for all pixel configurations . .	145
6.9	Constant term of the energy resolution fits for all pixel configurations	145
6.10	Pixel occupancy for 100 GeV photons.	146
6.11	Variation in the landau distributions for 10 GeV photons as a function of the pixel pitch. All distributions normalised to unity.	147
6.12	Variation in the landau distributions for 10 GeV photons as a function of the epitaxial thickness. All distributions normalised to unity. . .	147
6.13	Energy resolution for 10 GeV photons.	148
6.14	Energy resolution for 50 GeV photons.	148
6.15	Energy resolution for 250 GeV photons.	149
6.16	Variation in the energy resolution as a function of the threshold applied after each DigiMAPS effect is added. The effects are added sequentially in the order displayed in the legend.	152
6.17	Stochastic term of the energy resolution fits for all pixel configurations when including clustering, noise, dead space and threshold spread. .	154
6.18	Noise term of the energy resolution fits for all pixel configurations when including clustering, noise, dead space and threshold spread. .	154
6.19	Constant term of the energy resolution fits for all pixel configurations when including clustering, noise, dead space and threshold spread. .	155

6.20 Energy resolution for 10 GeV photons after DigiMAPS is applied but without clustering.	155
6.21 Energy resolution for 10 GeV photons after DigiMAPS is applied.	156
6.22 Energy resolution for 50 GeV photons after DigiMAPS is applied.	156
6.23 Energy resolution for 250 GeV photons after DigiMAPS is applied.	157

DEFINITIONS OF ACRONYMS

ATLAS A Toroidal LHC Apparatus

BDS Beam Delivery System

BDT Boosted Decision Tree

BS Beamstrahlung

BSM Beyond the Standard Model

CALICE Calorimeter for Linear Collider Experiment

CDR Conceptual Design Report

CERN European Organisation for Nuclear Research

CLIC Compact Linear Collider

CMOS Complimentary Metal-Oxide Semiconductor

CMS Compact Muon Solenoid

DECAL Digital Electromagnetic Calorimeter

ECAL Electromagnetic Calorimeter

EM Electromagnetic

ETD Endcap Tracking Detector

FCC Future Circular Collider

FTD Forward Tracking Detector

HCAL Hadronic Calorimeter

HL-LHC High Luminosity Large Hadron Collider

ILC International Linear Collider

ILD International Large Detector

IP Interaction Point

ISR Initial State Radiation

LEP Large Electron-Positron Collider

LHC Large Hadron Collider

MAPS Monolithic Active Pixel Sensors

PID Particle ID

PFA Particle Flow Algorithm

PFO Particle Flow Object

QCD Quantum Chromodynamics

RAL Rutherford Appleton Laboratory

RF Radio Frequency

SET Silicon External Tracker

SiD Silicon Detector

SIT Silicon Internal Tracker

SM Standard Model

TDR Technical Design Report

TPC Time Projection Chamber

CHAPTER 1

Introduction

With the expected shutdown of the High Luminosity Large Hadron Collider (HL-LHC) in 2038, and the long time scales associated with the construction of any new colliding facility (~ 10 years), the time for physicists to agree on what experiments should operate in the post Large Hadron Collider (LHC) era is rapidly approaching, with initial decisions expected to take place in the early 2020s. However, following the discovery of a Higgs Boson at the LHC [3, 4], with properties consistent with those predicted by the Standard Model (SM)[5, 6, 7], the particle physics community is left in a situation where there is no definitive course of action through which new physics phenomena might be discovered. There are still many open questions remaining; one clear example being the origin of dark matter, which has been observed to make up $\sim 27\%$ of the universe. Despite being examined through multiple astrophysical observations such as gravitational lensing or galactic rotation curves [8], there is still no experimental evidence in particle physics that clarifies its nature. Other notable examples include the matter-antimatter asymmetry of the universe which

is yet to be reconciled with the levels of CP violation measured in the SM[9] and the Higgs hierarchy problem / fine tuning problem[10] where it is expected that a precise cancellation of quantum corrections is needed to be able to explain the difference in strength between the weak and gravitational forces while accommodating the measured value of the Higgs mass. Currently there is no clear direction for how we might solve these mysteries. As such, there are two main approaches that may be taken.

The first is to continue to push the boundaries of the “energy frontier” to increasingly high levels and look for physics phenomena that are not predicted by the SM. In this scenario the natural option is to build a circular hadron collider, much like the LHC. While hadron collisions result in more complex interactions due to the substructure and strong interaction nature of the initial state, they are well suited for high energy collisions due to the high masses of the accelerated beam particles which reduce the amount of synchrotron radiation emitted, which for a circular trajectory can be written as

$$\Delta E(\text{GeV})/\text{turn} = \frac{k}{\rho(m)} \frac{E^4(\text{GeV})}{m_e^4(\text{GeV})}, \quad (1.1)$$

where ΔE is the energy lost, E is particle energy, ρ is radius of curvature, m_e is mass and k is a constant.

Pushing the energy frontier has the appeal that it allows direct detection of particles at new energy scales and is supported by the fact that many Beyond the Standard Model (BSM) models such as supersymmetry[10] rely on new particles appearing in the multiTeV energy range, however it does have drawbacks and risks. Due to the composite structure of hadrons, they provide centre-of-mass energies that are often significantly below the nominal collision energy of the two initial state beams and so the precise energy at which the hard interactions take place is challenging to measure. This limits the type of measurement that can be performed as the initial state of the interaction is poorly defined and so all measurements must rely on measurement of the final state particles. This increases the impact of un-

certainties introduced by detector acceptances and resolutions and makes it highly challenging to identify particles that cannot be directly observed by the detector e.g. neutrino/ dark matter candidates. Due to fragmentation of the hadrons, there are also significant Quantum Chromodynamics (QCD) background jets produced. the cross-section of which can be orders of magnitude larger than that of potential new signal channels. While these do make measurements more challenging, the real risk with pushing the energy frontier is that the constraints on the scale of at which new physics might be observed are currently very poor[11]. This makes it challenging to choose the collision energy for any future collider as choosing too low an energy could result in no new phenomena being seen.

The second option is to advance in the “precision frontier” and search for small deviations from the SM in established observables, or by measuring “ultra rare” decays for the first time[12]. In this case the more natural choice is to use a lepton collider as annihilation of fundamental rather than composite particles means the initial conditions of the interaction can be known to a high precision, determined entirely by the quality of the colliding beams. For leptons it is also possible to produce polarised beams which opens up a new range of potential measurements when examining interactions that couple differently to left and right handed particles. Doing this, areas of the SM that are less well measured such as the Higgs and Top quark sectors can be probed for evidence of physics beyond the SM. The worst case scenario for a lepton collider is to simply reinforce the SM without seeing any new phenomena, however even in this case the significantly higher levels of precision on many of the SM parameters will be beneficial for constraining BSM theories and reducing systematic uncertainties on measurements being made at other future colliders.

While optimised for precise measurements of the SM, lepton colliders also provide opportunities for both direct and indirect discoveries of new physics through channels that are either unavailable at hadron colliders or that are challenging due to the QCD backgrounds. The main drawback of colliding leptons is that currently the only viable option is to use electrons and positrons (though there is effort underway to

use muons [13]) which have extremely low masses and so produce considerable levels of synchotron radiation (10^{13} as much as protons) when used in a circular collider. The usual solution to this is to use a linear collider instead. This reduces losses from synchotron radiation, however it limits the maximum collision energy that can be achieved as the path over which the particles can be accelerated is limited by the mean accelerating gradient of the active components of the machine and the length of the accelerator, which is itself limited by the increasing cost of extending the footprint of the machine. It is worth noting however, that for leptons each collision takes place at twice the beam energy, except for the fraction that are subject to radiative losses in the initial state as discussed in Chapter 2.

Considerable work has already been carried out into designing both high energy and high precision colliders. On the high energy side is the Future Circular Collider (FCC), a 100 TeV circular proton collider proposed as a project based at the European Organisation for Nuclear Research (CERN). It is possible to also use the tunnel constructed for this machine to accommodate an e^+e^- collider operating above the Higgs threshold so as to act as a “Higgs factory”. On the precision side there are multiple proposed projects, however the most mature of these are the linear electron-positron colliders: CLIC [14] and ILC [15]. The ILC is a 500 GeV collider proposed as a joint endeavour between the Japanese government and the international community while CLIC is a multi-TeV machine being proposed by CERN. Due to the large cost of these devices it unlikely that CERN would build both FCC and CLIC together.

The focus of this thesis will be on the prospects of the proposed high precision colliders. In particular we discuss the prospects for measuring properties of the Higgs boson and top quark at CLIC, the properties of which are both relatively less well known when compared to the other particles of the SM. The physics studies are complemented by detailed design investigations for a digital calorimeter based on CMOS MAPS technology for use in future detectors as an extremely high granularity Electromagnetic Calorimeter (ECAL).

CHAPTER 2

Experiments

There are many possible designs for future lepton colliders [16, 17, 18] however here we focus on the two most developed projects, CLIC and ILC. Both projects are linear colliders which propose using electron-positron collisions and had their origins over twenty years ago, though ILC is currently the more mature design of the two. We will also discuss the detectors proposed for both experiments. ILC currently has two detector concepts being developed, the International Large Detector (ILD) and Silicon Detector (SiD), which will be operated in a “push-pull” scheme in which both detectors are periodically moved to alternate which detector is placed in the path of the beams. This is necessary as there is only one interaction point at a linear collider. Having two detectors has the advantage that any results from one detector can be independently tested by the second to help reduce systematic bias, however it comes with the penalty that each detector will only be able to take data half of the time and the process of moving the detectors in and out is lengthy (~ 3 days) resulting in reduced time for data taking for the experiment. CLIC intends to

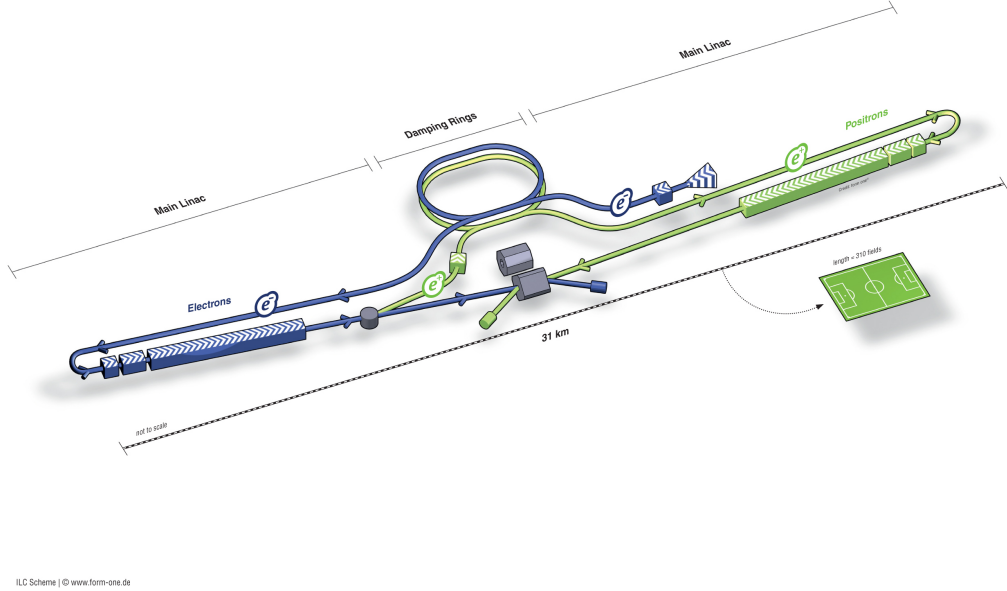


Figure 2.1: The ILC Collider[19]

operate with only one detector, a variation of the ILD developed for ILC, optimised for its more challenging beam conditions.

2.1 ILC

The ILC[19] (Figure 2.1) is a proposed experiment consisting of a 31km e^+e^- collider to be built in Kitakami in the northern region of Japan. The current construction schedule anticipates the experiment will be finished in the mid 2020s with a cost of the order £6 billion and will run for approximately 20 years. However, until funding is secured for the experiment this is only speculative. The ILC Technical Design Report (TDR) [19] was released in 2013 and gives a full description of the experiments' baseline design. Both of the detectors and the accelerator are still in the process of being refined, despite the detail of the TDR. As such the specifications described here are all subject to change.

2.1.1 Energy Staging

The ILC will first be built with a maximum collision energy of 250 GeV and the potential for a later upgrade to 1 TeV which would require doubling the length of the machine to 62 km. Whether the 1 TeV upgrade is necessary will largely be determined by the results of the LHC experiments; if any new physics is discovered above 500 GeV then the 1 TeV upgrade could be essential to characterise it. Assuming the 1 TeV upgrade is realised the energy staging will be as described below.

The first three years will involve the ILC running at an energy of 250 GeV and taking 250 fb^{-1} of data. The main aim at this stage will be to measure the Higgs mass and ZH cross section from the Higgsstrahlung process as described in Chapter 3 to allow model independent measurements of the Higgs couplings to be performed.

For the following three years, the collider will then run at 500 GeV and will accumulate a further 500 fb^{-1} of data. The main aims here will be to measure the HWW coupling, the total Higgs width and the absolute Higgs couplings to fermions. At this energy, measurements of top physics will also be possible including the top forward-backward asymmetry. Outside of the Higgs sector, the top quark is perhaps the least well measured of the SM particles and so provides another area in which to look for deviations in its predictions.

After this there will be an upgrade to 1 TeV followed by another three years of data taking accumulating 1000 fb^{-1} of data. The aim of running at this high energy will be to search for new particles such as dark matter candidates and supersymmetric particles while improving the precision of the measurements performed at the lower energies. If one of these (or something entirely new) has already been discovered at the LHC then the choice of energy could be tuned to match the scale of the newly discovered physics.

After this the collider will undergo a high luminosity upgrade and will run at the same energies for the same time periods for another 9 year, recording 900, 1100 and 1500 fb^{-1} at the respective energies. This will allow for a further increase in

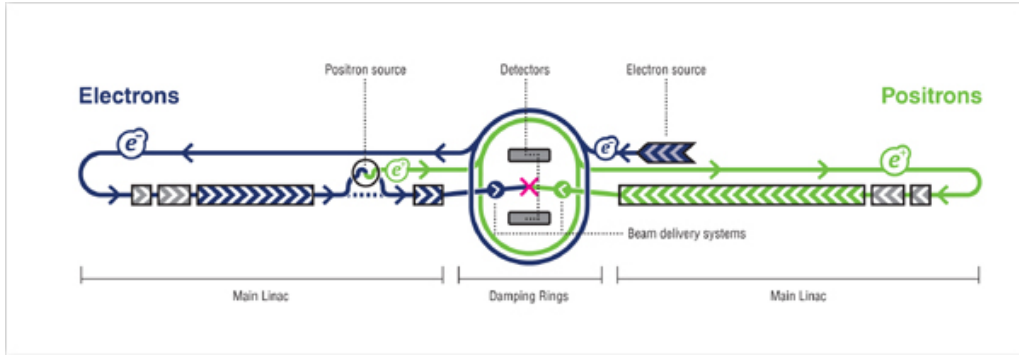


Figure 2.2: A simplified schematic of the ILC[19]

Table 2.1: ILC Beam Parameters[19]

Parameter	Symbol	Unit	Stage 1	Stage 2
Centre-of-mass energy	\sqrt{s}	GeV	250	500
Repetition frequency	f_{rep}	Hz	5	5
Number of bunches per train	n_b		1312	1312
Number of particles per bunch	N	10^{10}	2.0	2.0
Bunch separation	Δt_b	ns	554	554
Accelerating gradient	G	MV/m	14.7	31.5
Electron Polarization	P_-	%	80	80
Positron Polarization	P_+	%	30	30
Total luminosity	\mathcal{L}	$10^{34} \text{ cm}^{-2}\text{s}^{-1}$	0.75	1.8
Luminosity above 99% of \sqrt{s}	$\mathcal{L}_{0.01}/\mathcal{L}$		87.1%	58.3%
IP RMS beam size	σ_x/σ_y	nm	729.0/7.7	474/5.9
RMS Bunch length	σ_z	mm	0.3	0.3
Horizontal emittance	ϵ_x	μm	10	10
Vertical emittance	ϵ_y	nm	35	35
Estimated power consumption	P_{AC}	MW	122	163

the precision of all measurements taken during the lower luminosity run. While the TDR proposes the above run scheme for the ILC there is still debate about what energies should be used, including running at 90 GeV (the Z mass) to gain precision measurements of the Z boson, 350 GeV (the top production threshold) to better measure the properties of the top quark or to simply only run at 250 GeV to provide precision Higgs measurements for minimal cost.



Figure 2.3: A 1.3GHz Superconducting Niobium Radio Frequency Cavity [19]

2.1.2 Beam Production, Acceleration and Focusing

A simplified schematic of the ILC machine layout is shown above in Figure 2.2 while a summary of the key beam parameters is shown in Table 2.1. The first stage of the acceleration process is the production of electrons. This is done using the photoelectric effect by firing photons onto a GaAs target to produce photoelectrons. These electrons then enter a 3.2 km long damping ring which accelerates the beam up to 15 GeV. The primary purpose of the damping ring is to produce a homogeneous beam of electrons with a small spread in the phase space of each bunch. After the damping ring the electrons enter into a two-stage bunch compressor which separates the electron beam into \sim 1300 bunches, each containing 2×10^{10} electrons, with each bunch being separated by 554 ns and a maximum beam pulse length of \sim 1.6 ms. The overall intended collision rate of these so called “bunch trains” is 5 Hz, which means that the time within which collisions occur will take place is less than 1% of the overall duty cycle of the accelerator. This has important consequences for the detector design as it means the detectors have approximately 200 ms in which to process data before the next bunch train arrives. As the detectors do not need to be operating for 99% of the time, it is considerably easier to cool them meaning the material budget for the cooling systems within them can be greatly reduced. Following the bunch compression the electrons enter the main 11 km linac where they are accelerated up to the nominal beam energy using 7,400 1.3 GHz superconducting niobium Radio Frequency (RF) cavities (see Figure 2.3).

The RF cavities are kept at a temperature of 2K and act to produce an average accelerating gradient of up to 31.5MV/m (14.7MV/m for the 250GeV stage.) The final stage before the collision is the Beam Delivery System (BDS) which primarily acts to transport the beam from the end of the main accelerating linac to the interaction

point, as well as to compress the beam into a “ribbon” shape with a cross-section of $7.7 \times 729.0 \text{ nm}^2$ while also handling the beam monitoring. The ribbon shape is designed to reduce Beamstrahlung (BS) radiation from beam interactions while giving a small enough cross section that a high instantaneous luminosity can be achieved. Following the BDS the beam finally enters the detector and collides with the opposing positron beam at a crossing angle of 14 mrad then exits into the beam dump system which quenches what is left of the beam.

2.1.3 Positron Production

Positrons are produced at the ILC by tapping off energy from the electron beam after it has been accelerated by the main linac. The electron beam is passed through an undulator which causes the electrons to emit synchrotron radiation in the form of 10-30 MeV photons by forcing the beam to take a rapidly varying path in the plane transverse to its direction of motion. The photons are incident on a Titanium alloy target and produce electron positron pairs. The electrons and positrons are then separated, the electrons are dumped while the positrons are transported to a damping ring and undergo the same stages of acceleration and shaping as described above for the electrons.

2.2 CLIC

CLIC will be an experiment based at CERN which consists of a 42 km accelerator at the main CERN site in Geneva (Figure 2.4.). Despite being named as compact, CLIC is actually longer than the initial 250 GeV ILC. The reason for this naming is that CLIC has a much higher accelerating gradient (100 MeV/m) compared to ILC and so provides a much higher energy per length. The expected build date for CLIC is still uncertain and likely to be no earlier than 2030 as the accelerating technology required for CLIC is less developed than that used by ILC. This difference

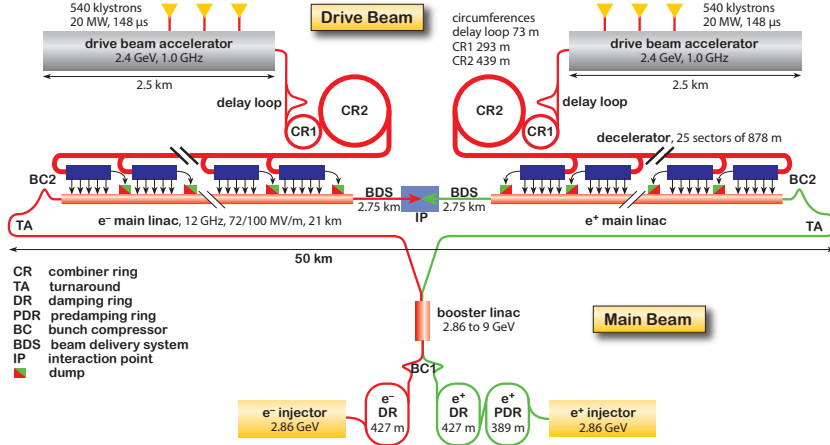


Figure 2.4: The CLIC Collider. Layout for the CLIC accelerator at 3 TeV. For the lowest energy stage there will only be one drive beam constructed which will power both main beams[20]

Table 2.2: Parameters for the CLIC energy stages. The power consumptions for the 1.5 and 3 TeV stages are from the CDR; depending on the details of the upgrade they can change at the percent level [14].

Parameter	Symbol	Unit	Stage 1	Stage 2	Stage 3
Centre-of-mass energy	\sqrt{s}	GeV	380	1500	3000
Repetition frequency	f_{rep}	Hz	50	50	50
Number of bunches per train	n_b		352	312	312
Bunch separation	Δt	ns	0.5	0.5	0.5
Pulse length	τ_{RF}	ns	244	244	244
Accelerating gradient	G	MV/m	72	72/100	72/100
Total luminosity	\mathcal{L}	$10^{34} \text{ cm}^{-2}\text{s}^{-1}$	1.5	3.7	5.9
Luminosity above 99% of \sqrt{s}	$\mathcal{L}_{0.01}$	$10^{34} \text{ cm}^{-2}\text{s}^{-1}$	0.9	1.4	2
Main tunnel length		km	11.4	29.0	50.1
Number of particles per bunch	N	10^9	5.2	3.7	3.7
Bunch length	σ_z	μm	70	44	44
IP beam size	σ_x/σ_y	nm	149/2.9	$\sim 60/1.5$	$\sim 40/1$
Normalised emittance (end of linac)	ϵ_x/ϵ_y	nm	920/20	660/20	660/20
Normalised emittance (at IP)	ϵ_x/ϵ_y	nm	950/30	—	—
Estimated power consumption	P_{wall}	MW	252	364	589

in the maturity of the two experiments can be seen from the fact that the ILC has released its TDR while the most comprehensive document for the CLIC project is still its Conceptual Design Report (CDR) [20]. Updates on this document have been provided in the New Baseline Report [14] released in 2016 and details discussed in the following originate from these two documents.

Overall the design for CLIC is relatively similar in layout to the ILC but with a few changes. Positron production at CLIC takes place independent of the main electron beam, though they are still produced via the same mechanism as before. The BDS still compresses the beam into a ribbon shape to give it a small cross-section and reduced BS at the interaction point, however the aspect ratio in the transverse plane is slightly reduced compared to ILC. This results in larger contributions from beam photon radiations at CLIC. The collision rate at CLIC is significantly higher as it aims to be a high luminosity device—the collision rate will be 50 Hz with 354 bunches per pulse with a separation of just 0.56 ns. This means that CLIC will have a significantly higher duty cycle which will make cooling of the detectors harder and make data processing close to the detector front end more of a challenge. A summary of the beam parameters for CLIC is shown in Table 2.2. While these differences are important, the most significant changes are in the energy staging and acceleration technology used at CLIC (see Section 2.2.2.)

2.2.1 Energy Staging

CLIC will operate at three energy stages: 380 GeV, 1.5 TeV and 3 TeV collecting 500 fb^{-1} , 1.5 ab^{-1} and 2 ab^{-1} of data respectively. During the running of the 380 GeV energy stage, construction of the 1.5 TeV structure will be carried out (and so on for the 1.5 TeV and 3 TeV scales) to reduce the delay between operation at successive energy stages.

The 380 GeV energy scale is chosen as it is above the $t\bar{t}$ production threshold and provides a significant cross section for many channels involving the top quark. This

stage is also supplemented by a series of 10 measurements around the $t\bar{t}$ threshold taking 10 fb^{-1} each with the aim of measuring the top mass and width from the line shape of the $t\bar{t}$ production cross section at threshold. The 380 GeV stage will also be used to provide measurements of the higgs boson similar to those performed at ILC during its two lower energy stages.

The 1.5 TeV energy stage provides the ability to further study the top and Higgs in more detail with several new channels becoming significant e.g top Yukawa coupling, Higgs self-coupling, while the 3 TeV stage pushes the energy frontier allowing the possibility of direct detection of new physics at the multi-TeV scale. The choice of 3 TeV is based upon certain models of supersymmetry which predict new particles to exist at this energy (see Figure 2.5).

For clarification it should be stated that for many years the proposed scheme for CLIC was actually to operate at 500 GeV, 1.4 TeV and 3 TeV. These were updated to provide better precision on measurements of the top quark during the lowest energy stage ($t\bar{t}$ production threshold is ~ 350 GeV) and improved precision on the Higgs self-coupling during the second stage. It is important to be aware of these changes as the studies presented in chapters 4 and 5 were carried out at 1.4 TeV assuming the original energy staging, however no qualitative change in the conclusions are expected as a result of this change.

2.2.2 Acceleration Technology

Unlike ILC, the acceleration technology will use two beams of electrons— referred to as the main beam and the drive beam— rather than just one main accelerated beam. The drive beam is accelerated using standard RF accelerating technology (klystrons), but not superconducting, to accelerate bunches of electrons to 2.75 GeV. These bunches then enter a series of delay/control rings which are designed such that the electrons within them get combined with the new electrons being added from the drive beam accelerator to build up a large number of low energy electrons

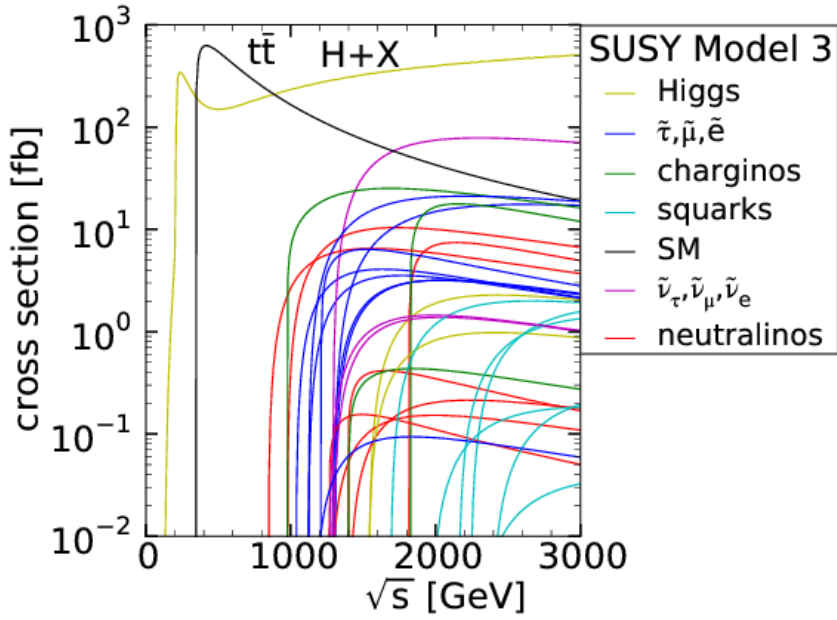


Figure 2.5: Cross sections for production of various supersymmetric particles at an e^+e^- collider as a function of centre of mass energy[20].

which combined carry a large amount of energy. The energy from this high-current beam is then used to drive the main beam. This is done by rapidly decelerating the drive beam electrons down to 10% of their initial energy and using the resulting RF produced to accelerate the smaller number of electrons in the main beam resulting in a rapid acceleration. The main beam is then used to supply collisions. Overall the result is that the machine is simply acting as a novel form of transformer, converting a high current, low energy beam of electrons into a lower current, high energy beam. This approach allows for very high accelerating gradients but has the disadvantage that in approximately 1% of events the sudden input of energy from the drive beam can cause electrical breakdowns in the main beam cavity, which disrupt the alignment and structure of the main beam making them unsuitable for use.

2.3 Linear Collider Analysis Framework

A common framework known as ILCSoft is used for event simulation, reconstruction and analysis. It has been developed for both ILC and CLIC to allow sharing of techniques between the two experiments. Here we will provide an overview of the key packages used.

2.3.1 Event Generation

Event generation is performed using an external package called WHIZARD [21]. WHIZARD itself handles most of the event generation such as the calculation of hard matrix elements, phase space integration and accounting for interference between processes, however for certain aspects it relies on additional packages. The most relevant of these are tau decays which are handled by TAUOLA[22] and hadronization which is handled by PYTHIA[23]. Unfortunately no other hadronization package is available within WHIZARD which makes it challenging to evaluate systematic uncertainties arising from the modelling of jets of hadrons. The output from WHIZARD is a series of four momenta for all the particles produced in the collisions. These are then passed to a package called MOKKA which acts as an interface to GEANT4[24]. Within MOKKA, the geometry of each subsystem within the overall detector, the interaction of the particles with the material of the detector, and the response of the detector to these energy deposits is modelled. These are then finally passed on to the ILCSoft reconstruction package MARLIN in which digitisation of the hits and track reconstruction occur to produce realistic outputs from the detector. At this stage $\gamma\gamma \rightarrow$ hadron beam backgrounds are overlayed on the events assuming a mean rate of 1.6 events per bunch crossing.

2.3.2 Pandora Particle Flow Algorithm

Pandora[25] is a Particle Flow Algorithm used at linear colliders which allows an increased level of precision from detector measurements. The underlying principle behind particle flow is to always use the most precise detector component for performing energy measurements where possible. Typical values for energy resolutions for a charged particle in the main detector components are $\sigma(\Delta p_T/p_T^2) < 2 \times 10^{-5}$ GeV $^{-1}$ in the tracker, $\sigma_E = 0.15 \times \sqrt{E}$ in the ECAL and $\sigma_E = 0.55 \times \sqrt{E}$ in the Hadronic Calorimeter (HCAL). For a typical jet the composition will usually be $\sim 60\%$ charged hadrons, 30% photons and 10% hadrons. Traditionally for measuring the energy in a jet one would simply sum the deposits in both calorimeters resulting in a relatively poor energy resolution of $\sim 60\%/\sqrt{E}$ due to the large component being measured in the HCAL. If one can measure the charge hadron component in the tracker instead, this performance can be vastly improved to $\sim 20\%/\sqrt{E}$. In order to be able to reach this performance, accurate association of tracks with deposits in the calorimeters is crucial. This is achieved by having a high granularity calorimeter and a high spatial resolution for the tracker. In practice however, even with a well-designed detector, the particle flow algorithm can still fail to reconstruct the correct energy due to ambiguities referred to as “confusion”. For example, if a photon enters the calorimeter near to a charged hadron, it is possible that the two will not be resolved and the energy identified from just using the track will neglect the contribution from the photon. Energy can also be overestimated in cases where a charged hadron showers in such a way that it looks like two separate calorimeter deposits which results in part of the shower being identified as a neutral hadron and the other fragment being associated with the track. One of the main design aims of the detectors for ILC and CLIC will be to try and minimise these confusion effects.

2.4 Detectors

The ILC has been designed with the intention of having two unique detectors so that results can be validated by cross-checking between the two detectors. However, because ILC is a linear collider it is only feasible to have one interaction point and as a result the beam time will have to be shared between the detectors. This will be done using a 'push-pull' design in which both detectors are placed on a single platform at the interaction point which can be moved back and forth to position the desired detector in the path of the beams. While having two detectors is certainly desirable as it allows the gathering of two independent sets of results for the collider and the continued taking of results when one of the detectors requires maintenance, it also has disadvantages as it means an increase in the dead time of the machine (as swapping the detectors is a slow process taking several days which will be done multiple times a year) and an increase in the cost of the overall science project. As a result the possibility of using only one detector is still being considered as a potential option. The possibility of splitting the main beam and having two IPs has also being proposed so that both detectors could be used without the need to physically move them, however this would be expensive as extra tunnels would have to be built to accomodate this and there would also be a potential reduction in the beam quality from additional synchrotron radiation when directing the beam towards each experiment. The studies presented in this thesis are based on simulations of only one of these detectors, ILD[26], and as such we will not give details of the alternative: SiD[27].

2.4.1 ILD

The ILD (shown in Figure 2.6) is a general purpose detector which is cylindrical in design with radius 8m and length 14m. The different sub-detectors are arranged in a concentric manner in the main barrel of the detector, and are positioned with the vertexing technology closest to the beamline, followed by trackers, then electromag-

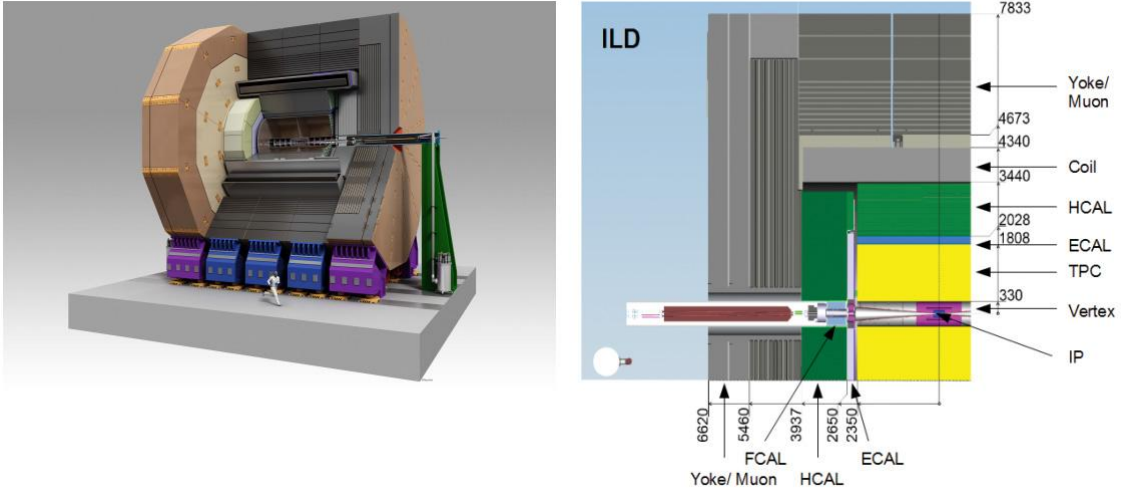


Figure 2.6: The International Large Detector Concept (left). Schematic of the ILD showing the key components in a one-quarter view of a vertical section of the detector (right). Dimensions are given in mm [15]. The z-axis is defined to be that parallel to the beam pipe.

netic and hadronic calorimeters, then the magnetic field coils which supply a 3.5T B-field and finally muon/tail catchers. The detector has two endcaps with a similar layer structure at each end of the barrel creating a hermetic design.

In order to provide precision measurements of the various processes proposed in the ILC and CLIC physics schemes, there are several strict requirements imposed upon the performance of the detector:

- **Momentum Resolution:** $\sigma(\Delta p_T/p_T^2) < 2 \times 10^{-5} \text{ GeV}^{-1}$, key for precision Higgs recoil mass measurements.
- **Jet Energy Resolution:** $\sigma_E/E \sim 3-4\%$, allows separation of hadronic W/Z decays.
- **Impact Parameter Resolution:** $\sigma_b < 5 \oplus 10 \times (p \sin^{\frac{3}{2}} \theta)^{-1} \mu m$, allows accurate flavour tagging for short lived particles.
- **Hermetic Coverage:** Needed for processes with a strong angular dependence or differential cross-sections that peak close to the beam axis or to establish physics signals that have a distinctive missing energy component due to either

neutrinos or other long-lived/non-interacting particles.

Detailed specifications for the detector can be found in the ILD Letter of Intent [26]. Here we will give a brief overview of the key components, their functions, and the methods used for making the most of the information they provide.

2.4.1.1 Vertexing

The vertexing technology is used to determine the presence of b and c quarks. These are typically found in short lived bound states (e.g B mesons $\tau \sim 10^{-12}$ s) and so decay close to the beamline before they can reach the trackers or calorimeters. As such, the vertexers are placed extremely close to the beamline and work by looking for displaced vertices from the initial Interaction Point (IP) which correspond to the point at which the heavy flavour paricles decayed. Due to their proximity to the beam line it is always necessary for the vertex detectors to be radiation hard as they are exposed to stray high energy particles from the beam. The vertexers also provide spatial point measurements that can be used alongside the main trackers for charged particle track reconstruction and so are required to be highly granular to separate particles that have had very little time to spread out since the IP. The design for the vertex detectors is yet to be finalised as there are numerous competing technologies under consideration, but the target performance[19] is to achieve a track impact parameter resolution of

$$\sigma_b < 5 \oplus \frac{10}{p \sin^{\frac{3}{2}} \theta} \mu m \quad (2.1)$$

where p is the track momentum in GeV, θ is the angle between the track and the vertex detector plane and the first and second terms describe contributions from the transverse impact parameter resolution and multiple scattering effects respectively. In practice it is found that to achieve this impact parameter resolution a spatial resolution of at least 3 μm is required. As well as achieving a sufficienctly good

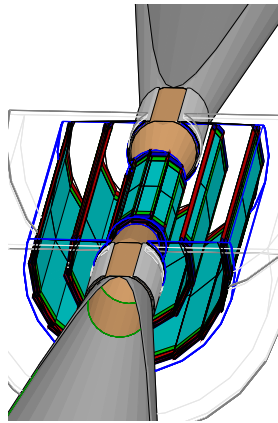


Figure 2.7: Proposed vertex detector geometry for ILD [26]

Table 2.3: Properties of the CLIC vertex detector assuming three pairs of layers [26]

layer	radius, r [mm]	ladder length [mm]	read-out time [μs]
1	16.0	125.0	25-50
2	18.0	125.0	25-50
3	37.0	250.0	100-200
4	39.0	250.0	100-200
5	58.0	250.0	100-200
6	60.0	250.0	100-200

impact parameter resolution, the vertexing detectors are also required to have sufficient granularity and low enough occupancy rates to allow separation of individual tracks passing through the detector. The material budget of the whole vertex and tracking detector systems is less than one radiation length to avoid unwanted production of electromagnetic showers prior to the ECAL. The detector layout used for the baseline studies in the ILD TDR assumes six layers of $50\mu\text{m}$ thick silicon pixels arranged in pairs. The layout and details of the structure are shown in more detail in Figure 2.7 and Table 2.3.

2.4.1.2 Tracking

Tracking in ILD is performed by multiple subsystems. We have already discussed the vertexing systems which act as trackers for low transverse momentum and short lived

particles, however the majority of the tracking is performed by a large Time Projection Chamber (TPC). This is a large gas filled cylinder extending from $r=395$ mm to $r=1739$ mm with an electric field applied parallel to the beam direction and readout electronics at each end of the cylinder on the endcaps. As particles pass through the gas, they ionize it producing charged particles. The electric field then causes these particles to drift to each end of the detector where they are collected by the electronics. By measuring the transverse position and time at which the charged particles arrive, the track of the original ionizing particle can be reconstructed. A magnetic field is also generated across the chamber to deflect the charged particles so that the momentum and charge of the particle can be determined. The magnetic field used in the ILD has a strength of 3.5T and is generated by a superconducting solenoid located outside the calorimeters to minimize the material in front of the calorimeters. The use of a TPC provides several benefits over alternative technologies such as silicon tracking (the technology used in the SiD tracker). Because the ionization occurs across the whole track, it is possible to reconstruct the path of particles from numerous spatial points to provide a precise measurement of the path taken. This is not the case for a silicon tracker where the number of data points is proportional to the number of tracking layers present, however this is compensated for by the fact silicon trackers typically have a higher spatial resolution on each point ($\sim 1 \mu\text{m}$) compared to TPCs ($\sim 1 \text{ mm}$). TPCs also benefit from having a low material budget compared to silicon trackers. In ILD the gas used will be Ar:CH₄:CO₂ (95:3:2) which gives a material budget of $\sim 0.04(0.15)X_0$ radially(longitudinally.) The choice of readout technology is yet to be finalised with several options being pursued (Micro-Pattern Gas Detectors, MicroMegas[28] and GEM[29]) however in all cases it is expected that there will be 10^6 channels of dimension $\sim 1 \times 6 \text{ mm}^2$. This system will allow a single point resolution of $<100 \mu\text{m}$ (0.5 mm) and two-hit resolution of 2 mm (6 mm) in the x-y (r-z) planes, and a resolution of 5% on dE/dx.

The TPC is supplemented by a series of silicon based tracking systems which provide high spatial resolution points at the entrance and exit of the TPC. This allows for an improved momentum resolution, improves the ability to correctly associate

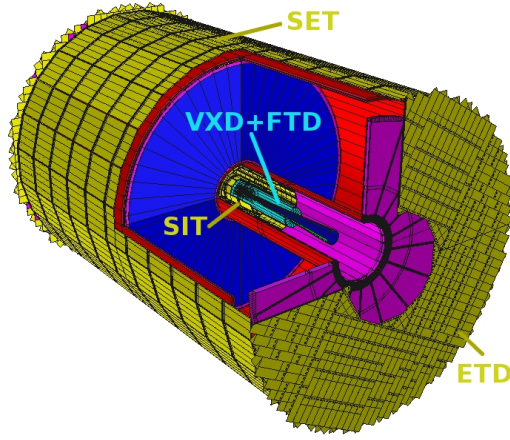


Figure 2.8: Silicon Tracking Systems For ILD [26]

tracks with calorimeter deposits in the Particle Flow Algorithm (PFA)s, provides time stamping for bunch tagging and assists in calibration of the TPC. These additional subdetector systems come in four parts. In the barrel region, between the vertex detector and the TPC lies the Silicon Internal Tracker (SIT) which contributes up to two high spatial resolution points at $r = 165$ mm and $r=309$ mm, while between the TPC and the ECAL lies the Silicon External Tracker (SET) which provides a single space point at $r=1844$ mm. Both of these systems are based on double sided silicon microstrips and provide a resolution of $\sim 50 \mu\text{m}$. The Forward Tracking Detector (FTD) covers the very forward region of the detector down to 0.15 radians and consists of seven disks positioned in the innermost tracking region, the first three using silicon pixels and the end four using silicon microstrips. The Endcap Tracking Detector (ETD) is similar in structure to the SET but is positioned outside the TPC endcaps rather than the barrel to provide high spatial resolution for particles exiting the tracker into the endcap calorimeters. The positioning of all these subdetector systems can be seen in Figure 2.8.

The combined performance of the vertexer, TPC and silicon tracking systems gives a momentum resolution of $\sigma(\Delta p_T/p_T^2) < 2 \times 10^{-5} \text{ GeV}^{-1}$ and a tracking coverage extending down to $\cos \theta < 0.996$.

2.4.1.3 Calorimetry

The function of calorimeters is to measure the energy of particles. As the way that particles interact depends on the type of particle involved, the calorimeters are usually split into two sections, the ECAL and HCAL, which are designed to interact with electromagnetic particles (electron, photons) and hadrons respectively. As we will later be presenting work on a proposed novel design for a so-called DECAL, it is pertinent to discuss in greater detail the relevant processes and terminology involved in electromagentic calorimetry to understand the limitations of current ECAL technologies and how the DECAL might improve upon them.

When a high energy electron interacts with matter it will typically radiate a photon via bremsstrahlung. In the presence of the electric field of a nucleus, this photon can then produce an electron-positron pair, each of which will in turn radiate further photons. This cascade process results in the formation of what is referred to as an electromagnetic shower. The shower will continue to develop until the energy of the shower particles reaches a critical value, E_C , at which the energy losses of the particle begin to be dominated by ionization rather than bremsstrahlung. The development of the electromagnetic shower can be characterised using several parameters. The most commonly used of these is the the radiation length, χ_0 , which is defined as the distance an electron can travel through a material before its energy has reduced by a factor of 1/e via bremsstrahlung (or equivalently to 7/9 the mean free path for pair production of a photon). The radiation length can be expressed as a function of a materials nuclear parameters according to the parameterisation [30]:

$$\chi_0 = \frac{kA}{Z(Z+1) \ln 287/\sqrt{Z}}, \quad (2.2)$$

where k is a constant equal to 716 gcm⁻², A is atomic mass, and Z is atomic number.

For the purposes of designing a detector, perhaps the most relevant parameters are

those related to the size of the showers as these determine the dimensions required for the calorimeter to contain the shower. The longitudinal detector requirements are decided by the rate of energy loss for a particle which is given by the Bethe-Bloch equation which can be simplified to [31]:

$$\frac{dE}{dx} = E_0 b \frac{(bx)^{a-1} e^(-bx)}{\Gamma(a)}, \quad (2.3)$$

where x is the material depth in units of χ_0 , E_0 is the initial energy of the particle, and a and b are properties of the absorbing material. The exponential term means that it is typically not possible to capture 100% of the energy in a shower, instead an acceptable level of loss must be decided and the detector designed accordingly. For example, a typical energy scale for CLIC would be ~ 100 GeV. For a working point of 5% loss a calorimeter depth of $\sim 17 \chi_0$ is sufficient, while for an improved performance of just 1% loss a depth of $\sim 20 \chi_0$ is required. The transverse profile of the shower is described by the Moliere radius, the radius in which 90% of a particles energy will be deposited:

$$R_M = \frac{21\text{MeV}}{E_c} \chi_0 \quad (2.4)$$

In general, it is necessary to have a Moliere radius that is smaller than the typical separation of particles produced in a collision to avoid overlapping of showers. For ILD this is especially true where Pandora PFA relies on accurate association of tracks to calorimeter deposits which is only possible if the deposits from nearby particles can be distinguished.

For ILD the ECAL and HCAL are both sampling calorimeters. This means that the structure is divided into layers of two alternating materials known as the absorber and active material. The absorber is typically a thick piece of high Z material that acts to initiate an Electromagnetic (EM) shower. The active material is then a thin low Z material that is easily ionizable and so collects charge deposited from

the shower. The active layer will then be instrumented to collect and readout the charge deposited within it. In order to reconstruct the energy of the initial particle that produced the shower, the energy deposited in the active layers must be scaled by the expected ratio of the energy deposited in the calorimeter as a whole to that deposited in the active layers. The scale factors will usually be determined as part of a calibration procedure for the detector in which muons are passed through each layer. The application of these scale factors introduces an uncertainty in the reconstructed energy as they represent an average scale correction, whereas the actual ratio of the energy deposited in the active and absorbing layers will be determined by additional factors that cannot be easily measured. One example would be the path taken by the particle which can change the relative distance travelled by the particle in the active and absorbing layers.

The overall performance of a calorimeter is given by the energy resolution. This represents the quadrature sum of all sources of uncertainty in the energy reconstruction which are usually broken down by their energy dependence and expressed as follows:

$$\frac{\sigma_E}{E} = \frac{a}{\sqrt{E}} \oplus \frac{b}{E} \oplus c, \quad (2.5)$$

where a , b and c are referred to as the stochastic, noise and leakage terms. The energy dependence of the background and leakage terms are straightforward to understand. Noise typically arises from the electronics used for collecting and reading out the hits in the active layers. This means that it is independent of the energy of the incident particles energy and so the absolute uncertainty does not vary with E . The leakage term accounts for the energy lost from the calorimeter because it is not sufficiently large to contain the shower. One can see from Eq. 2.3 that the energy lost will scale with the incident particle energy.

The stochastic term is slightly more complicated as it represents a combination of effects. The first of these is the intrinsic resolution of the detector which is determined by the physics of how an EM shower develops. The number of particles

produced in a shower (N) is proportional to the energy of the incident particle (E), however the formation of bremstrahlung photons and electron-positron pairs is a quantum mechanical process and so is inherently statistical. As a result N will follow a Poisson distribution and so the uncertainty on it will vary as $1/\sqrt{N}$. As N is proportional to E , this means there is an inherent uncertainty in the energy proportional to $1/\sqrt{E}$. There are also further statistical contributions that arise from using a sampling approach. For low energy particles produced in the absorber there is a chance that they be absorbed before reaching the active layer and so will not be accounted for in the scale factors. The uncertainty associated with this can be described by $\sqrt{E_{cx}/E}$. This factor is further added to by the effect mentioned above where x will vary from particle to particle depending on the path it takes through the detector. Because the energy deposited in a material as a function of the material depth is described by a Landau distribution, uncertainties from varying path lengths are often referred to as Landau fluctuations with the form σ_{landau}/\sqrt{E} .

2.4.1.4 ECAL

The ILD ECAL is a highly granular calorimeter poitioned at $r=1847$ mm which consists of 30 active layers separated by layers of absorbing material. Tungsten is chosen for the absorber due to its short radiation length, $\chi_0=0.35\text{cm}$. The first 20 absorber layers are $0.6\chi_0(2.1\text{mm})$ thick while the later layers are $1.2\chi_0$ to contain higher energy EM showers while maintaining a compact design. The structure of the ECAL is shown in Figure 2.9. The active material will consist of $5\times 5\text{ mm}^2$ pitch silicon pixels and yields a resolution of

$$\frac{\sigma_E}{E} = \frac{16.6 \pm 0.1}{\sqrt{(E(\text{GeV})}}} \oplus (1.1 \pm 0.1)\%, \quad (2.6)$$

While this is currently the default used in simulations for physics analyses, the choice of active material is yet to be finalised. A variation that uses $10\times 45\text{ mm}^2$ silicon scintillator strips, rotated by 90° in each successive layer, gives an effective cell size

of $10 \times 10 \text{ mm}^2$ with photomultipliers attached to each strip for readout. The energy resolution for this form of the detector has been measured to be [19]

$$\frac{\sigma_E}{E} = \frac{14}{\sqrt{E}} \oplus 2\%, \quad (2.7)$$

however the pixel version is typically favoured due to its simpler design which does not require additional offline processing to produce the desired (effective) granularity.

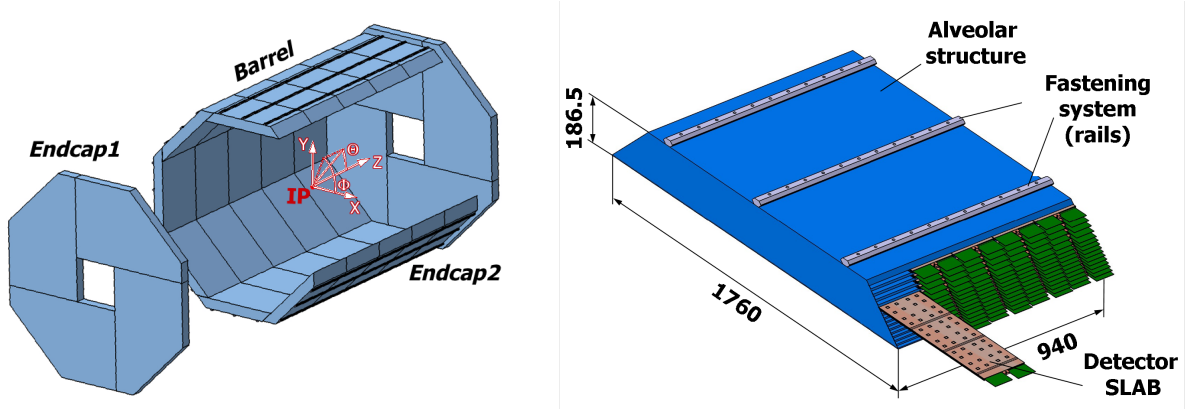


Figure 2.9: The Overall ILD Structure (left) and one individual module (right). The ECAL is made up 40 modules, each containing 30 detector slabs. The modules are combined into groups of 5 referred to as a stave which extend along the full length of the barrel. There are then 8 of these staves arranged in a circle to create the circumference of the barrel [26].

In Chapter 6 we will discuss our work on developing an alternative form of the silicon pixel technology with ultra-high granularity $50 \times 50 \mu\text{m}^2$ pixels which acts as a digital readout and purely counts the number of particles absorbed in the active medium from the showering in the absorber and deduces the energy of the original particle from this. This form of the technology has already begun to be studied [32]. It is expected to be cheaper than the standard silicon pixel technology as it is based on CMOS technology which is mass produced commercially, and has the potential for improved performance over its analogue counterpart due to reduced sensitivity to Landau fluctuations.

2.4.1.5 HCAL

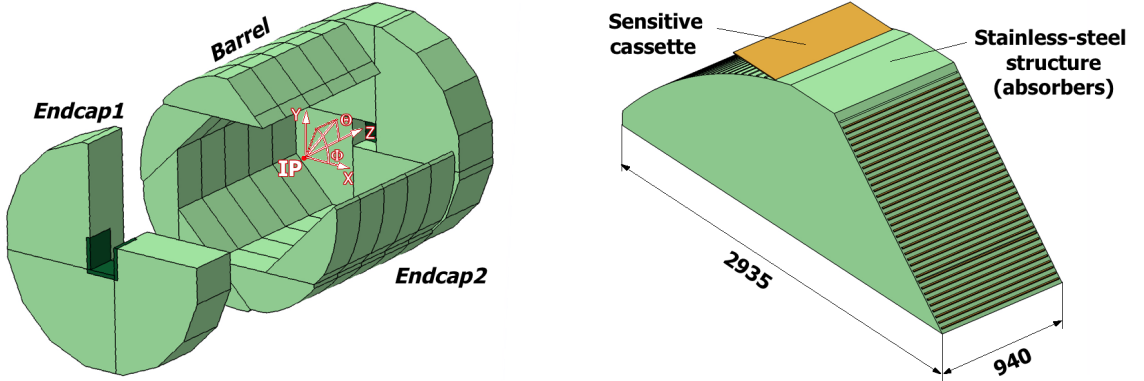


Figure 2.10: The Overall ILD HCAL Structure (left) and one individual module (right). The HCAL is made up 40 modules, each containing 30 detector slabs. The modules are combined into groups of 5 referred to as a stave which extend along the full length of the barrel. There are then 8 of these staves arranged in a circle to create the circumference of the barrel [26].

The HCAL is immediately outside the ECAL at $r=2058$ mm and has a similar overall modular structure to the ECAL as shown in Figure 2.10. Each module consists of 48 stainless steel absorber plates of thickness 20 mm interspersed with 3 mm silicon scintillators with a transverse segmentation of 30×30 mm 2 . This gives the HCAL a total depth of $\sim 5 \lambda_I$ (where λ_I is the nuclear interaction length, the equivalent of χ_0 for hadronic showers, which is typically much longer than χ_0) and an energy resolution of $49\%/\sqrt{E}$.

2.4.1.6 Muon Detection

Muon detection is perhaps the easiest process to perform at the ILC. Because the event environment at the ILC is typically clean with few high energy particles, few particles other than muons are capable of penetrating through the inner detector layers and the coil generating the magnetic field. As a result the muon detectors are produced by instrumenting the return yolk ($r=4424$ mm) that surrounds the detector to contain the magnetic field. The number of muons produced in an event is also relatively small which means that the cell size for the muon detectors can

be moderately large without the risk of multiple occupancy. The instrumentation is performed by placing 10 layers of resistive plate chambers into the return yolk with strip sizes of the order 3–4 cm. This system is sufficient for reliably detecting muons and contributing to the measurement of their momentum. This system provides $\sim 100\%$ efficiency for identifying muons with momentum > 3 GeV. Below this the muons do not have enough penetrating power to traverse the yolk. This identification performance can be extended down to 1.5 GeV when information from the calorimeters is also included.

2.4.1.7 Very Forward Region

Further instrumentation is present in the very forward regions of the detector for beam monitoring and to provide additional angular coverage. There are two main detectors of interest in this region.

The first of these is the LumiCal. As the name suggests this is designed for measuring the beam luminosity. The LumiCal consists of 30 layers of tungsten interspersed with silicon sensors covering the angular range of 32 to 74 mrad. The luminosity is determined by measuring the rate of Bhabha scattering in this region then scaling by the predicted cross section for the Bhabha scattering for the same angular range. As the Bhabha scattering process is an electroweak interaction the theoretical uncertainty on this cross section is small, $\mathcal{O}(10^{-4})$ [33], allowing for a precise measurement of the luminosity. For the studies presented here which are performed at 1.4 TeV at CLIC, this method allows the luminosity to be measured to a precision of $\sim 0.3\%$.

The second detector of interest is the LHCAL. This is a supplementary component of the HCAL which extends the coverage down to lower angles. The design for this is yet to be finalised, however it is expected to provide four radiation lengths of material covering the gap between the beam pipe and the HCAL endcap will consist of 40 layers of 1 cm thick tungsten interleaved with silicon.

Along side these there are also several systems for performing beam monitoring – namely the BeamCal, GamCal and pair monitor, however as these are less relevant to the studies presented in this thesis we shall not discuss them in detail here. Details on all the forward components of ILD can be found in the ILD letter of intent[26].

2.4.2 CLIC ILD

At CLIC the detector designs were originally based on the two ILC detectors, ILD and SiD, but with a few changes to adapt for the different experimental conditions at CLIC. In the case of ILD, due to the large beam related backgrounds the vertex detectors were moved to be 15 mm further radially from the IP to avoid pixel saturation. To account for the higher energy jets produced in interactions, the HCAL depth was extended to $7.5 \lambda_I$ to reduce leakage from the outer surface of the detector. To avoid increasing the radius of the solenoid (one of the main driving costs of the whole detector) the choice of absorber material in the HCAL was switched to tungsten to provide the increased interaction length but over the same depth as in the original steel design. In the barrels, because the thickness does not affect the solenoid radius, the absorber was left as steel. To improve the charge identification of higher energy tracks, the magnetic field strength was changed to be 4T which was found to still be achievable using the original ILD solenoid design. Further details on the CLIC version of ILD can be found in the CLIC CDR[20].

This version of the ILD detector is used for the analyses presented in Chapters 4 and 5. Since these analyses have been conducted, CLIC has recently produced a new unified detector design that will be used for future studies. Overall the design is similar to that of ILD but with a deeper ECAL to allow for higher energy photon containment and the tracker has been changed from a TPC to an all silicon tracker. As this version is not used in the studies presented here, we will not give a detailed account of the detector but more information is available in [34]. Overall the impact of the change in detector design is expected to be negligible for the studies presented here.

CHAPTER 3

Theory

Within this thesis two analyses are presented describing prospective measurements looking at the $H \rightarrow WW$ branching ratio and the forward-backward asymmetry in $t\bar{t}$ production at CLIC during the 1.4 TeV stage. As such it is important to first understand the physics behind these measurements and examine their significance in the context of the physics programme of CLIC and the wider state of particle physics.

3.1 The Standard Model

The SM is a quantum field theory representing our best current description of fundamental particles and the interactions between them. It consists of twelve spin- $\frac{1}{2}$ fermions (and their corresponding antiparticles), five spin 1 gauge bosons and one spin 0 scalar boson (as shown in Figure 3.1) where the interactions of the model

Type	Name	Mass	Charge (e)	Spin
Quark	Up	2.2 MeV	+2/3	1/2
Quark	Down	4.7 MeV	-1/3	1/2
Quark	Charm	1.28 GeV	+2/3	1/2
Quark	Strange	96 MeV	-1/3	1/2
Quark	Top	174 GeV	+2/3	1/2
Quark	Bottom	4.18 GeV	+1/3	1/2
Lepton	Electron	511 keV	-1	1/2
Lepton	Muon	106 MeV	-1	1/2
Lepton	Tau	1.77 GeV	-1	1/2
Lepton	Electron Nuetrino	~ 0	0	1/2
Lepton	Muon Neutrino	~ 0	0	1/2
Lepton	Tau Neutrino	~ 0	0	1/2
Gauge Boson	W^+	80.4 GeV	1	1
Gauge Boson	Z	91.2 GeV	0	1
Gauge Boson	γ	0	0	1
Gauge Boson	gluon	0	0	1
Scalar Boson	Higgs	125 GeV	0	0

Table 3.1: Particles of the Standard Model [9]

are described by an $SU(3)_C \oplus SU(2)_L \oplus SU(1)_Y$ local gauge symmetry. The model describes pointlike particles which interact via the strong, weak and electromagnetic forces. No gravitational interactions are described within the model.

The fermions of the model can be classified into two families- leptons and quarks- according to how they interact. The quark family consists of the up(u), down(d), charm(c), strange(s), top(t) and bottom(b) quarks, all of which are capable of interacting via the strong, weak and electromagnetic force. The lepton family, consisting of the electron(e), muon(μ), tau(τ), electron neutrino(ν_e), muon neutrino(ν_μ) and tau neutrino($\nu_{\tau\mu}$), are defined by the fact they carry no colour charge and so are incapable of interacting via the strong force, however they are still all capable of interacting via the weak force and the $e/\mu/\tau$ can interact electromagnetically. The gauge bosons are the mediators for the three fundamental forces of the model. The photon is a massless boson that mediates the electromagnetic force by coupling to particles with electrical charge. The gluon is also massless and mediates the strong force by coupling to particles with colour charge. The gluon is unique amongst the gauge bosons in that it is the only boson that carries the charge to which it couples (i.e. it is coloured) and so couples to itself. One direct consequence of this is that it is impossible to form a stable coloured state due to colour confinement and so quarks are only observed in net-colourless states called hadrons. When a quark is produced in an interaction, it will typically undergo a process known as hadronization in which the quark will bind to quarks/antiquarks spontaneously produced from the vacuum to form quark-antiquark pairs known as mesons, or triplets of quarks or antiquarks known as baryons. The only exception to this is the top quark which will typically decay in a shorter timescale than is needed for hadronization to occur. The final three gauge bosons are the Z, W^+ and W^- which are all massive and mediate the weak interaction via their coupling to weak isospin.

Much like the fermions can be separated into quarks and leptons according to the way they interact, the underlying symmetry of the SM of $SU(3)_C \oplus SU(2)_L \oplus SU(1)_Y$ can be decomposed into separate parts according to the interactions that the symmetries describe. The $SU(3)_C$ group represents transformations of the colour state of a

system and so describes interactions involving the strong force. These interactions are commonly referred to as QCD. The $SU(2)_L \oplus SU(1)_Y$ symmetry represents electroweak theory- a unified description of the weak and electromagnetic interactions. In this description, fermions can be thought of as consisting of left and right handed fields, where the left handed components transform as doublets under $SU(2)$ transformations while the right handed components only transform as singlets. The result of this is that the weak interaction only acts on the left handed field components. Hence the weak force only couples to left(right) handed particles (antiparticles.)

One of the most interesting features of electroweak theory occurs when considering the effect of gauge transformations on the Lagrangian of the system. In quantum field theory, fermions can be described by a dirac field with the following Lagrangian:

$$\mathcal{L} = i\bar{\psi}\gamma^\mu\partial\mu\psi - m\bar{\psi}\psi \quad (3.1)$$

Applying a global phase transition of the form:

$$\psi \rightarrow \psi' = e^{i\alpha}\psi \quad (3.2)$$

will leave the Lagrangian unchanged due to the fact $e^{i\alpha}\psi e^{-i\alpha}\psi = 1$. However, in the case of local gauge transformations where $e^{i\alpha}\psi \rightarrow e^{i\alpha(\mathbf{x})}\psi$, i.e. the phase has a local space-time dependence, then eqEq. 3.1 is no longer invariant:

$$\mathcal{L} = i\bar{\psi}\gamma^\mu\partial_\mu\psi - m\bar{\psi}\psi - \bar{\psi}(\mathbf{x})\gamma^\mu\partial_\mu\alpha(\mathbf{x}) \quad (3.3)$$

In order to restore the invariance, the derivative $\partial\mu$ must be replaced with the covariant derivative D_μ which is of the form:

$$D_\mu = \partial_\mu + ieA_\mu \quad (3.4)$$

where A_μ is a gauge field which transforms as:

$$A_\mu \rightarrow A'_\mu = A_\mu - \frac{1}{e} \partial_\mu \alpha(\mathbf{x}) \quad (3.5)$$

In electroweak theory the gauge fields required are found to consist of three weak isospin fields, W_1, W_2 and W_3 , coming from the $SU(2)$ group and one weak hypercharge field, B , from $U(1)$. The interesting result of this is the prediction that the bosons associated with these fields and the fermions they interact with should be massless, however this is experimentally found to be false as the bosons of the weak force, Z and W , have masses of 91.876 ± 0.0021 GeV and 80.385 ± 0.015 GeV respectively. Furthermore, in electroweak theory it can be shown that the presence of massive electroweak bosons results in unphysical predictions in the SM e.g. violation of unitarity when calculating the amplitude of $WW \rightarrow WW$ scattering [35]. These problems can be fixed via consideration of the final particle within the SM, the Higgs boson.

3.2 The Higgs Boson and the Origin of Mass

To solve the problems seen in the electroweak sector, Brout, Englert and Higgs [36][37] proposed that mass terms could be generated within the SM via the addition of a complex, scalar doublet of the group $SU(2)$ possessing four degrees of freedom:

$$\phi = \begin{pmatrix} \phi^+ \\ \phi^0 \end{pmatrix} \quad (3.6)$$

with potential:

$$V(\phi) = \mu^2 \phi^\dagger \phi + \frac{\lambda^2}{2} (\phi^\dagger \phi)^2 \quad (3.7)$$

The Higgs field is found to interact with the W_1, W_2, W_3 and B gauge fields. In the case that $\mu^2 < 0$, due to the Higgs field acquiring a non-zero expectation value, the $SU(2)_L \oplus SU(1)_Y$ symmetry is found to break leaving only a $U(1)_{em}$ symmetry corresponding to a massless photon. Of the four degrees of freedom associated with the Higgs field, the interaction of the field with the W and B gauge fields results in three massive gauge bosons corresponding to the measured Z and W^\pm masses, where the physically observed bosons actually represent mixtures of the underlying gauge fields:

$$\gamma = \cos \theta_W B + \sin \theta_W W_3 \quad (3.8)$$

$$Z = \cos \theta_W W_3 - \sin \theta_W B \quad (3.9)$$

$$W^\pm = \frac{1}{\sqrt{2}}(W_1 \mp iW_2) \quad (3.10)$$

Where θ_W is the weak mixing angle.

The last remaining degree of freedom of the Higgs field corresponds to the Higgs boson itself. The mass of the Higgs boson can be determined to be $m_H = \sqrt{2\lambda}\nu$, where λ is the Higgs self coupling parameter and ν is the vacuum expectation value for the Higgs field. While ν can be calculated within the standard model, λ is a free parameter and so the mass of the Higgs is not derivable. Experimentally it is found to be ~ 125 GeV.

While the mass of the Higgs is of interest as it represents a free parameter in the standard model, there are many more properties of the Higgs that are important to measure. In particular the way in which the Higgs boson couples to other particles is well predicted within the SM and is expected to vary between various BSM models. Within the SM the coupling of the Higgs to fermions and bosons is different but

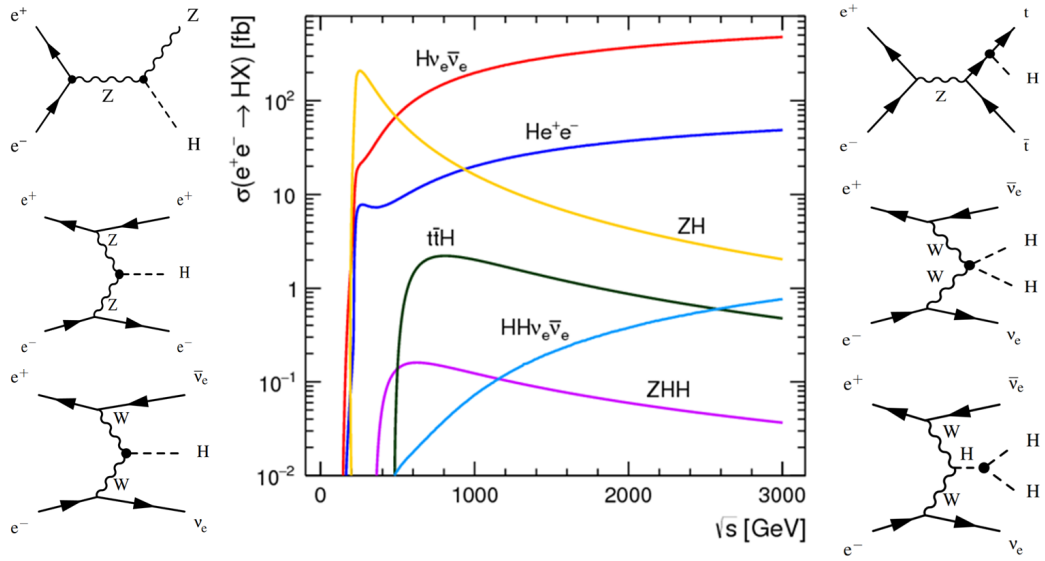


Figure 3.1: Cross Sections For Higgs Production Mechanisms [1]

depends on mass in each case:

$$g_{Hf\bar{f}} = \frac{M_f}{\nu} \quad g_{HBB} = \frac{2M_B^2}{\nu} \quad (3.11)$$

Due to this clear mass dependence, a fit of the coupling to each fermion as a function of the fermions mass represents a powerful way of testing the SM. The mass dependence on the Higgs couplings also presents a new way to perform indirect searches for new physics involving as yet unseen massive particles by looking at the branching ratio of Higgs decays to invisible decay products and the total Higgs decay width. This is of particluar interest in searches for dark matter which is known to interact gravitationally and so must possess mass.

3.3 Higgs Measurements at CLIC

The CLIC physics programme places a large focus on characterising the Higgs boson as it presents a new and relatively less well measured sector of the SM to explore. In particluar it will aim to measure the mass, width, and couplings of the Higgs in a

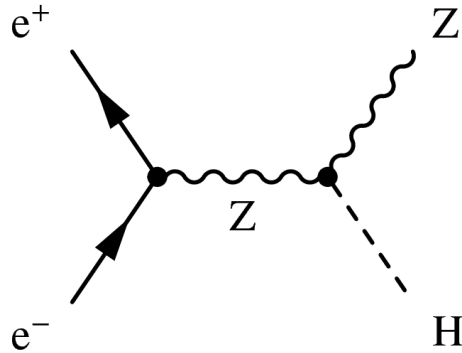


Figure 3.2: The Higgsstrahlung Process

model independent manner. Electron positron collisions provide access to numerous Higgs production mechanisms which can be seen in Figure 3.1. Due to the strong energy dependence on many of the cross sections on energy, different processes will be of interest at each of the three energy stages operated at CLIC. At 380GeV the focus will predominantly be on measuring the Higgsstrahlung (ZH) process in which a Z boson radiates a Higgs, while at higher energies vector boson fusion ($H\nu\bar{\nu}, He^+e^-$) dominates and new processes such as di-Higgs production become accessible. A summary of all the results from current Higgs studies performed by CLIC is available in [1].

3.3.1 Higgsstrahlung

One of the key aims of the experiment will be to examine the Higgsstrahlung process shown in Figure 3.2. In this process, if the four momentum of the Z boson can be measured to high precision, then because the initial conditions of the collision are well known, one can determine the mass of the particle it is recoiling against ($m_{rec}^2 = s + m_z^2 - 2E_z^2$) and infer the presence of the Higgs. This allows properties such as the Higgs mass, cross-section and coupling to the Z to be measured without actually ever measuring the decay products of the Higgs boson, which in turn allows the measurements to be model independent as few assumptions must be made about the properties of the Higgs. This method is not possible at hadron colliders such as the LHC where, even though the Higgsstrahlung process still occurs, the four

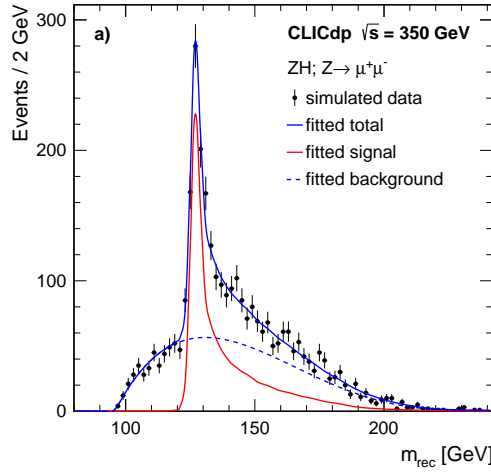


Figure 3.3: Reconstructed recoil mass from Higgsstrahlung process [1]

momentum of the colliding particles can never be known as precisely due to their composite nature. Using the clean signal from cases where the Z decays to a pair of muons or electrons it is possible to measure the recoil mass to high precision and thus determine the mass of the Higgs to $\Delta m_H = 110 \text{ MeV}$ (see Figure 3.3) using data from the low energy stage only. This value can be further improved to $\Delta m_H = 44 \text{ MeV}$ when including direct measurement results from the $ee \rightarrow H\nu\bar{\nu}, H \rightarrow b\bar{b}$ channel at 3 TeV. Despite giving a poorer resolution on the Z four momentum, the $Z \rightarrow qq$ higgsstrahlung channel is also considered due to it's larger cross section. Using this channel a limit of $BR(H \rightarrow \text{invis.}) < 0.97\%$ at 90% C.L. can be set.

3.3.2 Model Independent Extraction of Higgs Couplings

While the Higgsstrahlung alone allows the mass and branching ratios of the Higgs to be determined, it is further possible to extract the absolute width of the Higgs, Γ_H , by measuring the rates of several different Higgs processes and combining them in the right ratio. One such scheme proposed for doing this is shown in Eq. 3.12 [38]:

$$\Gamma_H = \frac{X_1^2 X_3^2}{X_4^2 X_2} \quad (3.12)$$

where

$$X_1 = \sigma_{ZH} \propto g_{HZZ}^2 \quad (3.13)$$

$$X_2 = \sigma_{H\nu\bar{\nu}} \times BR(H \rightarrow WW^*) \propto \frac{g_{HWW}^4}{\Gamma_H} \quad (3.14)$$

$$X_3 = \sigma_{H\nu\bar{\nu}} \times BR(H \rightarrow b\bar{b}) \propto \frac{g_{HWW}^2 g_{Hbb}^2}{\Gamma_H} \quad (3.15)$$

$$X_4 = \sigma_{ZH} \times BR(H \rightarrow b\bar{b}) \propto \frac{g_{HZZ}^2 g_{Hbb}^2}{\Gamma_H} \quad (3.16)$$

With the exception of X_1 , the choice of variables used is not unique (e.g. one could replace the production mechanism in X_1 and X_2 with ZZ-fusion rather than WW-fusion,) however the combination shown here is expected to give the highest precision on Γ_H due to the large cross-section associated with WW-fusion and the high branching ratio of $H \rightarrow b\bar{b}$ ($\sim 65\%$). In chapter 4 we will present our research on the precision to which X_2 can be measured during the 1.4 TeV run at CLIC. Currently at the LHC the standard process for extracting couplings from the equivalent measurements of $X_{2,3\&4}$ is to multiply through by the standard model value of the Higgs width [39]. This type of measurement is referred to as ‘model-dependent’ as the values determined for the Higgs couplings carry the implicit assumption that the standard model is correct in its prediction of the Higgs width. At CLIC, because the width can be measured experimentally there is no need to make this assumption and so the couplings are measured in a “model-independent” way. The unique ability of linear colliders to perform model-independent measurements is one of the largest driving factors for constructing and using them as a so called “Higgs-Factory”. One limiting factor for the model-independent measurements of the couplings is that they are always ultimately dependent on the precision to which the ZH cross section

Channel	Measurement	Observable	Statistical precision
			350 GeV 500 fb^{-1}
ZH	Recoil mass distribution	m_H	110 MeV
ZH	$\sigma(\text{ZH}) \times BR(H \rightarrow \text{invisible})$	Γ_{inv}	0.6 %
ZH	$\sigma(\text{ZH}) \times BR(Z \rightarrow l^+l^-)$	g_{HZZ}^2	3.8 %
ZH	$\sigma(\text{ZH}) \times BR(Z \rightarrow q\bar{q})$	g_{HZZ}^2	1.8 %
ZH	$\sigma(\text{ZH}) \times BR(H \rightarrow b\bar{b})$	$g_{HZZ}^2 g_{Hbb}^2 / \Gamma_H$	0.84 %
ZH	$\sigma(\text{ZH}) \times BR(H \rightarrow c\bar{c})$	$g_{HZZ}^2 g_{Hcc}^2 / \Gamma_H$	10.3 %
ZH	$\sigma(\text{ZH}) \times BR(H \rightarrow gg)$		4.5 %
ZH	$\sigma(\text{ZH}) \times BR(H \rightarrow \tau^+\tau^-)$	$g_{HZZ}^2 g_{H\tau\tau}^2 / \Gamma_H$	6.2 %
ZH	$\sigma(\text{ZH}) \times BR(H \rightarrow WW^*)$	$g_{HZZ}^2 g_{HWW}^2 / \Gamma_H$	5.1 %
H $v_e \bar{v}_e$	$\sigma(Hv_e \bar{v}_e) \times BR(H \rightarrow b\bar{b})$	$g_{HWW}^2 g_{Hbb}^2 / \Gamma_H$	1.9 %
H $v_e \bar{v}_e$	$\sigma(Hv_e \bar{v}_e) \times BR(H \rightarrow c\bar{c})$	$g_{HWW}^2 g_{Hcc}^2 / \Gamma_H$	14.3 %
H $v_e \bar{v}_e$	$\sigma(Hv_e \bar{v}_e) \times BR(H \rightarrow gg)$		5.7 %

Figure 3.4: Expected statistical uncertainties for Higgs measurements at 350GeV at CLIC assuming unpolarised beams [1]

can be measured (predicted to be $\Delta h_{HZZ} = 0.8\%$) as this quantity is always needed in the ratio used to extract Γ_H .

In practice it is expected that an 11 parameter global fit to multiple variations of these measurements will be performed at each stage of operation to extract the Higgs width and its couplings to both fermions and bosons. The relevant inputs for these fits are shown in Table 3.4 and 3.5 while the results of the fits are shown in Figure 3.6

For context it is also important to compare these results to what can be expected from current leading experiments such as ATLAS and CMS at the LHC. Because the Higgs width can not be explicitly calculated at Hadron colliders, it is best to compare the model dependent version of the CLIC analysis with those predicted by ATLAS and CMS. In this situation, because the precision of the couplings is no longer limited by the precision on g_{HZZ} , the predicted precision for CLIC is seen to improve considerably. One can see from Figure 3.7 and 3.8 that in many cases CLIC is expected to provide an order of magnitude improvement over what can be achieved at the LHC with many of the key parameters associated with the Higgs being measured to sub percent precision.

Channel	Measurement	Observable	Statistical precision	
			1.4 TeV 1.5 ab ⁻¹	3 TeV 2.0 ab ⁻¹
H $\nu_e \bar{\nu}_e$	H $\rightarrow b\bar{b}$ mass distribution	m_H	47 MeV	44 MeV
H $\nu_e \bar{\nu}_e$	$\sigma(H\nu_e \bar{\nu}_e) \times BR(H \rightarrow b\bar{b})$	$g_{HWW}^2 g_{Hbb}^2 / \Gamma_H$	0.4 %	0.3 %
H $\nu_e \bar{\nu}_e$	$\sigma(H\nu_e \bar{\nu}_e) \times BR(H \rightarrow c\bar{c})$	$g_{HWW}^2 g_{Hcc}^2 / \Gamma_H$	6.1 %	6.9 %
H $\nu_e \bar{\nu}_e$	$\sigma(H\nu_e \bar{\nu}_e) \times BR(H \rightarrow gg)$	$g_{HWW}^2 g_{Hgg}^2 / \Gamma_H$	5.0 %	4.3 %
H $\nu_e \bar{\nu}_e$	$\sigma(H\nu_e \bar{\nu}_e) \times BR(H \rightarrow \tau^+\tau^-)$	$g_{HWW}^2 g_{H\tau\tau}^2 / \Gamma_H$	4.2 %	4.4 %
H $\nu_e \bar{\nu}_e$	$\sigma(H\nu_e \bar{\nu}_e) \times BR(H \rightarrow \mu^+\mu^-)$	$g_{HWW}^2 g_{H\mu\mu}^2 / \Gamma_H$	38 %	25 %
H $\nu_e \bar{\nu}_e$	$\sigma(H\nu_e \bar{\nu}_e) \times BR(H \rightarrow \gamma\gamma)$	$g_{HWW}^2 g_{H\gamma\gamma}^2 / \Gamma_H$	15 %	10 %*
H $\nu_e \bar{\nu}_e$	$\sigma(H\nu_e \bar{\nu}_e) \times BR(H \rightarrow Z\gamma)$	$g_{HWW}^2 g_{HZ\gamma}^2 / \Gamma_H$	42 %	30 %*
H $\nu_e \bar{\nu}_e$	$\sigma(H\nu_e \bar{\nu}_e) \times BR(H \rightarrow WW^*)$	g_{HWW}^4 / Γ_H	1.0 %	0.7 %*
H $\nu_e \bar{\nu}_e$	$\sigma(H\nu_e \bar{\nu}_e) \times BR(H \rightarrow ZZ^*)$	$g_{HWW}^2 g_{HZZ}^2 / \Gamma_H$	5.6 %	3.9 %*
He ⁺ e ⁻	$\sigma(He^+e^-) \times BR(H \rightarrow bb)$	$g_{HZZ}^2 g_{Hbb}^2 / \Gamma_H$	1.8 %	2.3 %*
t $\bar{t}H$	$\sigma(t\bar{t}H) \times BR(H \rightarrow b\bar{b})$	$g_{Htt}^2 g_{Hbb}^2 / \Gamma_H$	8.4 %	—
HH $\nu_e \bar{\nu}_e$	$\sigma(HH\nu_e \bar{\nu}_e)$	λ	32 %	16 %
HH $\nu_e \bar{\nu}_e$	with -80 % e ⁻ polarisation	λ	24 %	12 %

Figure 3.5: Expected statistical uncertainties for Higgs measurements at 1.4TeV and 3TeV at CLIC assuming unpolarised beams [1]

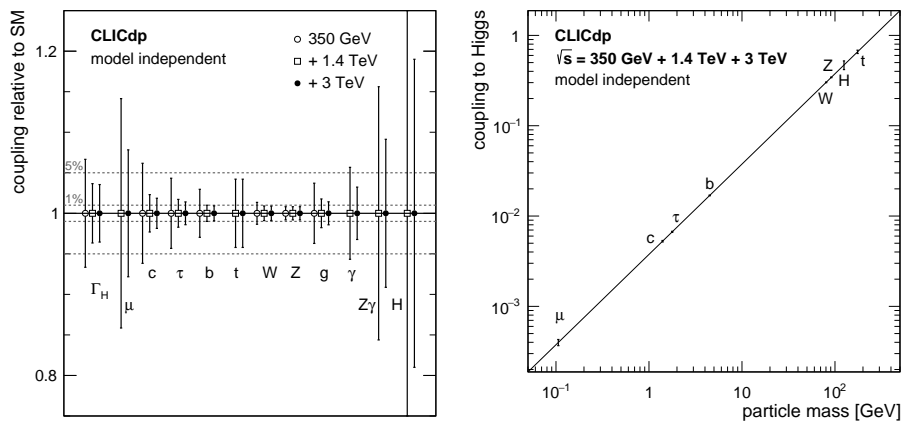


Figure 3.6: Expected precision on model independent measurements of the Higgs couplings [1]

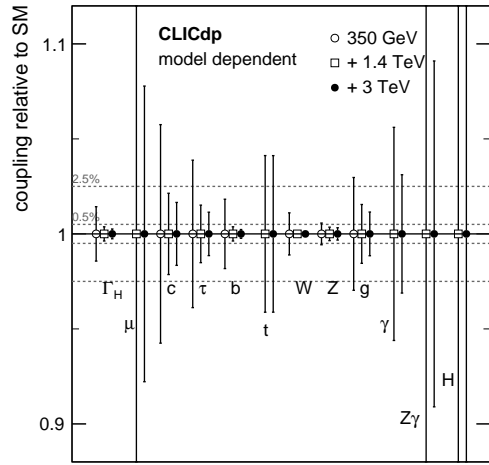


Figure 3.7: Expected precision on model dependent measurements of the Higgs couplings at CLIC [1]

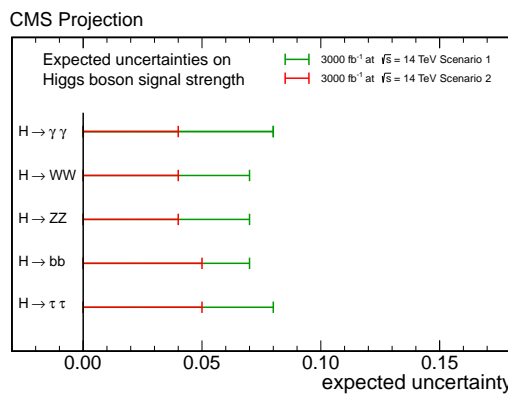


Figure 3.8: Expected precision on model dependent measurements of the Higgs couplings at CMS for the HL-LHC. Scenario 1 represents a case where the systematic and theoretical uncertainties remain at their current levels. In scenario 2 the theoretical uncertainty is scaled by a factor of a half and the systematic uncertainties are scaled by the square root of the integrated luminosity [40].

Model	κ_V	κ_b	κ_γ
Singlet Mixing	~6%	~6%	~6%
2HDM	~1%	~10%	~1%
Decoupling MSSM	~-0.0013%	~1.6%	~-4%
Composite	~-3%	~-(3-9)%	~-9%
Top Partner	~-2%	~2%	~+1%

Table 3.2: Generic size of Higgs coupling modifications from the SM values when all new pariles are $M \sim 1\text{TeV}$ and mixing angle satisfy precision electroweak fits. The Decoupling MSSM numbers assume $\tan \beta = 3.2$ and a stop mass of 1 TeV with $X_t = 0$ for the κ_γ prediction [11]

Ultimately the aim of performing precision measurements is to be allow the validation or rejection of theoretical models. While the results seen so far at the LHC suggest that the observed Higgs Boson is that of the SM, their are numerous alternative theories that predict a Higgs like particle with properties similar to what has been observed but which differ to a degree not yet measureable by current experiments. The details of these theories will not be expanded upon within this thesis, however the deviations expected in the Higgs couplings of these theories relative to the SM are shown in Table 3.2 These values should only be taken as a rough guideline for the precision required to discover/reject the theories as they are based on the assumption that new physics occurs at a specific scale (in this case 1 TeV,) however it is clear that the level of precision required to provide sensitivity to these models is expected to be greater than what will be possible with the LHC but could be within the scope of the proposed CLIC physics programme.

3.4 Top Quark Physics

The top quark is currently the heaviest particle within the SM and is the only quark that decays before undergoing hadronization. Due to it's high mass, top interactions are often seen as good channels for looking for BSM physics with a characteristic energy scale beyond what has currently been discovered. Due to it's high mass, the top is also the fermion with the highest coupling to the Higgs making

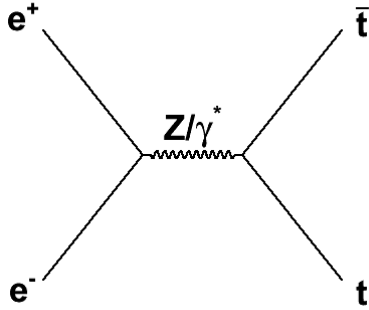


Figure 3.9: Dominant top production mechanism at electron positron collider

it a good candidate for finding deviations from the SM within the Higgs sector. As such, the physics programme for CLIC places a strong focus on measuring the top quarks properties with the lowest energy stage of operation featuring a dedicated top threshold scan aiming to provide precision measurements of the top mass and width. The dominant production mechanism for top production is through the s-channel: $e^+e^- \rightarrow \gamma/Z \rightarrow t\bar{t}$ process shown in Figure 3.9. Using this process the properties of the $t\bar{t}\gamma$ and $t\bar{t}Z$ vertices can be measured. Examining these can provide sensitivity to contributions from BSM effects such as the existence of extra bosons (e.g. Z' [41]) which could provide an additional production channel, modifying the behaviour at the vertex. The $t\bar{t}X$ vertex can be written as below [42]:

$$\Gamma_\mu^{t\bar{t}X}(s, q, \bar{q}) = ie\{\gamma_\mu(F_{1V}^X(s) + \gamma_5 F_{1A}^X(s)) - \frac{\sigma_{\mu\nu}}{2m_t}(q + \bar{q})^\nu(iF_{2V}^X(s) + \gamma_5 F_{2V}^X(s))\} \quad (3.17)$$

Where $X = \gamma/Z$, q and \bar{q} are the four momenta of the top and anti top, s is Mandelstam , γ_μ and γ_5 are the Dirac matrices corresponding to vector and axial-vector currents respectively, $\sigma_{\mu\nu} = \frac{i}{2}(\gamma_\mu\gamma_\nu - \gamma_\nu\gamma_\mu)$ allows for describing the scattering and F are the electroweak form factors. Within the SM, at tree level all the F_2 are zero as is F_{1A}^γ leaving only the following non-zero form factors:

$$F_{1V}^\gamma = \frac{2}{3} \quad (3.18)$$

$$F_{1V}^Z = \frac{1}{4 \sin \theta_W \cos \theta_W} \left(1 - \frac{8}{3} \sin \theta_W\right) \quad (3.19)$$

$$F_{1A}^Z = \frac{1}{4 \sin \theta_W \cos \theta_W} \quad (3.20)$$

where θ_W is the weak mixing angle. If higher order corrections are present it is possible for the zero valued form factors to become non-zero. Combinations of these factors can be related to physical observables which can be measured at CLIC. The couplings of the bosons to quarks with left or right handed helicity can be expressed as:

$$g_L^X = F_{1V}^X - F_{1A}^X \quad g_R^X = F_{1V}^X + F_{1A}^X \quad (3.21)$$

The most relevant variables are perhaps the total cross section and the forward backward asymmetry (A_{FB}) as these are the prospective measurements that are presented later within this thesis and will be discussed in more detail in Chapter 5. The forward backward asymmetry is especially of interest as the measurement of the b quark forward-backward asymmetry at Large Electron-Positron Collider (LEP)[43] currently produces the largest tension with the SM, $\mathcal{O}(3\sigma)$ [44], in electroweak fits. These variables are found to be dependent on the helicity of the incoming electrons [45] and so are more easily expressed in terms of the alternative form factors:

$$F_{ij}^L = -F_{ij}^\gamma + \left(\frac{-\frac{1}{2} + \sin \theta_W^2}{\sin \theta_W \cos \theta_W}\right) \left(\frac{s}{s - m_Z^2}\right) - F_{ij}^Z \quad (3.22)$$

$$F_{ij}^R = -F_{ij}^\gamma + \left(\frac{\sin \theta_W^2}{\sin \theta_W \cos \theta_W}\right) \left(\frac{s}{s - m_Z^2}\right) - F_{ij}^Z \quad (3.23)$$

Where L,R represent the polarization of the electron, i=1,2 and j=V,A. In this notation, for an electron polarization P, the total $ee \rightarrow Z/\gamma \rightarrow tt$ cross section and

A_{FB} can be expressed as:

$$\sigma_P = \frac{8\pi\alpha(s)^2}{s} \beta \left\{ \left(1 + \frac{1}{2\gamma^2}\right) (F_{1V}^P)^2 + (\beta F_{1A}^P)^2 + 3F_{1V}^P F_{2V}^P + \left(1 + \frac{1}{2\gamma^2}\right) (F_{2V}^P)^2 \right\} \quad (3.24)$$

$$A_{FB}(P) = \mp \frac{12\pi\alpha(s)^2\beta^2}{s} \frac{F_{1A}^P (F_{1V}^P + F_{2V}^P)}{\sigma_P} \quad (3.25)$$

where $\alpha(s)$ is the electromagnetic coupling, γ and β are the Lorentz factor and velocity of the top, and for Eq. 3.25, the $+$ and $-$ refer to the $P = R$ and $P = L$ cases respectively. If one performed just one measurement of the cross section and A_{FB} it is clear that it would not be possible to extract the form factors from these variables alone as there are more variables than there would be constraints. However, because the cross section and A_{FB} vary with β , γ and P , then by performing the measurement at multiple energies and making use of the fact CLIC can be operated with different beam polarizations, it becomes possible to extract all the relevant couplings. The only exceptions to this are the F_{2A}^X factors which do not effect these two variables and so must be measured using alternative methods.

The predicted uncertainty to which the couplings are expected to be measured to at CLIC based on generator level studies, as well as the equivalent results for ILC and HL-LHC is shown in Figure 3.10. The expected precision from performing these measurements at a lepton collider is an order of magnitude better than what can be expected from hadron colliders. Overall there will be more tops produced in a hadron collider, however the production mechanisms are often more complicated making it harder to extract the couplings from a theory perspective, and it is also harder to successfully identify tops (which typically decay to at least one jet) in an environment that contains QCD jets from beam remnants compared to at lepton colliders where there is minimal QCD background within an event.

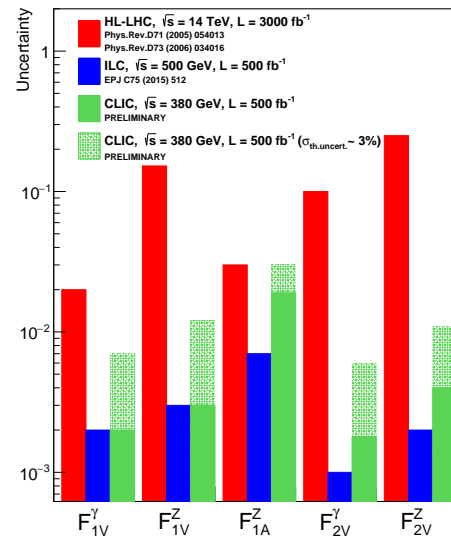


Figure 3.10: Expected precision on CP conserving electroweak form factors at future colliders [14]

CHAPTER 4

Higgs to WW* at 1.4 TeV

As mentioned in Chapter 3, one of the key aims of the CLIC physics programme will be to perform model independent measurements of the Higgs couplings. In order to be able to do this, the total width of the Higgs must first be measured. This has been found to be possible by taking the ratio of four different measurements:

$$X_1 = \sigma_{ZH} \propto g_{HZZ}^2$$

$$X_2 = \sigma_{H\nu\bar{\nu}} \times BR(H \rightarrow WW^*) \propto \frac{g_{HWW}^4}{\Gamma_H}$$

$$X_3 = \sigma_{H\nu\bar{\nu}} \times BR(H \rightarrow b\bar{b}) \propto \frac{g_{HWW}^2 g_{Hbb}^2}{\Gamma_H}$$

$$X_4 = \sigma_{ZH} \times BR(H \rightarrow b\bar{b}) \propto \frac{g_{HZZ}^2 g_{Hbb}^2}{\Gamma_H}$$

Here we will look at the measurement of one of these, X_2 . As can be seen from Figure 4.1, WW-fusion is the dominant Higgs production mechanism for energies above ~ 500 GeV and so this measurement is best performed in the higher energy

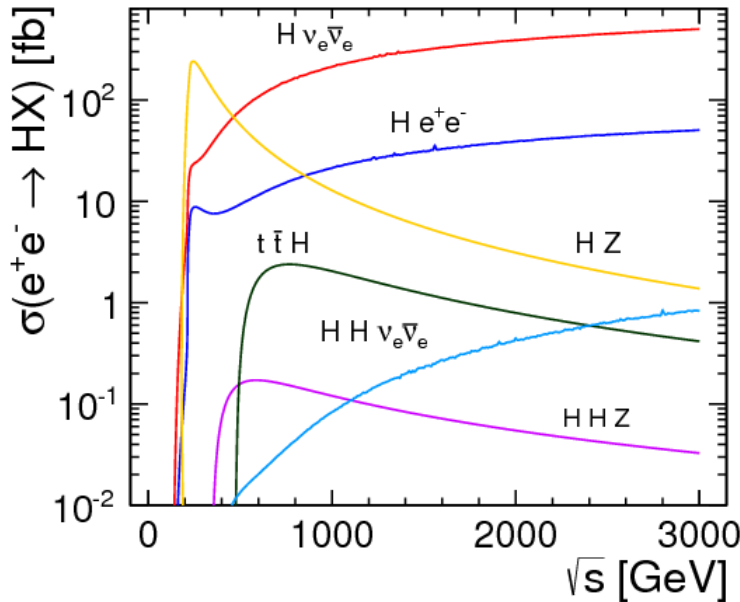


Figure 4.1: Cross sections for dominant Higgs production mechanisms as a function of energy [1]. Higgs production via WW-fusion is shown in red.

stages of operation. In particular we will focus on measuring X_2 at 1.4 TeV. For measuring the branching ratio for $H \rightarrow WW$ there are three potential final states that can be examined depending on the decay mode of the two W's. An individual W will decay hadronically (into a quark pair) 67.41% of the time and leptonically (into a lepton + neutrino) 32.58% of the time. The combinations available from each W decaying give three final states referred to as the hadronic, semileptonic and leptonic decay modes corresponding to both W's decaying hadronically, one W decaying hadronically while the other decays leptonically and both W's decaying leptonically. The relative abundance for each decay mode is roughly 4:4:1. Here we will only study the semileptonic mode (Figure 4.2.) An equivalent analysis has already been performed for the hadronic final state yielding a statistical precision of 1.5% on X_2 [1]. Due to its lower branching ratio, the leptonic decay mode has yet to be studied as it is not expected to yield a significant improvement on the statistical precision achievable for X_2 .

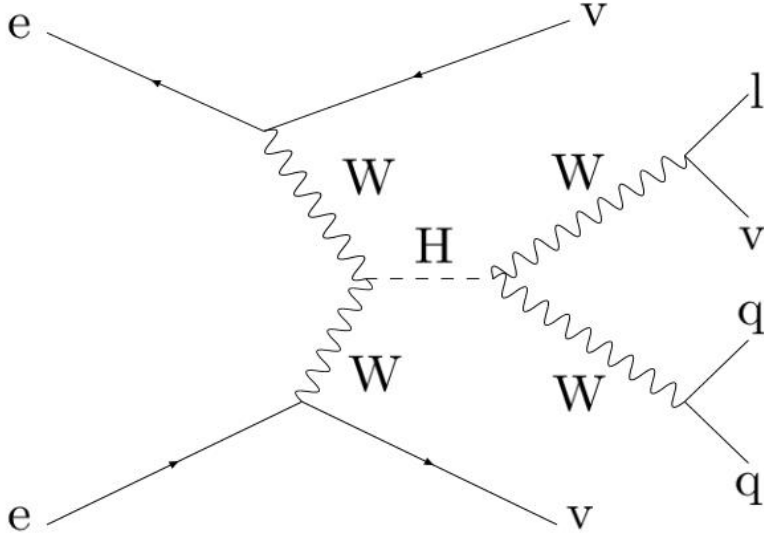


Figure 4.2: Semileptonic decay channel for WW^* decays of Higgs produced through WW-fusion

4.1 Event Generation

All events used in this analysis were produced centrally by CLIC using WHIZARD 1.95 [21] and are summarised in Table 4.3. In the case of $e\gamma$ events, a scale factor of 2 was applied to the cross section to account for interactions occurring with both the electron and positron. In the case of beamsstrahlung events (simulated using GUINEA-PIG [46]), a further scaling of 0.75 was applied to account for the lower luminosity of these type of collisions. Sample 2022 is the $ee \rightarrow H\nu\nu$ inclusive sample. The relevant events were extracted from this main sample by performing a parton level event selection to identify events in which the Higgs decayed to W's and separating these according to their decay products. At this point events in which the lepton produced in the W decay is found to be a tau are excluded from the signal definition due to the fact they produce a different topology in the final state compared to electrons and muons. In all cases the detector model used is CLICILD_CDR, CLIC's variation of the ILD detector designed for ILC described in the CDR[20]. The main backgrounds of note are: the $ee \rightarrow qql\nu$ process (dominated by $e^+e^- \rightarrow W^+W^-$) as it has a very similar topology to our signal process and so is expected to be the most difficult to exclude; and the $ee \rightarrow H(WW^* \rightarrow qqqq)\nu\nu$

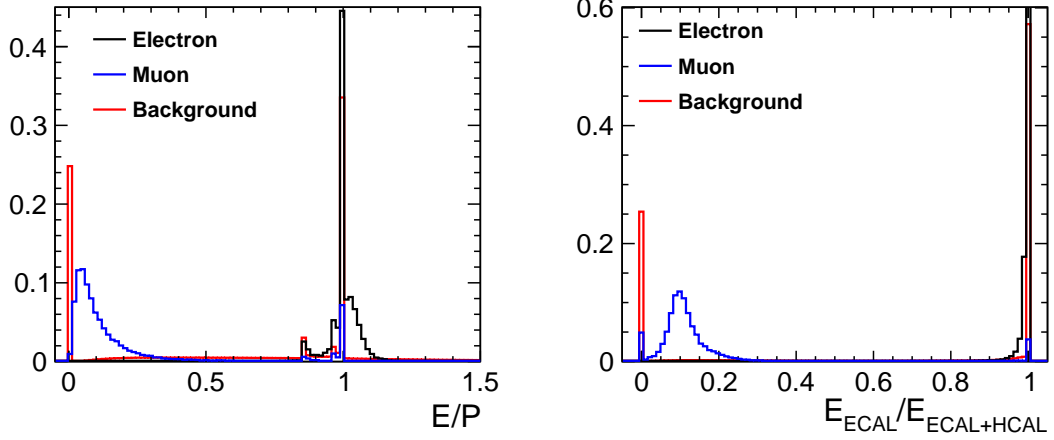
Process	Cross Section(fb)	Production ID[47]	Events Used
Signal: ee \rightarrow H(WW* \rightarrow qql $\nu\nu$)	17.3	2022	70000
ee \rightarrow H(WW* \rightarrow qqqq) $\nu\nu$	27.4	2022	100000
ee \rightarrow H* \rightarrow Other	199.4	2022	800000
ee \rightarrow qq	4009.5	2091	500000
ee \rightarrow qqqq	1328.1	2163	300000
e γ \rightarrow eqq (γ from EPA)	32308	2515	500000
e γ \rightarrow eqq (γ from BS)	56043	2527	500000
ee \rightarrow qq $\nu\nu$	787.7	3243	500000
ee \rightarrow qql	2725.8	3246	400000
ee \rightarrow qql ν	4309.7	3249	1000000

Figure 4.3: Samples used for the H \rightarrow WW* analysis

process as contamination from these events after event selection must be taken into account for before any combination of results from the semileptonic and hadronic channels can be made.

4.2 Event Reconstruction

Reconstruction of the signal events was performed using ILCSoft v01-17-06 and was carried out in two main stages as described below. The first stage was to identify the isolated lepton associated with the leptonic W boson decay. The second stage involved removing this isolated lepton and resolving the remaining particles into two jets that were associated with the two quarks produced by the hadronically decaying W boson. Using the two jets, the W boson could then be reconstructed and combined with the isolated lepton to reconstruct the Higgs boson. The reconstructed Higgs candidate will not be complete due to the missing energy and momentum from the lepton neutrino produced from the W decay. However, the observed properties will still be sufficient for providing discrimination between signal and background events.



(a) Ratio of the energy deposited in both calorimeters to the particles momentum.
(b) Ratio of the energy deposited in the ECAL to the total energy deposited in the calorimeters.

Figure 4.4: Properties used for the loose lepton selection. Note that in both cases, electrons and muons not produced in the initial W decay are counted as background.

4.2.1 Lepton Identification

Two different methods were used for identifying leptons. Our primary method for particle identification is to assume that the highest energy electron or muon (as identified by PandoraPFA [25]) corresponds to the isolated lepton from the leptonically decaying W boson. This method was found to have an efficiency of 93% (90% for electrons, 96% for muons) and purity of 96% for identifying the isolated lepton. The improved efficiency for muons relative to electrons is a result of the different signatures they leave in the detector. Electrons are identified by the presence of a track followed by a deposit in the ECAL. If the track is not reconstructed or is wrongly attributed to a different calorimeter deposit by Pandora, the electron will be wrongly identified as a photon (characterised by no track, only energy deposited in the ECAL.) Muons on the other hand are highly penetrating and so will leave deposits in the HCAL and muon tail catchers as well as the tracker and ECAL. As a result, even if one part of the detector system fails there is enough redundancy in the measurement that the muon should still be identified.

The second method used a series of cuts to select the isolated lepton. The first stage

of this was to group the particles in the event into four jets. This was done using FastJet [48] to implement the kt-algorithm using the E-scheme for recombination with an R-parameter of 0.4. We then required that the energy of the isolated lepton (electron or muon) constituted more than 35% of the visible energy of the jet it was contained within. For electrons it was then required that at least 90% of the total energy of the particle was deposited in the ECAL, and the ratio of energy to momentum for the particle was between 0.75 and 1.25. For muons it was required that less than 35% of the total energy of the particle was deposited in the ECAL, and the ratio of energy to momentum should be between 0.01 and 0.60. The relevant distributions for these variables are shown in Figure 4.4. This method yielded an efficiency of 91% and a purity 74%. Due to the lower purity of this method, leptons selected by this method are referred to as loose selected. Although this approach is not as performant as the first method, it allows more than one lepton to be selected. As a result it is useful for discriminating between signal and background processes (e.g. $ee \rightarrow ZZ \rightarrow qql\bar{l}$) as requirements can be placed on the number of leptons identified by this selection.

In summary, the first method is used to select a single isolated lepton, which is then used for reconstruction, while the number of lepton candidates selected by the second method is used as a discriminating variable to distinguish between signal and background processes.

4.2.2 Jet Finding

Following the lepton finding, the remaining PFOs (not including the isolated lepton) are forced into two jets to reconstruct the properties of the two quarks produced from the hadronic W decay. This was carried out using the exclusive kt algorithm as implemented in FastJet. This is a sequential jet finding algorithm and so follows the following procedure:

1. For each particle calculate it's distance from the beam:

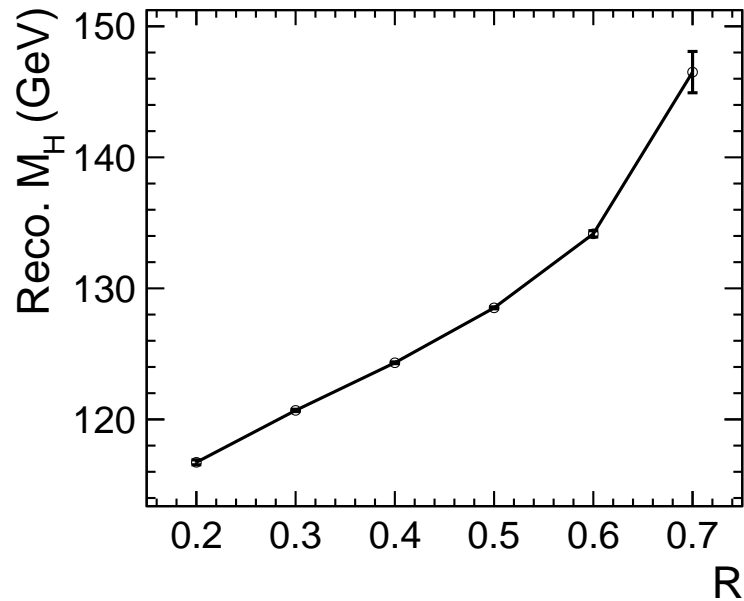


Figure 4.5: Reconstructed Higgs mass as a function of the jet radius parameter when using MC truth to add the neutrino information

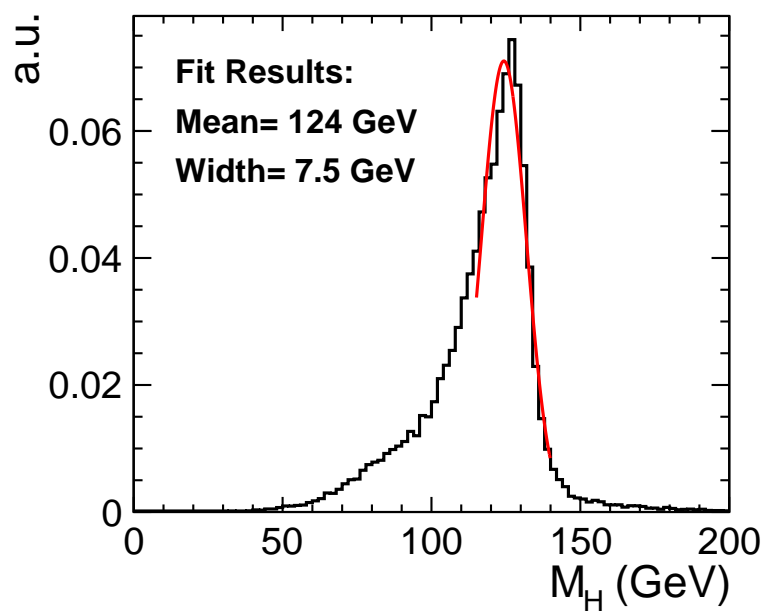


Figure 4.6: Reconstructed Higgs mass for a jet radius of $R=0.4$ using MC truth information to add the neutrino information

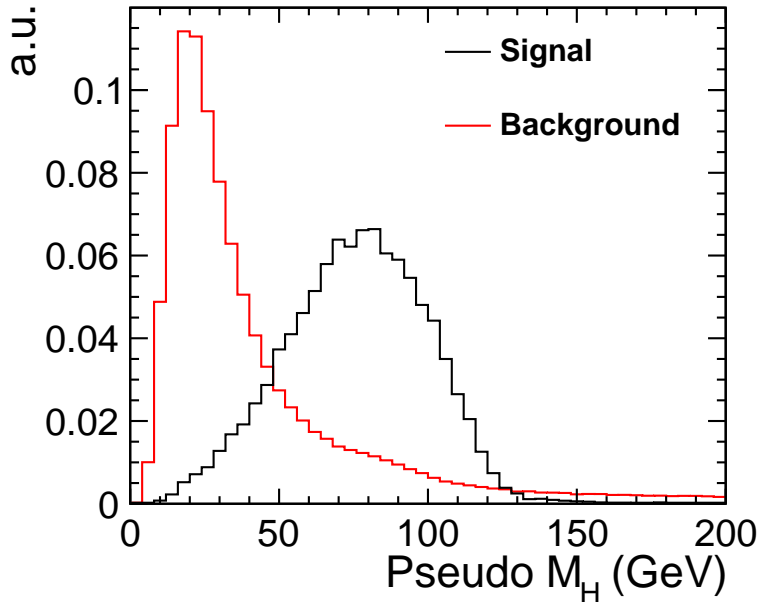


Figure 4.7: Reconstructed invariant mass of the lepton + quark pair system

$$d_{iB} = p_{Ti}^2$$

2. For every pair of particles calculate the distance between them:

$$d_{ij} = \min(p_{ti}^2, p_{Tj}^2) \Delta R_{ij}^2 / R^2$$

where $\Delta R_{ij}^2 = (y_i - y_j)^2 + (\phi_i - \phi_j)^2$, i and j label particles, p_T is transverse momentum, y is rapidity, ϕ is azimuthal angle and R is a tuneable parameter referred to as the jet radius.

3. Find the minimum of all the d_{ij} and d_{iB} . If this corresponds to a d_{ij} then merge particles i and j by summing their four-momenta. If it corresponds to a d_{iB} then declare particle i to be part of the beam and remove it.
4. Repeats steps 1)-3) until there are only the desired number of jets remaining

The optimization of the R-parameter was performed by using Monte Carlo information to obtain what mass would be measured for the reconstructed Higgs for various values of R, when using Monte Carlo truth kinematic information of the lepton

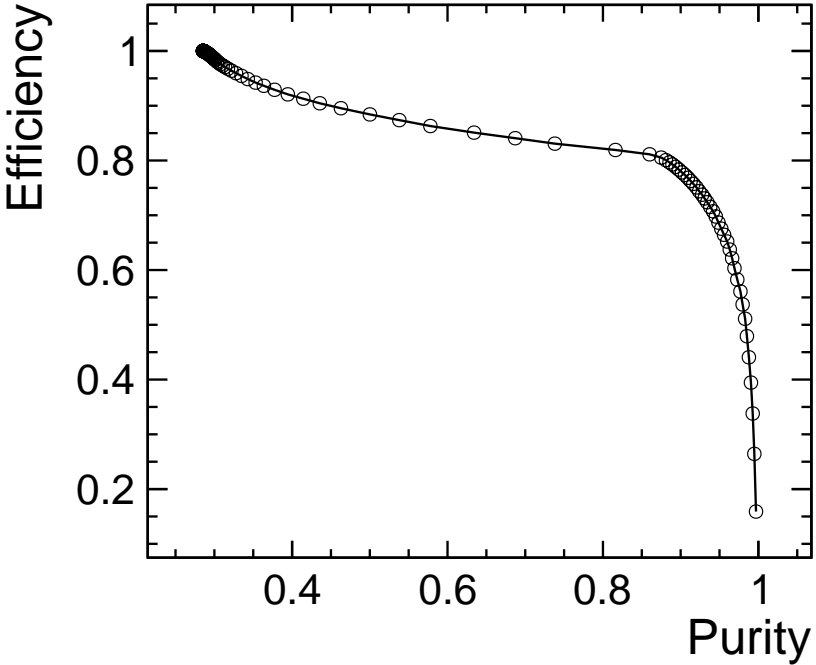


Figure 4.8: Purity vs efficiency for identifying b-jets, obtained from a sample of $Z \rightarrow$ light, c and b quark events simulated at $\sqrt{s} = 1.4\text{TeV}$

neutrino in our reconstruction. The results of this optimization study are shown in Figure 4.5. An acceptably small bias in the reconstructed mass was found for an R value of 0.4, indicating successfully reconstruction of the quark pair. The resulting Higgs mass distribution is shown in Figure 4.6. Note that this mass is only used for optimization of the jet reconstruction. It is never used for the event selection as it is not possible to calculate this mass without using MC truth information. For event selection, the pseudo Higgs mass corresponding to the invariant mass of the lepton and quark pair system is used instead. This is shown in Figure 4.7.

4.3 Flavour Tagging

Flavour tagging of events was performed using LCFIPlus v00-05-02 [49]. Three neural nets were trained to identify u/d/s, b and c quarks respectively with 50,000 $e e \rightarrow Z \nu \nu$, $Z \rightarrow q q$ events used for each neural net. Application of these neural nets

returned two parameters for jets within the event that quantify the probability of the jet being either a b-jet or c-jet. For this analysis, identifying b-jets is more useful for discriminating against the relevant backgrounds. Performance of the b-tagging was evaluated by applying the neural nets to a sample of 150,000 events containing an equal number of $Z \rightarrow$ light, c and b quarks. It can be seen from Fig.4.8 that a purity of 90% can be achieved while still retaining an efficiency of 80%.

4.4 Event Selection

Event selection was performed in two steps. The first of these is referred to as the preselection and acts to remove easily identifiable backgrounds with minimal loss of signal events by applying loose cuts. The cuts used were as follows:

1. Mass of the reconstructed Higgs < 200 GeV
2. At least one loose selected lepton in the event
3. Missing energy of the event must lie in the range 800–1350 GeV
4. Energy of the hadronically decaying W < 600 GeV

With the exception of the upper limit placed on the missing energy, these cuts were optimised for the removal of the two dominant background processes ($ee \rightarrow H\nu\nu$ (non-signal) and $ee \rightarrow qql\nu$.) The upper limit on missing energy is instead designed to remove $e\gamma$ events which are typically collinear to the beam axis and so leave minimal energy in the detector. This cut alone removes approximately half of all $e\gamma$ events. The distribution of the variables associated with these cuts before the preselection is applied are shown for the signal and dominant backgrounds($ee \rightarrow H\nu\nu$ (non-signal) and $ee \rightarrow qql\nu$)in Figure 4.9-4.14 and the resulting efficiencies for the signal and background processes after the preselection is applied are shown in Table 4.16. Along with the cut on the mass of the Higgs, one might naively expect

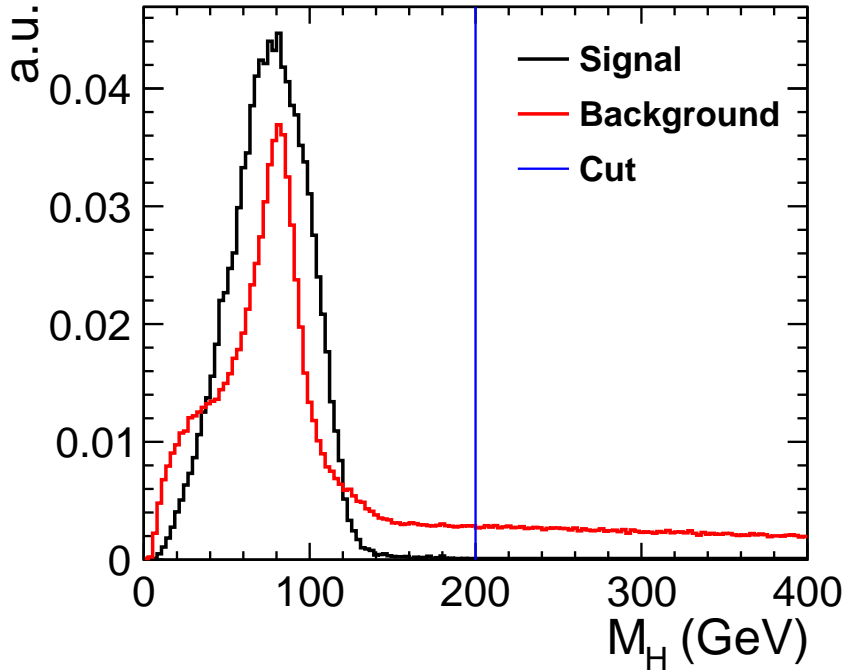


Figure 4.9: Mass of the reconstructed Higgs for the signal process and dominant backgrounds ($ee \rightarrow H\nu\nu$ (non-signal) and $ee \rightarrow qql\nu$)

a similar cut to be placed upon the mass of the reconstructed W. However, due to the relative masses of the Higgs and W the W's produced in the Higgs decay cannot always be on shell. In practice one finds that the kinematically favoured solution is that one W is produced on shell while the second is produced with a mass of ~ 45 GeV. As a result, as can be seen in Figure 4.15, it is challenging to separate background events from signal events in which the hadronically decaying W is produced off shell.

4.4.1 Boosted Decision Trees

Following the preselection, the main event selection is then performed using a multivariate approach that takes into account correlations between variables to maximise the information available for background discrimination. A BDT, implemented in ROOT TMVA [50] was used for performing this stage of the selection. A detailed description of how a BDT works is given in [51]. Fundamentally a decision tree can

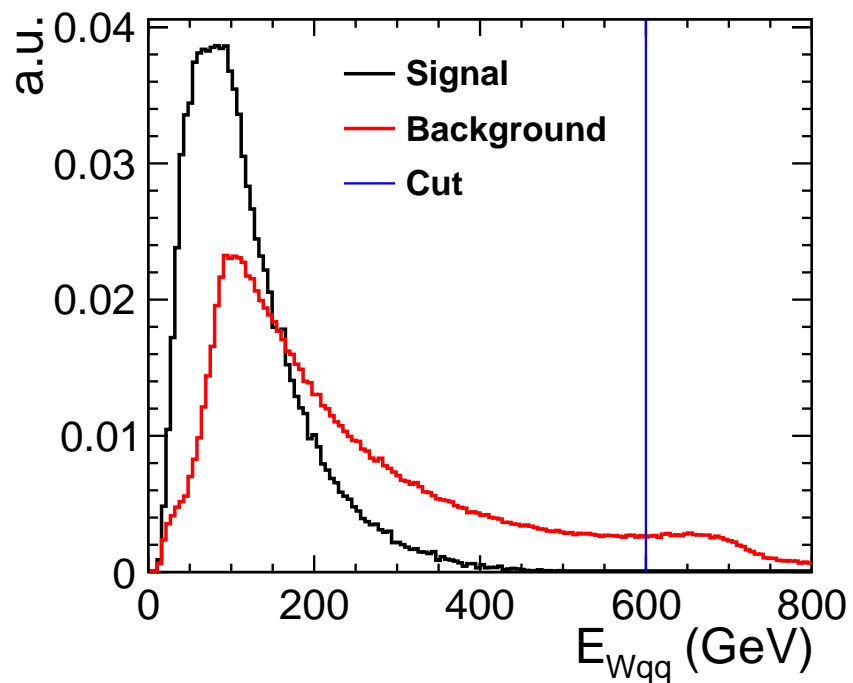


Figure 4.10: Energy of the hadronically decaying W

Figure 4.11: Energy of the hadronically decaying W Boson for the signal process and dominant backgrounds ($ee \rightarrow H\nu\nu$ (non-signal) and $ee \rightarrow qql\nu$)

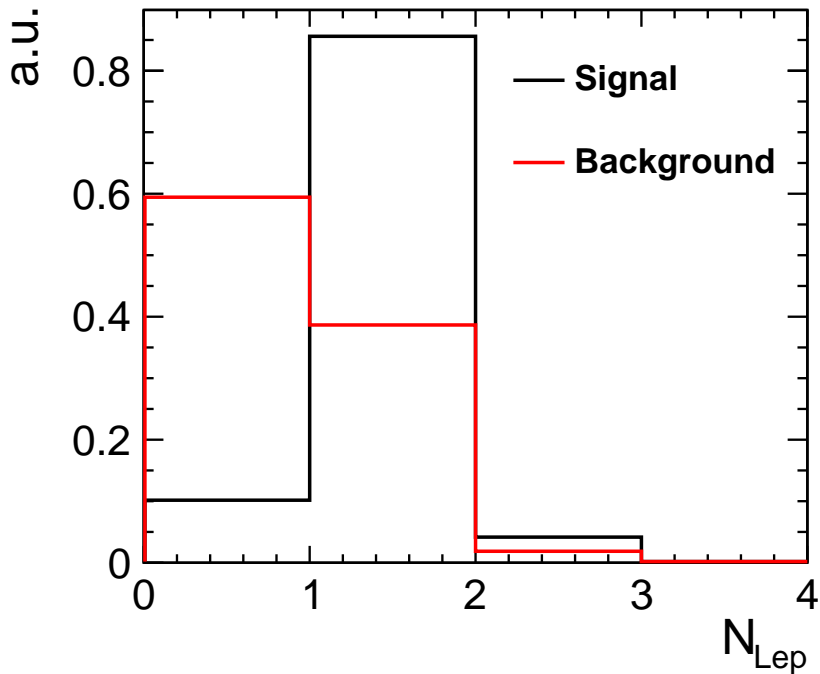


Figure 4.12: Number of loose selected leptons for the signal process and dominant backgrounds ($ee \rightarrow H\nu\nu$ (non-signal) and $ee \rightarrow qql\nu$)

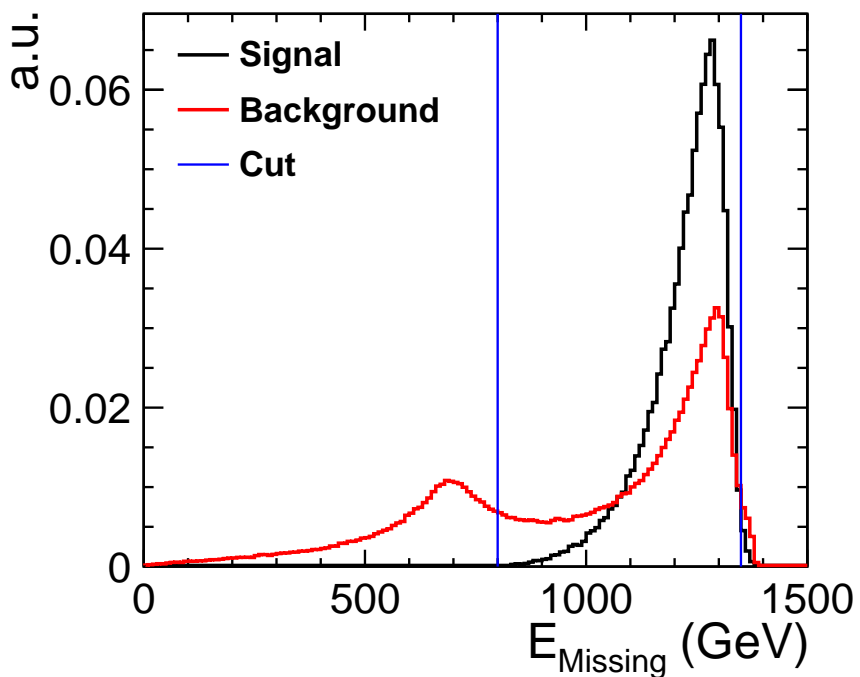


Figure 4.13: Missing energy for the signal process and dominant backgrounds ($ee \rightarrow H\nu\nu$ (non-signal) and $ee \rightarrow qql\nu$)

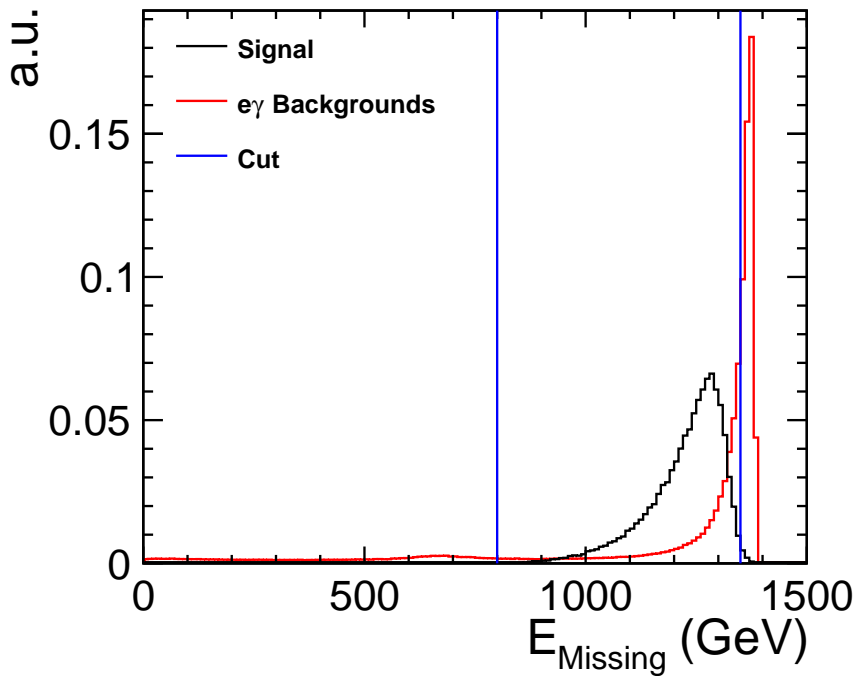


Figure 4.14: Missing energy for the signal process and $e\gamma$ backgrounds

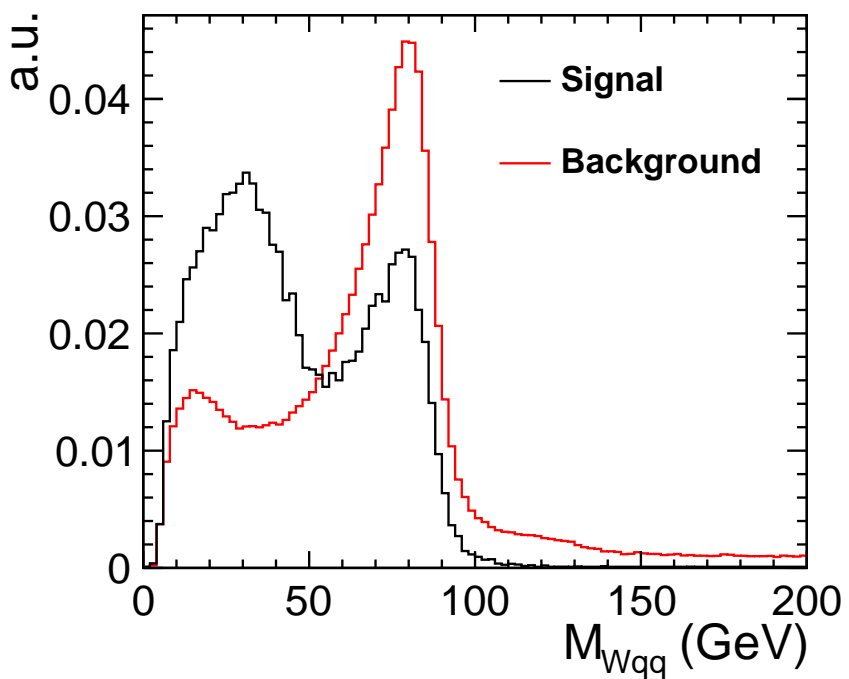


Figure 4.15: Reconstructed mass for the signal process and dominant backgrounds ($ee \rightarrow H\nu\nu$ (non-signal) and $ee \rightarrow qql\nu$)

Process	Cross Section(fb)	Preselection Efficiency (%)
Signal	17.3	89.3
ee \rightarrow H(WW* \rightarrow qqqq) $\nu\nu$	27.4	4.12
ee \rightarrow H(\rightarrow Other) $\nu\nu$	199.4	26.4
ee \rightarrow qq	4009.5	7.21
ee \rightarrow qqqq	1328.1	2.09
e γ \rightarrow eqq (γ from EPA)	32308	7.32
γ e \rightarrow eqq (γ from BS)	56043	8.02
ee \rightarrow qq $\nu\nu$	787.7	9.18
ee \rightarrow qql \bar{l}	2725.8	13.6
ee \rightarrow qql ν	4309.7	7.90

Figure 4.16: Preselection efficiencies

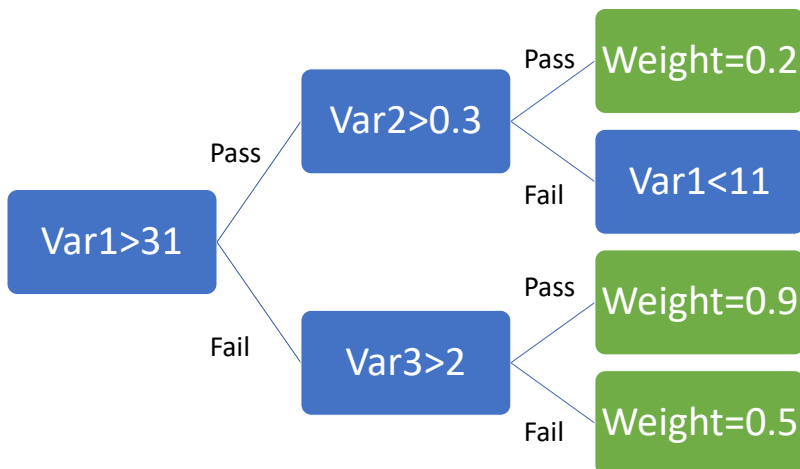


Figure 4.17: Example of a decision tree. Blue represents nodes while green represents leaves

be represented just as a logic flow diagram that assigns a weight to an event based on a series of cuts e.g. see Figure 4.17. Each level of the flow chart is made up of nodes and leafs. A node represents a cut on a particular variable where the specific choice of cut is chosen to be that which provides the greatest separation between signal and background. A leaf on the other hand represents an end point at which a weight (typically the purity of events reaching that point) is assigned to the event. The choice of whether to create a leaf or node after each branching is decided by a stopping criteria. Typically this criteria represents a sufficiently high or low purity of events that the node can be assigned as almost entirely signal or background. Typically not all events will have signal like properties for every variable used. As a result it is normally necessary to produce multiple trees (creatively referred to as a forest) using different combinations of variables for each of the nodes. The sum of weights from all the trees used then forms a final discriminating variable for distinguishing between signal and background events. Boosting is then a way of maximising the performance of the decision trees. The simplest form of boosting is train a set of trees, T_1 , using a sample of NEvents. A second set of trees, T_2 , are then trained using a further N events, half of which are misclassified by T_1 . A third set of trees, T_3 , can then be formed by training on events in which T_1 and T_2 disagree on the classification. The overall classification is then decided by a democratic vote from T_1 , T_2 and T_3 . This method yields an improvement in the performance by focusing the training on events that are the hardest to discriminate. The method can be extended to an arbitrary number of levels T_N where the final BDT score is then a weighted sum of the scores from the N trees. By implementing the preselection cuts before training the BDT the overall background rejection is found to be further improved as again, the BDT is able to focus only on those events that are hardest to discriminate. Within TMVA, the default parameters for the training are to use 850 trees per forest with each tree having a maximum depth of three nodes. This provides a balance between the computational time required to train the classifier and the performance it can achieve however it is possible an improved performance might be achieved by increasing the number of trees per forest or the depth of each tree.

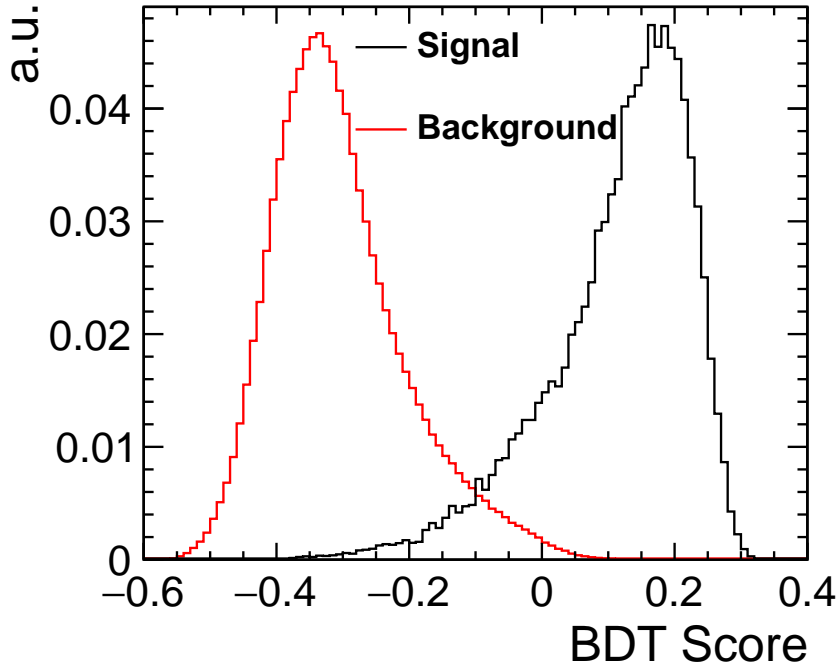


Figure 4.18: BDT response for signal and background events after TMVA classification

The BDT in this analysis used 7×10^4 signal events and 4×10^6 background events, split evenly between training and testing samples. A collection of 19 variables is used for the training: mass of the reconstructed Higgs and W bosons; energy of the W boson; missing energy and transverse momentum; number of isolated leptons selected; PID of the isolated lepton; transverse momentum of lepton; angle of lepton and W boson relative to the beam axis; magnitude of minor thrust value; number of particle flow objects (PFOs) in the two jets; average angle of the two jets relative to the beam axis; kt jet resolution parameter y_{12} ; number of tightly selected PFOs in the event; angular separation of the isolated lepton and the W boson; minimum angular separation and transverse momentum of the lepton relative to either jet, and the combined b-tag value for both jets. The signal and background distributions for every input variable after application of these cuts can be seen in appendix A, and the resulting BDT classifier output can be seen in Fig.4.18.

Figure 4.18 shows that there is a high degree of separation achieved between signal

and background events. The choice of cut on the BDT score was initially chosen to maximise the signal significance ($S/\sqrt{S+B}$) as this corresponds to the lowest statistical uncertainty on $\sigma \times \text{BR}$. Doing this it was found that the maximum significance of 77 was possible by applying a cut on the BDT score of 0.15 corresponding to a statistical uncertainty of 1.30% on $\sigma \times \text{BR}$. However, after later considerations of the relevant systematic uncertainties associated with the measurement (see Section 4.5), it was found that the overall uncertainty could be reduced by imposing a harsher cut of 0.17 on the BDT score resulting in a statistical uncertainty of 1.34% on $\sigma \times \text{BR}$ assuming an integrated luminosity of 1.5 ab^{-1} .

This value is similar to that observed for the $\text{WW} \rightarrow \text{qqqq}$ final state, 1.5%, as expected. By neglecting the case where the isolated lepton is a τ , we have reduced our statistics to two thirds that of the hadronic channel which inherently limits the precision that can be achieved. However, due to the lack of an easily identifiable and the combinatorics associated with assigning the four jets to the two W's, the signal in the qqqq channel is more challenging to distinguish from background events.

Looking in detail at the backgrounds after our selection, we can see that many of the backgrounds have been almost completely removed leaving only $\text{ee} \rightarrow \text{H}(\rightarrow \text{other})\nu\nu$ and $\text{ee} \rightarrow \text{qql}\nu$ as the dominant backgrounds. This is to be expected as these events most closely mimic our signal, which is mainly distinguished by its large missing energy. In the case of $\text{H} \rightarrow \text{other}$ events it was determined that 26% of the remaining events came from $\text{H} \rightarrow \tau^+\tau^-$ processes with a further 25% from $\text{H} \rightarrow \text{WW}^*$ processes with one or more of the Ws decaying to a τ . As such, attempts were made to veto τ events by rejecting events in which one or more hadronically decaying τ was explicitly identified using the default ILCSoft Tau Finder [52] package. However, the number of τ s misidentified in the signal channel was determined to be too high to veto the τ events without significantly increasing the overall statistical uncertainty on $\sigma \cdot \text{Br}$ and so τ identification is not used in the final selection. It is anticipated that in a scenario where CLIC is commissioned, an updated version of the tau finder package would be developed. One obvious improvement that could be made to the finder would be to include particle ID information as determined from pandora for

Process	Cross Section (fb)	Pre-selection Eff.	BDT Cut Eff.	Events After BDT
$ee \rightarrow H\nu\nu; H \rightarrow WW^* \rightarrow qql\nu$	17.3	8.93E-01	3.63E-01	9409
$ee \rightarrow H\nu\nu; H \rightarrow WW^* \rightarrow qqqq$	27.4	4.12E-02	2.03E-03	84
$ee \rightarrow H\nu\nu; H \rightarrow \text{Other}$	199.4	2.64E-01	6.93E-03	2072
$ee \rightarrow qq$	4009.5	7.21E-02	1.72E-05	103
$ee \rightarrow qqqq$	1328.1	2.09E-02	3.37E-05	67
$e\gamma \rightarrow eqq (\gamma \text{ from EPA})$	32308	7.32E-02	1.26E-05	612
$\gamma e \rightarrow eqq (\gamma \text{ from BS})$	56043	8.02E-02	4.54E-06	382
$ee \rightarrow qq\nu\nu$	787.7	9.18E-02	3.41E-04	403
$ee \rightarrow qql\bar{l}$	2725.8	1.36E-01	1.93E-05	79
$ee \rightarrow qql\nu$	4309.7	7.90E-02	4.20E-04	2716
Total Bkg	101738.6	7.82E-02	4.27E-05	6518

Figure 4.19: Efficiency for all processes following pre-selection and BDT response cuts and the number of events expected to satisfy these requirements, for an integrated luminosity of 1.5 ab^{-1} .

identifying taus. With a sufficiently reliable tau finder, up to 50% of the current backgrounds could potentially be removed.

The efficiency for selecting $WW^* \rightarrow qqqq$ events in the $WW^* \rightarrow qql\nu$ channel has been calculated to be 0.2%. The converse efficiency for selecting $WW^* \rightarrow qql\nu$ events in the $WW^* \rightarrow qqqq$ channel is 1.0% which should be sufficiently low that a straightforward combination of the uncertainties determined by both channels can be made. The resulting combined statistical uncertainty on $ee \rightarrow H\nu\nu, H \rightarrow WW^*$ is thus 1.0%.

4.5 Systematics

On top of the statistical uncertainty there will also be systematic uncertainties on the measurement. These primarily arise from the fact that in order to perform the

$\sigma_{H\nu\nu} \times BR_{H \rightarrow WW}$ measurement we must first subtract any remaining backgrounds after our event selection, then correct for finite signal efficiency, before finally scaling by the $WW \rightarrow q\bar{q}\nu\bar{\nu}$ branching ratio. The effects that have been quantified are as follows:

Luminosity— At CLIC it is estimated that the luminosity can be measured to 0.3%. Deviations from the nominal value will cause two problems. Firstly the cross section measurement itself will be directly effected as $\sigma = N/L$. Secondly, the number of background events recorded will differ from that which is predicted. As a result the background subtraction will either no longer remove all the background or will remove all the background but also remove some signal events too. The effect of the luminosity uncertainty was quantified by fluctuating the total number of events after event selection by $\pm 0.3\%$ before doing the background subtraction and efficiency corrections then measuring the variation seen in the measured cross section. This resulted in an uncertainty of 0.51% on $\sigma_{H\nu\nu} \times BR_{H \rightarrow WW}$.

Background Normalization— In order to remove the backgrounds remaining after the event selection a precise knowledge of the overall background normalization is required. For all the backgrounds there will be an uncertainty associated with their cross section. To evaluate the effect of these uncertainties, the number of events passing for each background process were fluctuated independently and the resulting change in $\sigma_{H\nu\nu} \times BR_{H \rightarrow WW}$ was determined. The uncertainties from changing each of the backgrounds individually were then added in quadrature to get the total uncertainty on the background normalization. In the case of Higgs related backgrounds a fluctuation of 5% was used for the normalization. This value was motivated by the studies presented in [1] where a statistical uncertainty of $\mathcal{O}5\%$ is expected on the dominant Higgs decays modes for Higgs produced through WW -fusion at 1.4 TeV. For the remaining backgrounds fluctuations of the order 1% were used instead. Overall this is found to give a combined uncertainty of 1.14% on $\sigma_{H\nu\nu} \times BR_{H \rightarrow WW}$ making the dominant systematic effect. The minimization of this uncertainty is the basis for increasing the cut on the BDT score. For the BDT score minimising the statistical uncertainty it was found that the systematic uncertainty

from the background normalization was $\mathcal{O}2\%$ due to a larger total number of backgrounds passing the event selection. Hence we see that for a small degradation in the statistical uncertainty we gain a large improvement in the systematic uncertainty.

W Branching Ratios– In order to measure $\sigma_{H\nu\nu} \times BR_{H \rightarrow WW}$ it is necessary to correct for the $WW \rightarrow qql\nu$ branching ratio. This quantity is already well measured with an uncertainty of 0.09% (0.27%) for the leptonic (hadronic) decay modes. This gives an uncertainty on the branching ratio $WW \rightarrow qql\nu$ and $\sigma_{H\nu\nu} \times BR_{H \rightarrow WW}$ of 0.57%.

As well as these uncertainties there will be other effects that have not been able to quantified. In particular, it would be beneficial to examine the effect of using a different event generator/hadronization scheme to see the effect of modelling on the variables used for performing the event selection. However there, are currently no alternative packages available within the linear collider framework and so there is no quantification made for these effects. Overall it is believed that the effect of different MC models should be small when compared to the other systematic effects as few of the input variables for training the BDT are expected to be sensitive to modelling effects.

Combining the various systematic effects leads to a total systematic uncertainty of 1.37%. This is of the same order as the statistical component (1.34%). Ultimately it is expected that these values probably represent an underestimate of the performance that CLIC will achieve as advances in analytical techniques will likely occur over the time scale (~ 20 years) before this measurement would actually be performed allowing for improved event reconstruction and background rejection.

4.6 Impact on CLIC Higgs Measurements

As discussed at the start of this chapter, the main motivation behind performing this measurement is to allow the Higgs width to be determined so that model independent

Process	Statistical Precision at 1.4 TeV (%)
$X_1 = \sigma_{ZH} \propto g_{HZZ}^2$	1.7
$X_2 = \sigma_{H\nu\bar{\nu}} \times BR(H \rightarrow WW^*) \propto \frac{g_{HWW}^4}{\Gamma_H}$	1.0
$X_3 = \sigma_{H\nu\bar{\nu}} \times BR(H \rightarrow b\bar{b}) \propto \frac{g_{HWW}^2 g_{Hbb}^2}{\Gamma_H}$	0.4
$X_4 = \sigma_{ZH} \times BR(H \rightarrow b\bar{b}) \propto \frac{g_{HZZ}^2 g_{Hbb}^2}{\Gamma_H}$	0.9

Figure 4.20: Expected precision on input quantities for the Higgs width measurement

measurements of the Higgs couplings can be performed. As a result we should look at this measurement in terms of the other measurements required for measuring the Higgs width.

One can see from 4.20 that the width measurement is not limited by the $\sigma_{H\nu\bar{\nu}} \times BR_{H \rightarrow WW}$ measurement, instead it is limited by the precision on the higgstrahlung cross section as measured during the low energy run. Overall, combining the measurements we expect a statistical uncertainty of 3.7% on the Higgs width at 1.4 TeV for 1.5 ab^{-1} of data.

4.7 Conclusion

In summary, we have performed a full analysis of the $e e \rightarrow H(WW^*)\nu\bar{\nu}$, $WW^* \rightarrow q\bar{q}l\nu$ decay channel using a large set of backgrounds with the aim of measuring the $H \rightarrow WW^*$ branching ratio as input for a model independent of the total Higgs width. A 19 variable BDT was used to select signal events where the final state charged lepton is either an electron or a muon, and to remove background which was found to be dominated by $e e \rightarrow H(\rightarrow \text{Other})\nu\bar{\nu}$ and $e e \rightarrow q\bar{q}l\nu$ in the final selection. Several systematic effects have been considered with the dominant uncertainty coming from the background normalization. The resulting uncertainty for 1.5 ab^{-1} of data at 1.4 TeV was found to be:

$$\delta\sigma_{H\nu\bar{\nu}} \times BR(H \rightarrow WW^*) = 1.34\%_{\text{Stat}} \oplus 1.37\%_{\text{Syst}}$$

The efficiency for incorrectly selecting $ee \rightarrow H(WW^*)\nu\nu$, with $WW^* \rightarrow qqqq$, in the $WW^* \rightarrow qql\nu$ channel, was found to be 0.2%. The correlated overlap in selections developed for the $WW^* \rightarrow qqqq$ and $WW^* \rightarrow qqlv$ final states would be taken into account when combining the individual results, however the combined statistical precision is expected to be 1.0%. Combining this with the other proposed measurements at 1.4 TeV and the low energy stage at CLIC this yields an overall statistical precision of 3.7% on the total Higgs width.

CHAPTER 5

Top Physics

5.1 Introduction

Here we give details of an analysis proposed for measuring the top quark forward-backward asymmetry, A_{FB}^t , at CLIC during the 1.4 TeV stage.

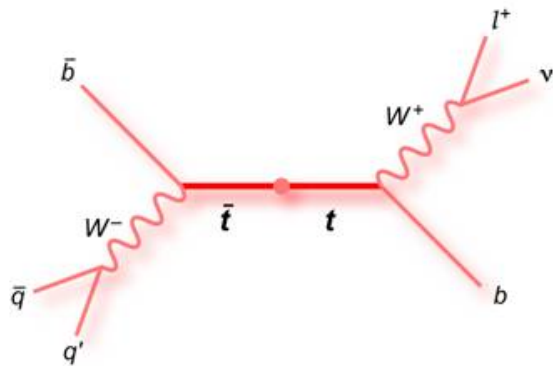


Figure 5.1: Semileptonic $t\bar{t}$ decay

Decay Mode	Branching Fraction (%)
Fully Hadronic, $t\bar{t} \rightarrow WbWb \rightarrow qqbqqb$	45.3
Semileptonic, $t\bar{t} \rightarrow WbWb \rightarrow qqbl\nu b$	43.8
Fully Leptonic, $t\bar{t} \rightarrow WbWb \rightarrow l\nu bl\nu b$	10.6
$t\bar{t} \rightarrow Other$	0.4

Table 5.1: Top Pair Decay Modes

As already described in Chapter 3, A_{FB}^t is sensitive to the electroweak form factors of the $t\bar{t}X(X=Z,\gamma)$ vertex. By measuring A_{FB}^t and the $t\bar{t}$ cross section at multiple energies and with different beam polarizations it is possible to extract values for the electroweak form factors and use these as a probe for testing the SM. This measurement is well motivated by the existing result for the b quark forward-backward asymmetry as measured at LEP, which currently provides the largest deviation from the SM within electroweak fits. Due to the limited energy at LEP (which is still the highest energy e^+e^- collider to have existed,) no analogous measurement of the asymmetry for tops has ever been performed at a lepton collider.

A_{FB} is defined as:

$$A_{FB}^t = \frac{N_F - N_B}{N_F + N_B} \quad (5.1)$$

Where N_F and N_B are the number of top quarks produced in the forward and backward directions, which are defined to be the hemispheres corresponding to an angle of less than and greater than 90° relative to the electrons initial momentum respectively.

As tops decay almost exclusively to a W and b (99.8% of decays) they are typically described in terms of the resulting decay modes of the Ws. The dominant decay modes are described in Table 5.1. Here we will look at measuring A_{FB}^t using the semileptonic $t\bar{t}$ decay channel (see Figure 5.1) in which one of the W's decays to a lepton and neutrino and the other W decays to a pair of quarks. This decay mode is ideal for determining A_{FB}^t as the lepton from the leptonically decaying top

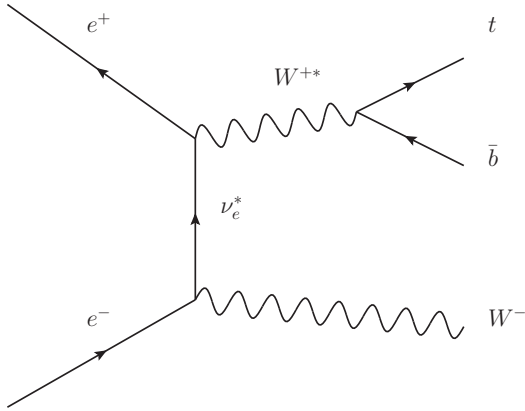


Figure 5.2: Dominant single top production mode capable of mimicking the signal process

provides the ability to charge tag the top while the hadronic decay allows an accurate measurement of the production angle of the top. Due to the sensitivity of A_{FB}^t to polarization states, the measurement will be done for two different electron beam polarizations, -80% and +80%, assuming an even split of luminosity between the two configurations. The dominant signal and background processes examined by this analysis, as well as their cross sections and internal CLIC production ID numbers for each polarization are shown in Tables 5.2 and 5.3. All samples are simulated using the CLICILD_CDR detector model, a variation of the ILD detector model developed for the ILC. The samples also include an overlay of $\gamma\gamma \rightarrow$ hadron events from beamstrahlung based on a 30 ns window around the generated physics events. Because these are inclusive samples, before they can be used for this analysis the $e^+e^- \rightarrow qqqql\nu$ samples must be filtered to extract the signal process. This is done by trying all combinations of qqq and $ql\nu$ and seeing if there is any case in which the resulting particles both have masses within $5 \times \Gamma_t$ of m_t , where within the generator m_t and Γ_t are 174 GeV and 1.4 GeV respectively. In the case that two tops could not be simultaneously identified, the event is described as either single top or non top depending on whether any single combination of qqq or $ql\nu$ is in the correct mass window. The dominant backgrounds are expected to be from alternative $t\bar{t}$ decays (fully hadronic decay modes and semileptonic decays containing taus) and from single top events (see Figure 5.2) which will have similar topologies due to the fact they can both contain a hadronically decaying top.

Process	Cross Section(fb)	Production ID	Events Used (10^{-3})
$e^+e^- \rightarrow qqqql\nu$	142.3	6589, 6592, 6634, 6637	3860
$e^+e^- \rightarrow qqqqqq$	116.4	6595, 6598, 6601, 6604, 6610, 6607, 6613, 6616, 6619, 6622	310
$e^+e^- \rightarrow qql\nu l\nu$	44.1	6586, 6625, 6628, 6631	100
$e^+e^- \rightarrow qqqq$	2304.0	8254	1,590
$e^+e^- \rightarrow qql\nu$	6975.0	7477	3,520
$e^+e^- \rightarrow qql l l$	2681.0	8244	1,190
$e^+e^- \rightarrow qq\nu\nu$	1395.0	8271	1,120
$e^+e^- \rightarrow qq$	4843.0	8283	2,400

Table 5.2: Samples used in the -80% electron beam polarization study

Process	Cross Section(fb)	Production ID	Events Used (10^{-3})
$e^+e^- \rightarrow qqqql\nu$	53.5	6646, 6697, 6691, 6694	160
$e^+e^- \rightarrow qqqqqq$	44.9	6652, 6655, 6658, 6661, 6664, 6667, 6670, 6673, 6676, 6679	198
$e^+e^- \rightarrow qql\nu l\nu$	15.3	6643, 6682, 6685, 6688	15.3
$e^+e^- \rightarrow qqqq$	347	8257	500
$e^+e^- \rightarrow qql\nu$	1640	7480	1,000
$e^+e^- \rightarrow qql l l$	2530	8241	1,000
$e^+e^- \rightarrow qq\nu\nu$	180	8274	200
$e^+e^- \rightarrow qq$	3170	8286	1,500

Table 5.3: Samples used in the +80% electron beam polarization study

The results presented here are currently being included in a paper summarising the top physics potential at CLIC[2], however this paper is still under review. Within the paper, an alternative version of this analysis performed by Lars Rickard Ström (CERN) in which an alternate reconstruction method and event selection are implemented. The results of both analysis have been found to yield consistent results for the expected precision on A_{FB}^t when accounting for the lower signal efficiency in the alternate analysis.

5.2 Event Reconstruction

Reconstruction of signal events is performed using ILCSOFT v01-17-10 and consists of three main stages. The first stage is to identify isolated leptons arising from the leptonically decaying top. These leptons are then removed and the remaining PFOs are resolved into two large radius “fat jets”. The two fat jets must then be associated with either the b jet produced by the leptonically decaying top or to the combination of three jets arrising from the hadronically decaying top. A kinematic fitter is then used to reconstruct the neutrino and any Initial State Radiation (ISR)/BS photons present in the event. Throughout the analysis only tight selected PFOs have been considered in the reconstruction (PFOs reconstructed using with a timing cut of $\sim 2\text{ns}$ placed on clusters in the detector[53]) so as to reduce beam backgrounds.

5.2.1 Lepton Finding

Lepton finding is the first stage of reconstruction performed in each event. Due to the fact the measurement of A_{FB}^t is entirely reliant on using the lepton charge to distinguish between top and antitop decays, it is essential that a high efficiency and purity are achieved and that there is no angular dependence on the performance. For this analysis lepton finding is done in two steps. Firstly, lepton candidates with energy $> 10 \text{ GeV}$ are identified using the particle ID provided by the Pandora

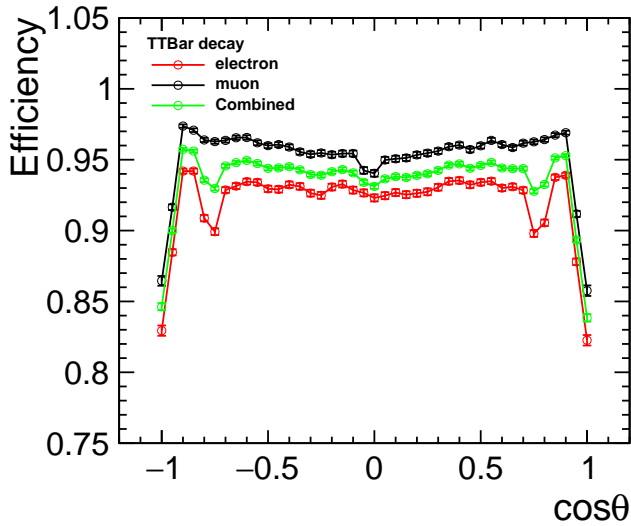


Figure 5.3: Efficiency for identifying leptons with the correct charge as a function of angle

Particle Flow Algorithm [25]. Only muons and electrons are examined due to the fact tau leptons require different reconstruction techniques to identify and are typically reconstructed with significantly lower efficiency. This first stage removes $> 90\%$ of fake candidates with negligible impact on efficiency. The second stage of lepton selection is to examine how isolated each of the candidates are. This is evaluated by resolving all PFOs in the event into five jets, then for each lepton candidate measuring the energy of the candidate relative to the jet it was been associated with. For this process the inclusive ee kt algorithm was chosen for the jet finding to ensure that all lepton candidates are always placed within a jet. The lepton candidate found to have the highest ratio of $E_{Candidate}/E_{Jet}$ is then declared to be the isolated lepton arising from the leptonically decaying top. In the case that no lepton is selected by the first step, the restrictions on the particle ID and energy are relaxed and the lepton is selected purely based on which PFO is the most isolated according to step two. This method ensures that there is always exactly one lepton selected per event. The net efficiency with which this method selects a candidate with the correct charge is found to be 93% for electrons and 96% for muons.

As well as understanding the net efficiency for finding leptons it is also important

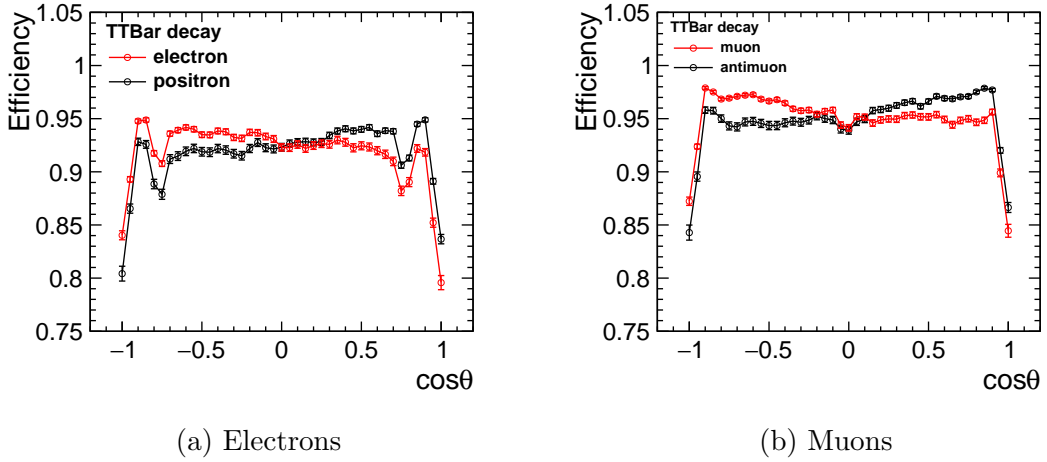


Figure 5.4: Angular dependence of lepton finding for particles vs antiparticles.

to examine the angular dependence of the efficiency to ensure there is no bias that could effect the measurement of A_{FB}^t . Figure 5.3 shows how the efficiency varies with angle. The efficiency is seen to rapidly decline for $|\cos\theta| > 0.9$ due to the detector acceptance. A decrease in efficiency is also seen for electrons at angles corresponding to the transition point between the ECAL barrel and endcaps. This effect is not seen for muons as they are also reconstructed using the muon detectors placed at a larger radius. Overall the efficiency is seen to be consistently worse for electrons than muons. This is to be expected as muons produce easily recognisable signatures in the detector due to the fact they typically penetrate through the tracker, ECAL, HCAL and muon systems whereas electrons only leave deposits in the tracker and ECAL. In the case that tracks are lost during reconstruction or are wrongly associated to other PFOs it is then possible for photons to wrongly be labelled as electrons and vice versa leading to a higher fake rate for electrons.

As well as checking the angular dependence of the charge tagging efficiency it is also key to examine the charge dependence of the lepton finding to make sure there is no preference for identifying particles over antiparticles. The angular dependence of the charge tagging efficiency for particles vs antiparticles is shown in Figure 5.4. An asymmetry in the performance is observed for both electrons and muons.

This arises from the underlying asymmetry in the production of particles vs antipar-

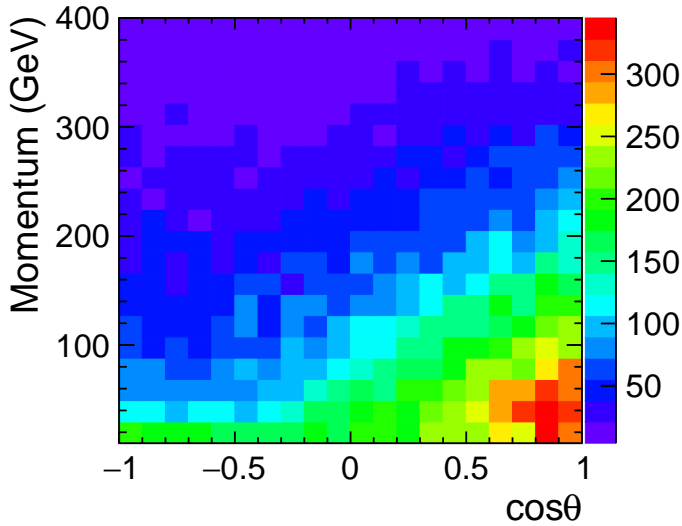


Figure 5.5: Correlation between lepton momentum and angle for positrons only.

ticles due to forward-backward asymmetries. The top forward backward asymmetry means that tops are preferentially produced in one direction while antitops are produced more often in the opposite direction, however due to charge conservation this also means that the W bosons and leptons are produced asymmetrically too. Because the collisions are taking place well above the top pair production threshold, the W bosons will gain a large boost forcing them to travel in the same direction as the initial top. The polarization of the W means that the lepton will also be preferentially produced along the same direction as the W and can only be produced in the opposite direction with a lower energy. Overall this means that leptons are produced with higher energy in one direction and lower energy in the opposite direction while for antileptons this directional dependence is reversed. The effect is shown in Figure 5.5 where it is seen that positrons are produced with higher energy in the forward direction ($\cos\theta > 0$) than the backward direction. It is known that the efficiency for reconstructing leptons at CLIC increases with energy and so the fact the energy and angle at which leptons are produced are correlated results in the asymmetric angular efficiency for correctly reconstructing the lepton. Further evidence for this theory is shown in Figure 5.6 and 5.7 which show that the asymmetry disappears when either the production mode for the leptons is symmetric or when low energy leptons are not included.

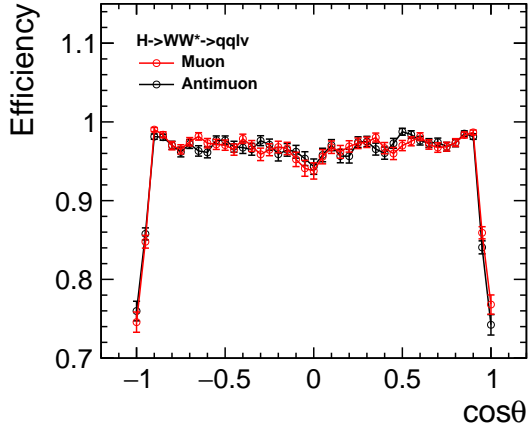


Figure 5.6: Charge tagging efficiency for $ee \rightarrow H\nu\nu, H \rightarrow WW \rightarrow qql\nu$. The efficiency is seen to be symmetric for particles and antiparticles when they are produced with the same initial angular distribution.

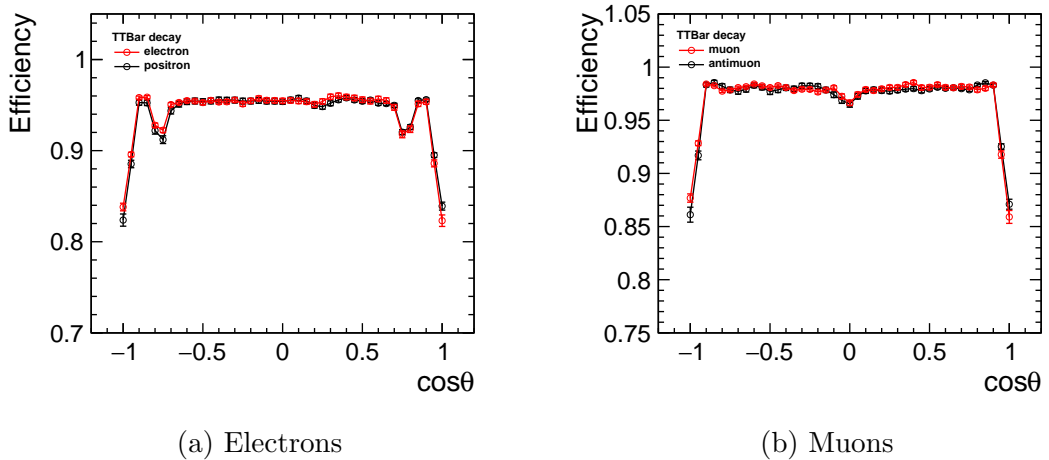


Figure 5.7: Charge tagging efficiency after 20 GeV lepton momentum cut. The efficiency is seen to be symmetric for leptons with momentum > 20 GeV.

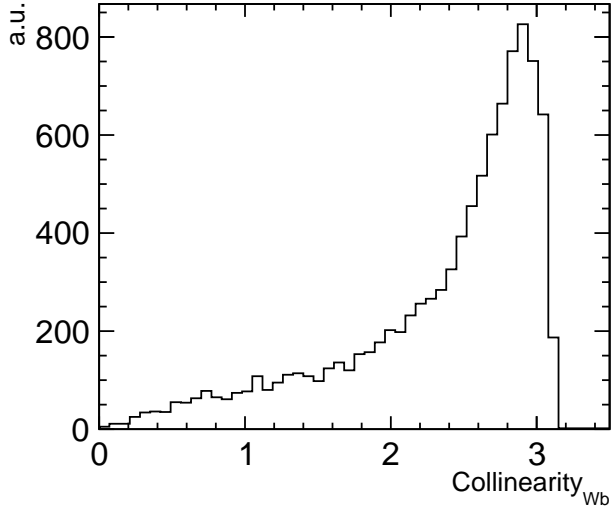


Figure 5.8: Separation between W and b jets from top decay. The pair are typically too collimated to allow the b-jet and the pair of jets from the W decay to be successfully resolved into three distinct jets.

5.2.2 Fat Jet Finding

Jet reconstruction was performed using the FastJet package [48]. Due to the high energy of the collisions relative to the top mass, the tops produced are highly boosted and produce highly collimated decay products (see Figure 5.8.) This means it is typically not possible to resolve the decay products from the hadronically decaying top into three jets corresponding to the b-jet and light quark jets from the W decay. As a result an alternative approach to jet reconstruction is considered based on the concept of fat jets, an approach already being used at the LHC[54]. Fat jets are large radius jets and are used to cluster groups of jets that can't be accurately resolved individually into one larger jet. For the purpose of this analysis the events are clustered into two fat jets which should correspond to the b-jet from the leptonically decaying top and to the whole set of decay products from the hadronically decaying top. The mass and substructure (see Section 5.4) of these fat jets can then be used to distinguish genuine top events from backgrounds. Two jet algorithms were considered for reconstructing the fat jets- the longitudinally invariant kt algorithm [55] and Valencia algorithm [56]. The kt algorithm is already extensively used at

hadron colliders while the Valencia algorithm is a newer algorithm designed for future lepton colliders that offers improved performance in handling beam backgrounds. A full description of the kt algorithm is already given in Section 4.2.2 so here we will only describe the Valencia algorithm. Overall the Valencia algorithm is similar to the kt algorithm, however the key differences are that the inter-particle distance and beam distance are redefined as:

$$d_{ij} = \min(E_i^{2\beta}, E_j^{2\beta})(1 - \cos\theta_{ij})/R^2 \quad (5.2)$$

$$d_{iB} = p_T^{2\gamma} E^{2(\beta-\gamma)} \quad (5.3)$$

Where R is the usual jet radius defined in the same way as for the kt algorithm and β and γ are additional parameters that can be used to tune how the algorithm behaves for particles approaching the beam line. Figure 5.9 shows how the ratio d_{ij}/d_{iB} develops for a pair of particles produced with fixed energy and angular separation as a function of their polar angle for multiple β factors. One can see that a higher β factor introduces a larger penalty for approaching the beam line leading to a decreased chance for the particles to be merged into a jet.

The performance of both algorithms is shown in figure Figure 5.10. For both algorithms it is seen that at higher R the resolution on the top mass gets worse while for lower R sub-peaks start to appear in the mass distribution corresponding to partial reconstructions of the top (either a W Boson or single quark). The kt algorithm is seen to produce a consistently broader distribution in the top mass. Placing a cut on the collision energy of $E > 1.2$ TeV reveals that these lower mass peaks only occur for lower collision energies where the tops will no longer be produced back to back and their decay products will be less collimated. As a result the fat jet finding can merge components from both the hadronic and leptonic tops into each jet. This analysis will be focusing on reconstructing the most boosted tops. As a result the Valencia algorithm is preferred due to its better mass resolution. Performance for

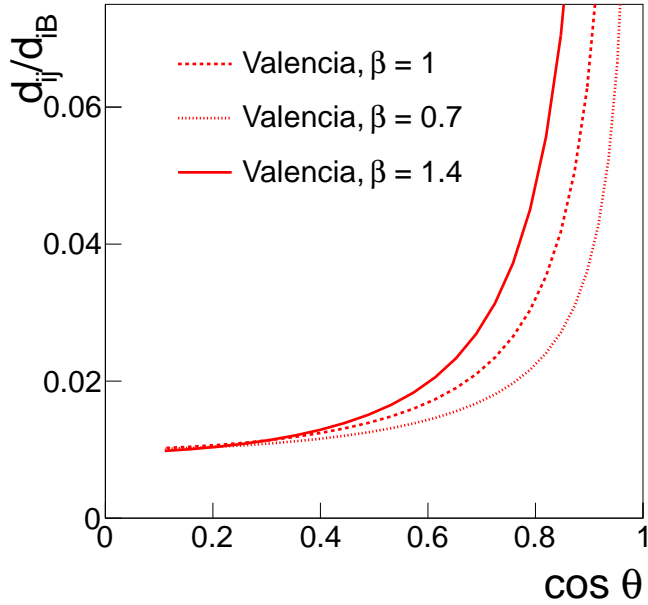


Figure 5.9: Effect of the Valencia β parameter on d_{ij}/d_B for a pair of particles produced at a fixed energy and angular separation as a function of their polar angle[56].

less boosted top decays might be improved by examining the performance of a more conventional jet analysis looking to resolve all four individual quarks whenever the fat jet finding produces jets outside the top mass window. This possibility is not examined here but represents a possible improvement for low $\sqrt{s'}$ events. Here the Valencia algorithm with $R=1.5$, $\beta=1$ and $\gamma=1$ is chosen as the optimal jet reconstruction method to provide a balance between mass resolution and the frequency of partial reconstructions.

5.2.2.1 Jet Association

After the fat jet finding has been performed, the two reconstructed jets must then be associated as either coming from the hadronically decaying top or from the b jet from the leptonically decaying top. The default method for this was to associate the highest energy fat jet to the hadronically decaying top, as due to the neutrino not being reconstructed and the lepton already being removed, the remaining decay products from the leptonically decaying top should typically have considerably less

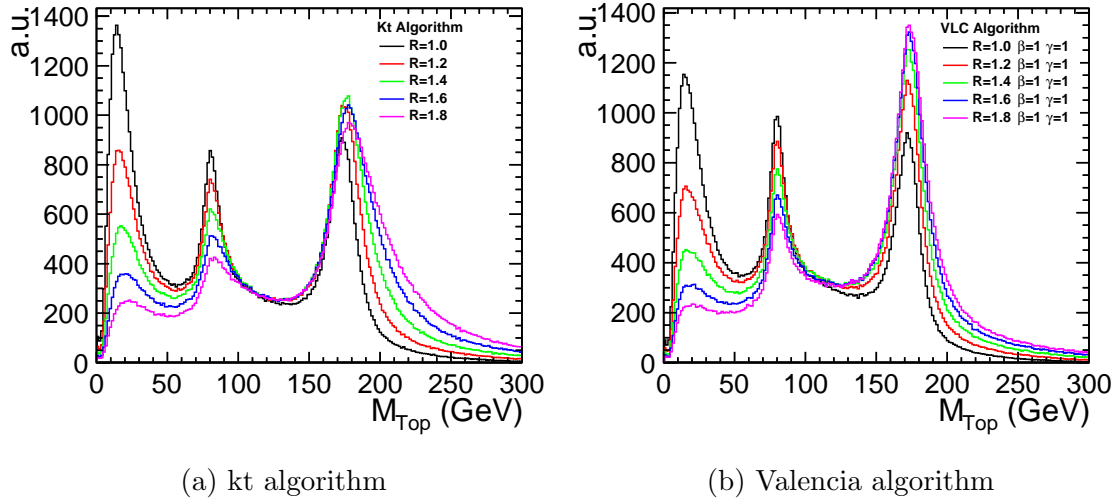


Figure 5.10: Performance of both jet finding algorithms for various parameter settings. The k_t algorithm is seen to produce a broader distribution in the top mass peak so the Valencia algorithm is preferred. For both methods it is seen that a lower R results in the development of peaks from partial reconstruction of the top jet (W Boson or single quark) while a larger R produces a broader peak at the top mass. A balance is found between producing a narrow top mass width while minimising sub peaks by selecting a radius of $R=1.5$

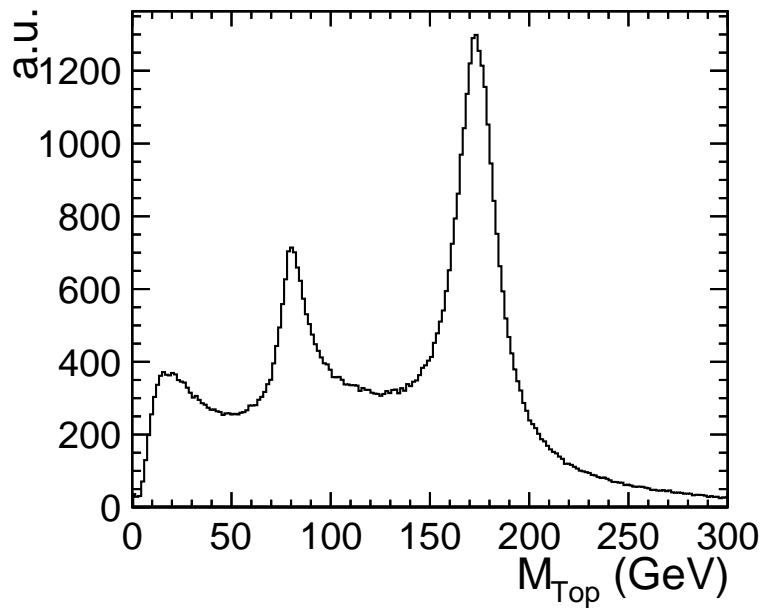


Figure 5.11: Reconstructed top mass for the Valencia algorithm in events close to the nominal collision energy ($E > 1.2$ TeV)

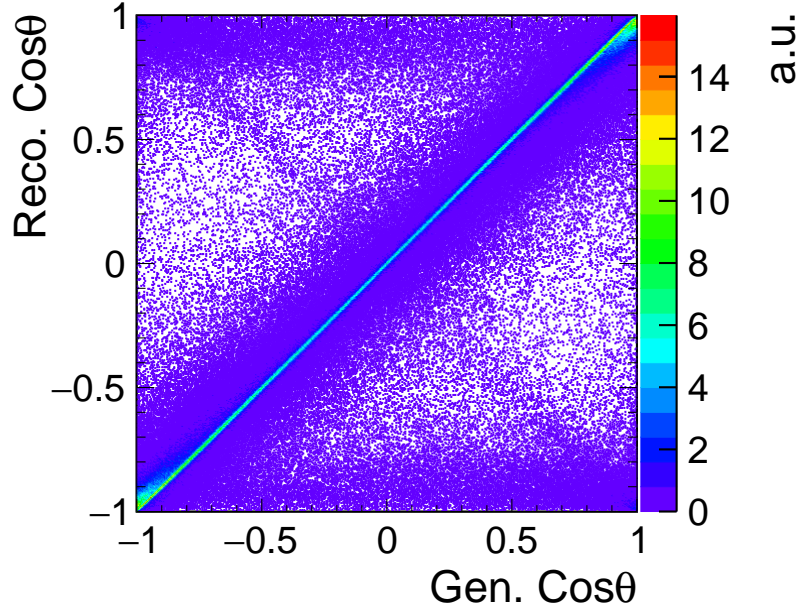


Figure 5.12: Comparison of reconstructed top decay angle to generator level. A strong correlation is seen over most of the range, however this starts to break down for large angles of $| \cos\theta | > 0.9$ where non-negligible off diagonal contributions are seen.

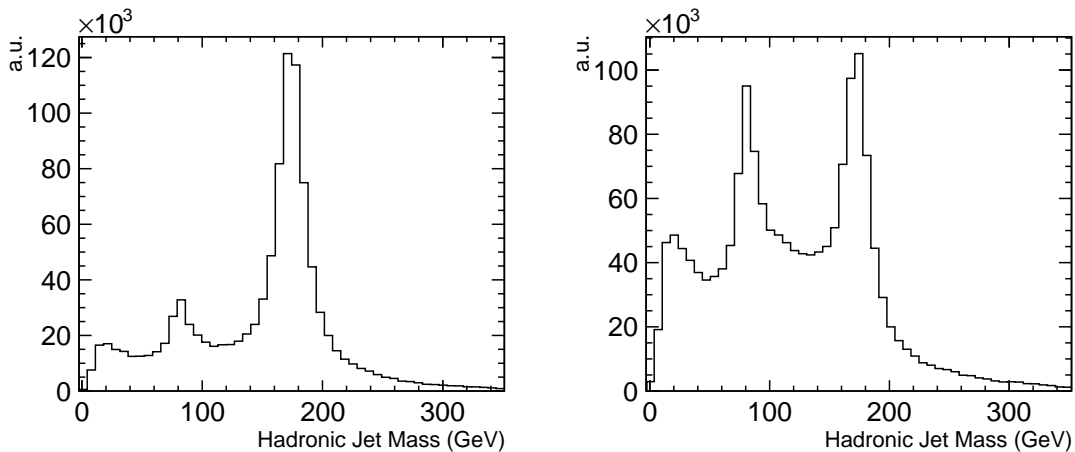
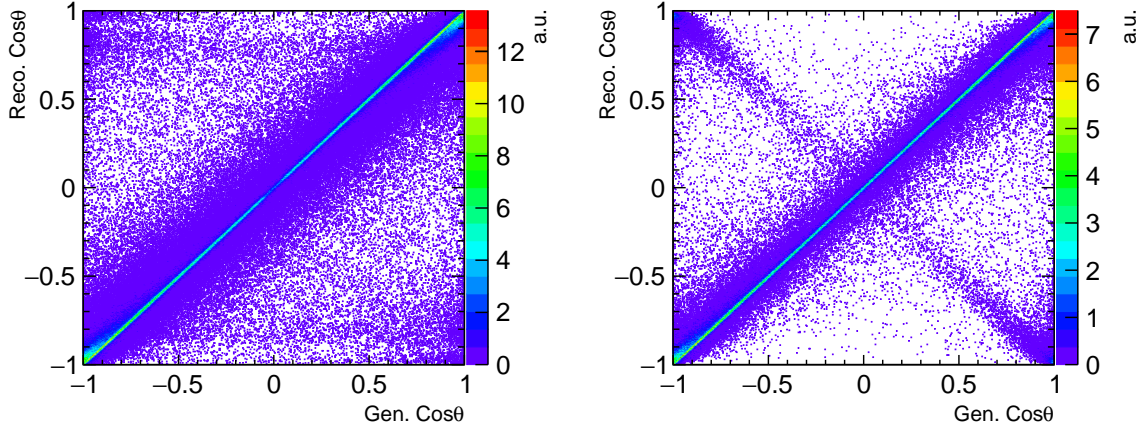


Figure 5.13: Reconstructed fat jet mass. Left: for the on diagonal elements of Figure 5.12) where $| \frac{\cos\theta_{Reco}}{\cos\theta_{Gen}} | > 1$, the reconstructed fat jet matches the top mass. Right: in the regions corresponding to the off diagonal elements, the mass is no longer consistent.

energy. The performance of this method can be examined by comparing the reconstructed decay angle relative to the generator value (see Figure 5.12). While the performance over most of the range studied is good, for $| \cos\theta | > 0.9$ the correlation between the generator and reconstructed angles breaks down and off diagonal elements start to appear. Performance in these forward regions is typically poor due to the detector acceptance which result in losses down the beam line. In cases where parts of the hadronic top decay are not able to be reconstructed, using the fat jets energy to perform the jet association no longer becomes a reliable method. Evidence that misreconstruction is the source of these off diagonal elements is presented in Figure 5.13 where it is clear that the fat jets in the off diagonal regions are not reconstructed with a consistent mass. If the jets are not fully reconstructed, it is more likely that the wrong jet is assigned to be from the hadronic top. When the wrong jet is selected the reconstructed angle will be approximately π radians off the generator value as the tops are predominantly produced back to back. This explanation is further supported by the results shown in Figure 5.14a which show that the off diagonal elements can be removed when a cut is placed on the angle between the reconstructed top and the generator level b jet from the leptonic top decay indicating that these elements are definitely coming from selecting the wrong jet being selected. As well as the π radian flips from selecting the wrong jet, there are also additional off diagonal contributions seen which arise from poor reconstruction of the fat jets. This typically happens when the tops are not produced back to back due to ISR/BS. When this happens, during the fat jet reconstruction it is possible for contributions from both true fat jets to be mixed e.g instead of grouping the 3 jets from the hadronic jets together only two of them are grouped together and the third is grouped with the lone b jet from the leptonic top. When this mismatching happens the hadronic top is no longer fully reconstructed and so the angle measured for the top decay has little correlation with the generator value. Figure 5.14b shows that these remaining off diagonal elements disappear when a cut is placed on the separation of the tops at truth level.

In order to avoid the problems close to the beam line, multiple alternative jet asso-



(a) Cut placed on angle between reconstructed top and generator b jet from leptonic decay, $\Delta\text{Cos}\theta_{\text{Reco-Bjet}} > 0.1$

(b) Cut placed on collinearity between top pair at generator level, separation > 3 radians

Figure 5.14: Reconstructed vs generator top decay angles with truth level cuts to explain the off diagonal elements seen in 5.12.

ciation methods were devised- see Table 5.4 for detailed descriptions.

The relative effectiveness of these methods were evaluated in three ways shown in Figures 5.15, 5.16 and 5.17 respectively. The first method was to look at the overall distribution of $\cos\theta$ produced by each method compared to the distribution at generator level as this is what will be used to extract A_{fb}^t . All the methods agree well with the generator distribution in the central region of the detector but diverge in the high $|\cos\theta|$ region. This is mainly caused by the effects described above. Close to the beam line the jets aren't fully reconstructed, the jet association fails and the b jet from the leptonic side is selected rather than the hadronic top jet. This causes migrations from the forward region to the backward regions producing a deficit in the forward region and an excess in the backward region. Migrations do occur in the opposite direction too for the same reason, however because the top forward-backward asymmetry means that more tops are produced in the forward region to begin with, the net migration is from forward to backward. The migrations are not always a shift of π radians as one might expect. Instead the migrations occur from very close to the beam line to a broader range in the opposite direction. This is due to the fact that ISR/BS can mean the top pair aren't produced exactly back

Fat Jet Selection Method	Description
Lepton	The hadronically decaying top is deemed to be the fat jet with the greatest angular separation from the isolated lepton
B tag	The hadronically decaying top is deemed to be the fat jet with the greatest angular separation from the jet with the highest b tag (see 5.2.5 for details on how flavour tagging is performed)
Energy	Select the fat jet with the highest energy to be the hadronically decaying top
Multiplicity	Recluster both fat jets into N “micro jets” (see 5.2.3.3 for methodology) The hadronically decaying top should have a higher number of micro jets found within it
Mass	The hadronically decaying top is deemed to be the fat jet with the greatest mass
Top Mass	Select the fat jet whose mass is closest to the top mass as the hadronically decaying top
Democratic	A combination of the lepton, energy and mass methods. Each method votes for which fat jet it thinks is the hadronically decaying top. The fat jet with the most votes is then selected as the hadronically decaying top

Table 5.4: Methods used for identifying which fat jet corresponds to the hadronically decaying top.

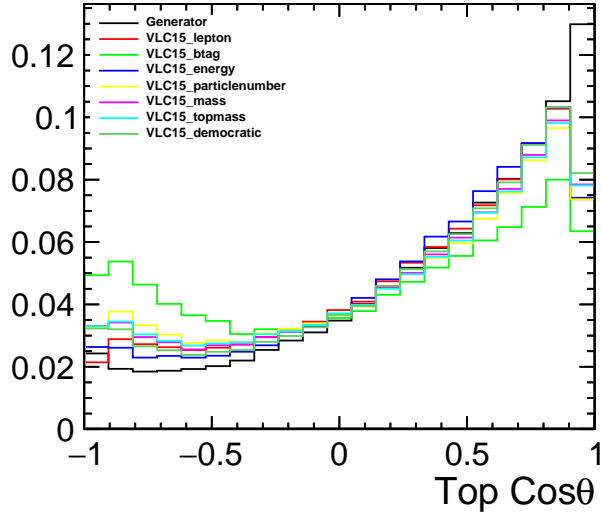


Figure 5.15: Reconstructed $\cos\theta$ distribution for various jet association methods. The expected distribution from truth level information is uncluded for reference.

to back in the lab frame and because the b-jet produced by the leptonic decay is not exactly collinear with the top decay axis. Comparing the methods we see that they all show similar levels of migration except for the btag method which shows the highest migration. This is attributed to the fact the highest btagged jet can sometimes be from the hadronic side even in events that are well reconstructed, and so the jet association will fail in more events than the other methods which only fail for events close to the beam line.

The second method was to measure the difference between the reconstructed and MC(generator) $\cos\theta$ per event and fit this with a gaussian. The variation in the width and mean of these distributions were plotted against the generator $\cos\theta$ and are shown in Figure 5.16. The effects of migration at high $\cos\theta$ is more pronounced in these plots where in the width we can see that the resolution on $\cos\theta$ gets much worse in the forward regions and the mean shows a pull in opposite directions in these regions proving the migrations do indeed occur in both directions with the same rate. Unfortunately there is little discrimination seen between the methods except for showing that there are slightly larger migrations when using the b-tag method.

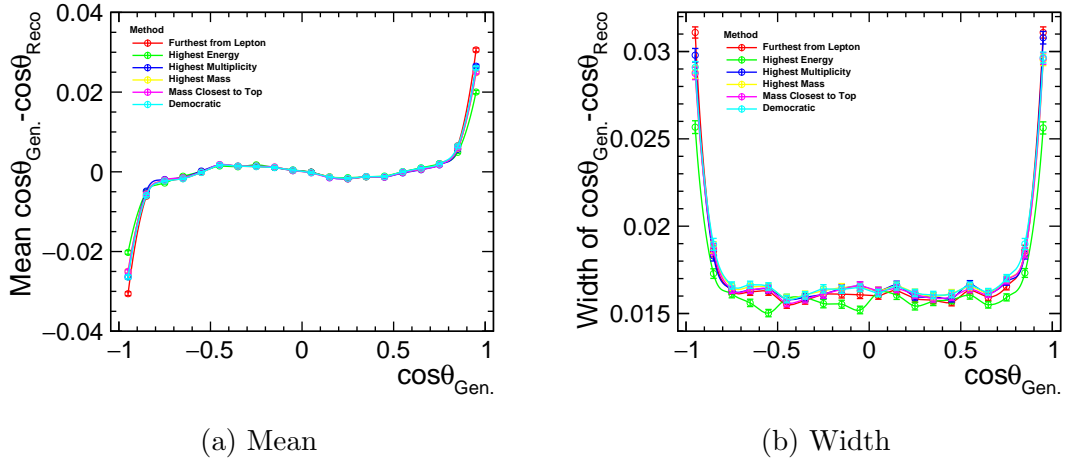


Figure 5.16: Mean and width from fitting $\Delta\cos\theta_{Gen.-Reco}$ to a gaussian. Mean: migrations close to $|\cos\theta| > 0.9$ result in a bias in the mean. The migrations cause a shift of roughly π radians resulting in the bias being in the opposite direction for each end of the range. Width: migrations close to $|\cos\theta| > 0.9$ cause a broadening in the resolution of the reconstructed $\cos\theta$.

The final method of comparison was to measure the efficiency with which the hadronic top was measured within the correct $\cos\theta$ bin as a function of the generator $\cos\theta$. For this study a bin width of 0.1 in $\cos\theta$ was used. The results are shown in Figure 5.17. Here there is a clearer separation in the performance of the different methods. B-tagging is seen to provide the worst efficiency while the energy and democratic methods provide the highest level of performance. The mass based selections provide slightly lower performance than the energy/democratic methods. This is likely explained by the fact they are less robust when the jets are not fully reconstructed. Missing a small section of the jet via acceptance losses/reconstruction inefficiencies can have a large impact on the reconstructed mass, however in the case of energy, if we naively assume that the energy is split evenly between the 6 final state particles, then we would expect that the energy of the hadronic fat jet would be three times that of the b-jet from the leptonic top and so considerable energy losses must occur before the wrong jet is selected. Due to their higher bin by bin efficiency, the energy and democratic methods are the best methods to use. Due to its simplicity the energy method is then chosen as the preferred method for the rest of the analysis.

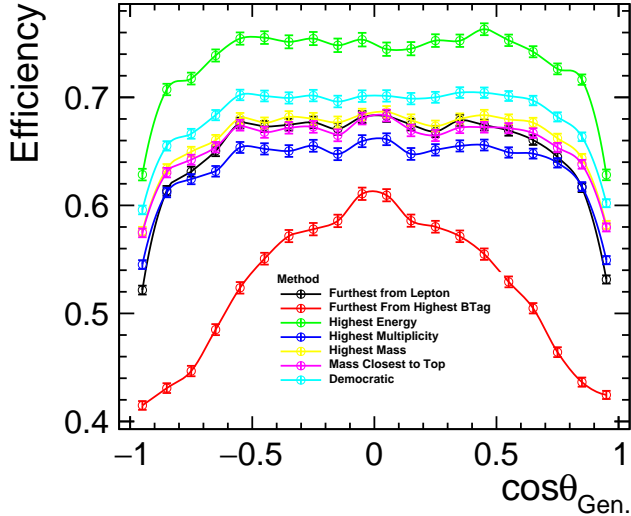


Figure 5.17: Efficiency for reconstructing the hadronically decaying top in the correct $\cos\theta$ bin.

5.2.3 Jet Substructure

After the fat jets have been found, in order to help distinguish signal events from similar background, it is useful to look at the substructure of these jets. To do this, three substructure variables were considered.

5.2.3.1 N-subjettiness

N-subjettiness is a substructure variable that is already being used in experiments at the LHC and is used to measure how many subjets are within a fat jet. In the signal channel one would expect the hadronic fat jet to contain three subjets (one b quark and two light quarks from the W decay) and the leptonic fat jet to have only one subjet. In order to calculate the N-subjettiness each fat jets is reclustered into N subjets. For this analysis this was done using the kt algorithm, R=0.3. After reclustering, the N-subjettiness is then defined as[57]:

$$\tau_N = \frac{1}{d_0} \sum_k p_{T,k} \min\{\Delta R_{j_1,k}, \Delta R_{j_2,k}, \dots, \Delta R_{j_N,k}\} \quad (5.4)$$

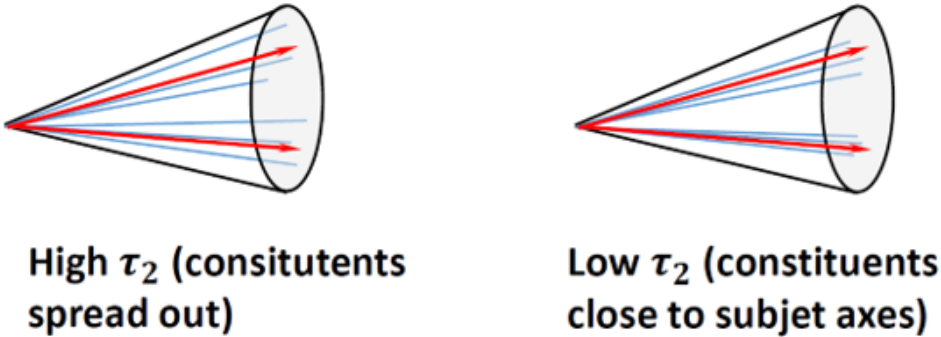


Figure 5.18: Diagrammatic representation of N-subjettiness.

Where k labels the constituent particles of the fat jet, j_i labels the subjets, ΔR is the distance in the rapidity-azimuth plane, p_T is transverse momentum and d_0 is a normalization parameter typically taken to be

$$d_0 = \sum_k p_{T,k} R_0 \quad (5.5)$$

Where R_0 is the jet radius used when reclustering the fat jet into the N subjets. One can see from Eq. 5.4 that the N -subjettiness is simply a sum of the angular separation of all particles in the fatjet to their nearest subjet axis weighted by the transverse of momentum of each particle. In the case that too few subjets have been chosen, the separation between the particles and the subjet axis will be large and so τ_N will be large. If instead the correct number of subjets are chosen, then all the particles are close to a subjet axis and τ_N will be closer to zero. This is perhaps more easily understood diagrammatically in Figure 5.18.

While the magnitude of τ_N does measure the substructure of the subjet, it is not possible to use it by itself to determine the correct number of subjets within a fatjet. This comes from the fact that while selecting too few subjets results in a higher value of τ , selecting too many jets actually results in a lower value of τ and so there is no minimum τ_N that decides the true number of subjets. As an example take the case shown on the right hand side of Figure 5.18. For two subjets, the value of τ_2 is clearly going to be quite small as the particles are all aligned along the two subjet

axes. However, if the fat jet was instead reclustered into three subjets, the most likely outcome would be that one of the two existing subjets would be artificially split into two new subjets. The two new subjet axis for the artificially split subjet would both be placed within the “true” subjet and so when calculating the angular separation of the particles in the true subjet to the new axis, the distance will be smaller than in the original case as there are now more axis to choose from. As a result τ_3 will be lower than τ_2 . This logic is true for any number of subjets and so it is almost always true that $\tau_N > \tau_{N+1}$. It is also not possible to simply place a cut on a specific τ_N as the absolute value of τ_N can depend on how diffuse the jets are. Again this is best seen from Figure 5.18. by inspection it is clear that the left hand event is a diffuse single subjet event while the right hand event is a two subjet event, however if one were to calculate τ_1 for both events the right hand event would have the lower τ_1 as the two subjets are relatively close to each other and so none of the particles would be particularly far from their combined central axis while in the single subjet event all of the particles are spread out and so the angular separation relative to a central axis would be larger.

In practice it turns out that the easiest way to get around these issues is to look at the ratio of τ_{N+1}/τ_N rather than just τ_N . This metric instead shows the improvement in τ_N from increasing the number of subjets. For a jet with 3 true subjets one expects a small value for τ_3/τ_2 and τ_2/τ_1 as the angular separations are being less limited by the lack of sufficient jet axes. For τ_4/τ_3 and above the value should be much closer to one because at this point any new jet axes will be the result of an artificial jet splitting and so the new axis will typically be very close to one of the old axes and so provides little improvement in the angular separation of the particles to their nearest axis.

An example of one of the N-subjettiness variables used here is the ratio τ_2/τ_1 for the leptonic fat jet (see Figure 5.19). For signal events where the expected number of subjets is one, the effect of adding an additional subjet axis is minimal and so the ratio is close to one. For many of the background e.g. $qqqq$, there will be two subjets within the fat jet and so the effect is more significant.

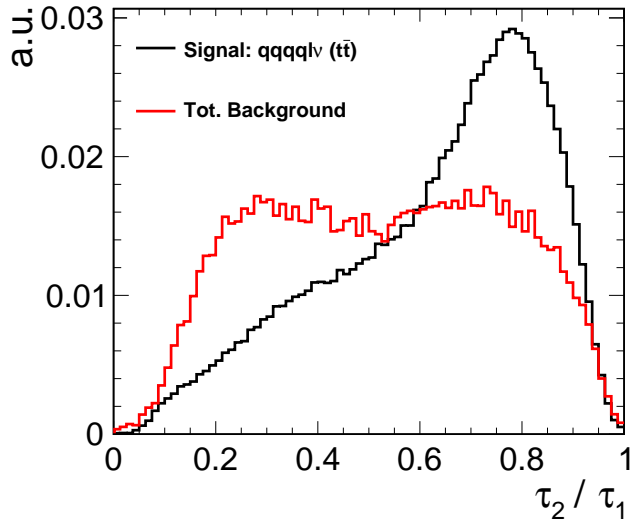


Figure 5.19: Leptonic fat jet τ_2/τ_1 . For signal events where the expected number of subjets is one, the effect of adding an additional subjet axis is minimal. For many of the background e.g. $qqqq$, there will be two subjets within the fat jet and so the effect is more significant.

5.2.3.2 Subjet Angular Distributions

As already described above, in the case that a fat jet is reclustered into more subjets than it should be, the subjets arising from the artificial splitting of a “true” subjet will typically be produced with minimal separation between them. This can be exploited to identify background events with a lower number of subjets than are present in the signal events. This is achieved by reclustering the hadronic fat jet into three subjets using the kt algorithm, $R=0.3$. The three resulting subjets are then ordered by energy and the angular separation between each of the them is determined. For background events the angle between these subjets is expected to be considerably smaller. The angular separation between the highest and lowest energy subjets is shown in Figure 5.20.

5.2.3.3 Jet Multiplicity

The final jet substructure variable that is considered is the jet multiplicity which corresponds to the number of particles within the fat jet. The number of parti-

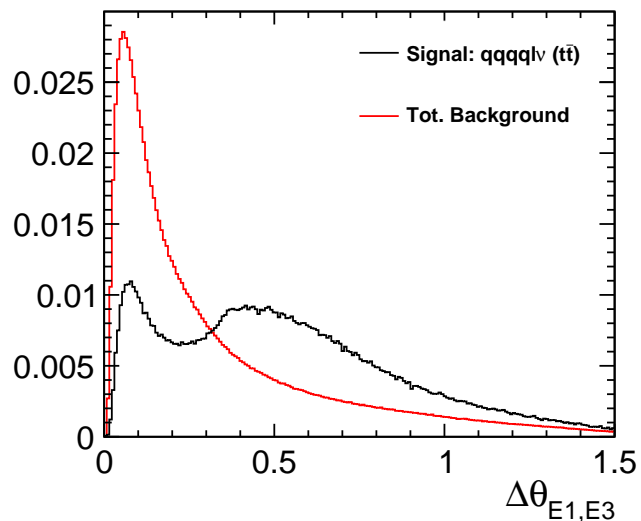


Figure 5.20: Angular separation of highest and lowest energy subjets

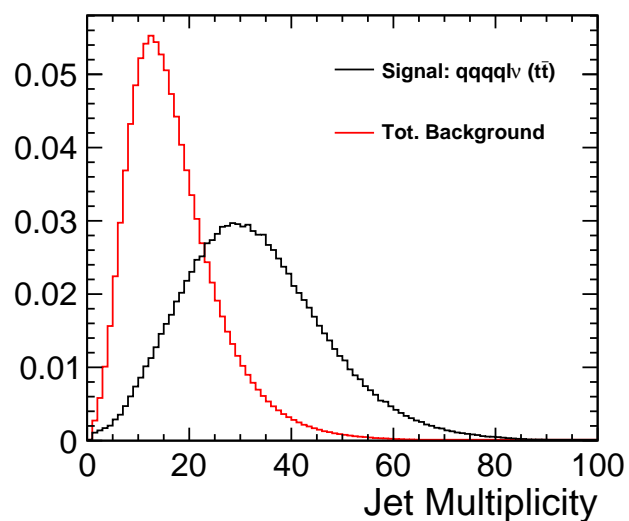


Figure 5.21: Jet multiplicity of the hadronic fat jet

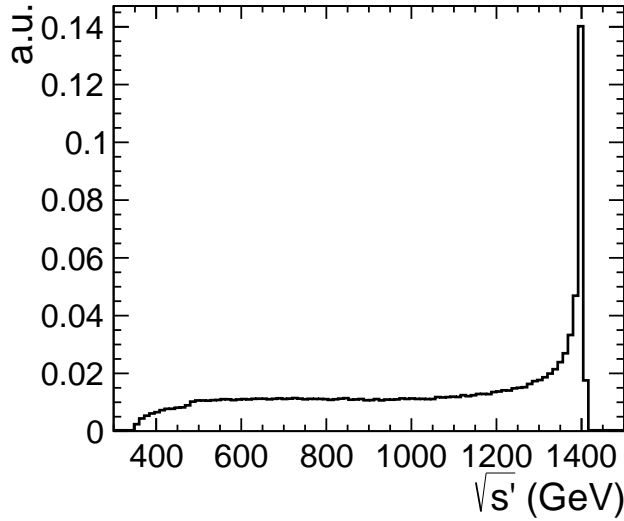


Figure 5.22: Expected $\sqrt{s'}$ spectrum for $t\bar{t}$ at 1.4 TeV

cles produced within a fat jet is proportional to the number of subjets within it. Originally the multiplicity was simply defined as being the number of Particle Flow Object (PFO)s assigned to the jet during the clustering process. However, to avoid sensitivity to how well the jet hadronization is modelled by PYTHIA, this was replaced by counting the number of “microjets” within a fat jet instead where the microjets are defined by reclustering the fat jet using the k_t algorithm in inclusive mode with a small radius $R=0.05$. This step is effectively reducing the resolution on the number of particle within the fat jet. Ideally one would try using multiple event generators to evaluate the sensitivity of the number of PFOs to the modelling, however as only one event generator is currently available within the linear collider framework this is not an option. To maintain a reduced sensitivity to the jet modelling these microjets are also used in place of PFOs for the N-subjettiness calculations when summing over all particles within a jet. The resulting jet multiplicity for the hadronic fat jet for signal and background events is shown in Figure 5.21

5.2.4 s' Reconstruction

Following the reconstruction of the lepton and hadronically decaying top it is already possible to calculate A_{FB}^t , however there is still benefit to first reconstructing the effective centre-of-mass energy of the events (along with the neutrino and any photons produced too.) This allows the calculation of A_{FB}^t to be determined in the $t\bar{t}$ rest frame where it is predicted to be up to 50% larger [58], and also allows a differential measurement of A_{FB}^t to be performed. The expected $\sqrt{s'}$ spectrum for $t\bar{t}$ production at 1.4 TeV is shown in Figure 5.22. Here it is seen that there is a large tail to the energy spectrum which can be taken advantage of to measure A_{FB}^t over a large range of energies. This differential measurement provides greater power for discriminating between different physics models than a single A_{FB}^t measurement. If $\sqrt{s'}$ can not be reconstructed per event, A_{FB}^t would have to either be measured as an integral over the full $\sqrt{s'}$ range or be measured just around the peak energy where there are only small $\sqrt{s'}$ corrections ($E > 1200$ GeV), however this would mean discarding $\sim 60\%$ of events produced during the 1.4 TeV run. As well as directly effecting the ways in which we can measure A_{FB}^t , reconstructing $\sqrt{s'}$ typically involves reconstructing the neutrino and photon contributions in the event. Having a description of these objects could provide further information by allowing the reconstruction of the leptonic top and so could help distinguish signal events from similar backgrounds.

In order to reconstruct $\sqrt{s'}$, multiple methods were attempted with varying complexity. In all cases, combined contributions from ISR and BS are approximated to the production of one photon radiated from the incoming electron positron pair.

5.2.4.1 Transverse/Longitudinal Association

The simplest method attempted was to assume that all missing momentum in the transverse direction is attributed to the neutrino, while all longitudinal missing momentum comes from photon contributions. These assumptions are motivated by the

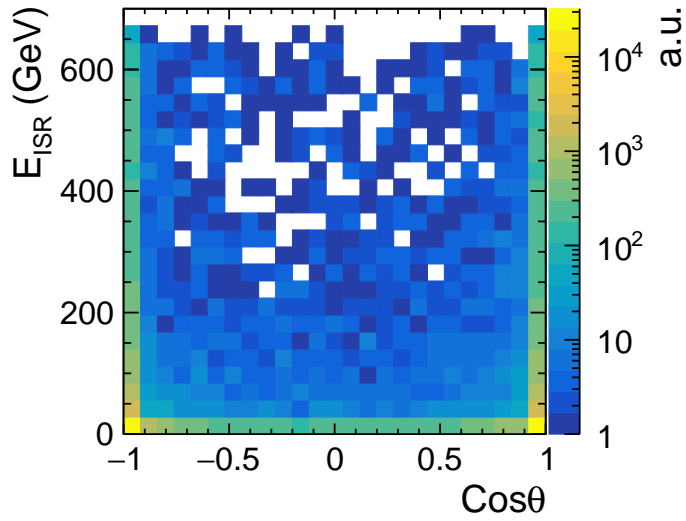


Figure 5.23: Angular energy distribution of initial state photons

results from Figure 5.23 which show that ISR photons are predominantly produced collinear to the beam. Using this method $\sqrt{s'}$ is then taken to be the mass of the neutrino + fat jets system. An event by event comparison of the reconstructed $\sqrt{s'}$ to the generator $\sqrt{s'}$ is shown in Figure 5.24. Overall this method is unsatisfactory as the reconstructed $\sqrt{s'}$ is consistently underestimating the true $\sqrt{s'}$ of the event. In retrospect this should be expected as the assumption that the photon losses are collinear to the beam is only approximately true. We have shown that it is true for high energy ISR photons, however one can see from Figure 5.23 that for lower energy emissions the photons can be emitted at large angles relative to the beam. This is why there is a stronger correlation between the reconstructed and generator $\sqrt{s'}$ when the photon energy losses are largest. On top of this there will also be photons produced through BS and there is no reason to assume these would be produced with negligible transverse momentum. In practice the neutrino from the leptonic top decay will also have a non negligible longitudinal momentum that should be accounted for. Overall it is clear that this method is unsatisfactory for reconstructing $\sqrt{s'}$.

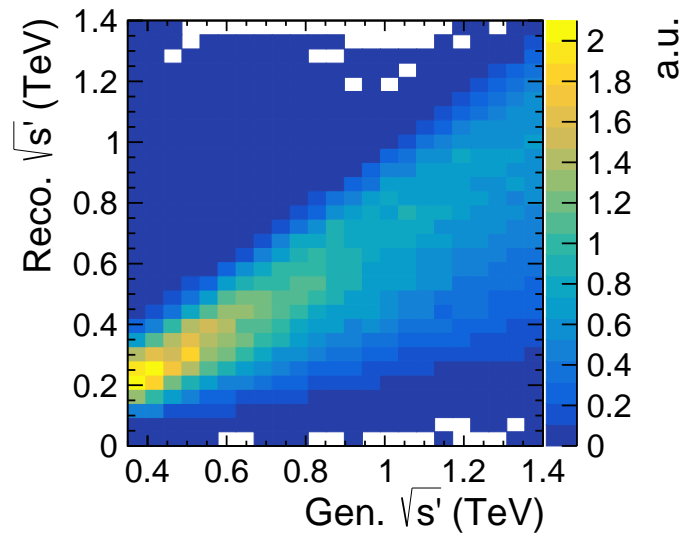


Figure 5.24: Reconstructed $\sqrt{s'}$ vs generator $\sqrt{s'}$ for transverse/longitudinal association method.

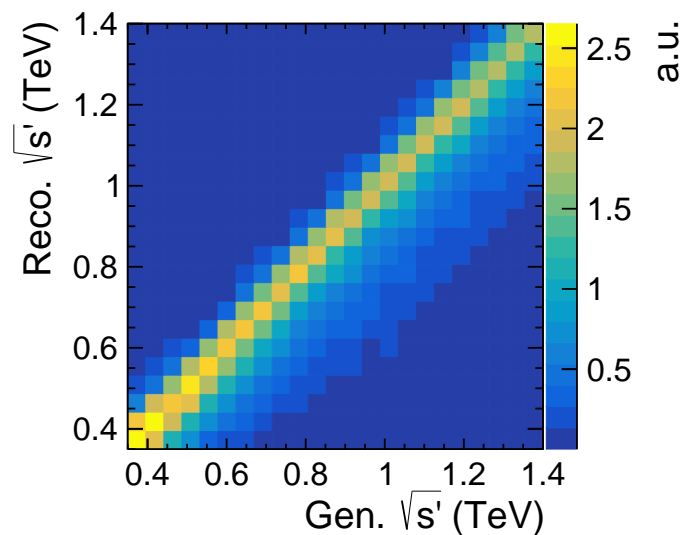


Figure 5.25: Reconstructed $\sqrt{s'}$ vs generator $\sqrt{s'}$ for mass constraint method.

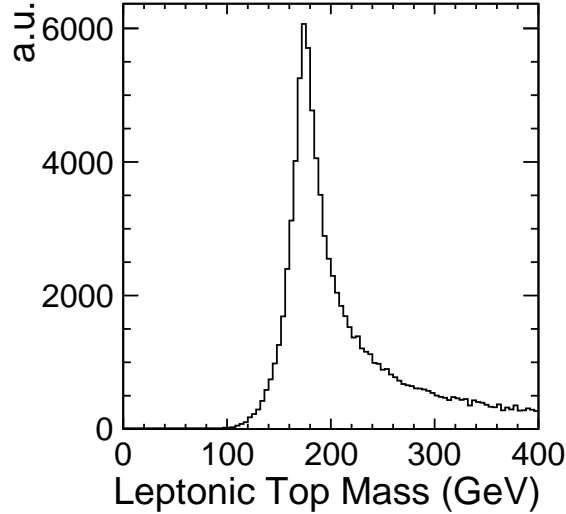


Figure 5.26: Mass of reconstructed top when using mass constraint method.

5.2.4.2 Analytic Mass Constraint

The second method attempted is an adaptation of the first method that makes use of the high efficiency with which the lepton is reconstructed to improve the performance. This method was developed by a fellow member of CLIC, Lars Rickard Ström, based at CERN when working on the alternative version of this analysis. It starts in the same manner by assuming that all transverse missing momentum comes from the neutrino, however the missing longitudinal momentum is then divided between the neutrino and photon. This is done by constraining the z component of the neutrino momentum by insisting the combination of the lepton and neutrino four momenta reproduces the W mass. Overall this acts to remove the incorrect assumption that the neutrino longitudinal momentum is negligible compared to the photons. The details of the calculations are as follows:

$$p_W = p_l + p_\nu \quad (5.6)$$

$$M_W^2 = M_l^2 + 2(E_l E_\nu - \mathbf{p}_l \cdot \mathbf{p}_\nu) \quad (5.7)$$

$$0 = -\frac{M_W^2 - M_l^2}{2} + E_l \cdot \sqrt{p_{\nu,x}^2 + p_{\nu,y}^2 + p_{\nu,z}^2} - (p_{\nu,x} p_{l,x} + p_{\nu,y} p_{l,y} + p_{\nu,z} p_{l,z}) \quad (5.8)$$

$$p_{\nu,z} = \frac{1}{2(p_{l,x}^2 - E_l^2)} (p_{l,z}(M_l^2 - M_W^2) - 2p_{l,z}(p_{l,x}p_{\nu,x} + p_{l,y}p_{\nu,y}) + X) \quad (5.9)$$

Where,

$$X = \sqrt{E_l^2((M_W^2 - M_l^2 + 2(p_{l,x}p_{\nu,x} + p_{l,y}p_{\nu,y}))^2 + 4\epsilon_T^2(p_{l,z}^2 - E_l^2))} \quad (5.10)$$

$$\epsilon_T = \sqrt{p_{\nu,x}^2 + p_{\nu,y}^2} \quad (5.11)$$

In the event that X is imaginary, ϵ_T is scaled so that X=0. The key detail however, is that there is that there are two possible solutions for the neutrino momentum arising from the quadratic form of Eq. 5.10. To decide the most suitable solution the W is combined with a fat jet (adding two more possible solutions, one for each fat jet) and the solution found to give an invariant mass closest to the top mass is chosen to be best. The resulting reconstructed leptonic top mass and $\sqrt{s'}$ reconstruction performance are shown in figures 5.25 and 5.26. The method does still have certain flaws that result in misreconstruction such as the assumption that all missing transverse momentum comes from the neutrinos and that the W mass is exactly 80.4 GeV with no associated width, however it clearly offers an improvement over the first method with a reasonable degree of agreement seen across the full $\sqrt{s'}$ range and a lower tendency to underestimate $\sqrt{s'}$.

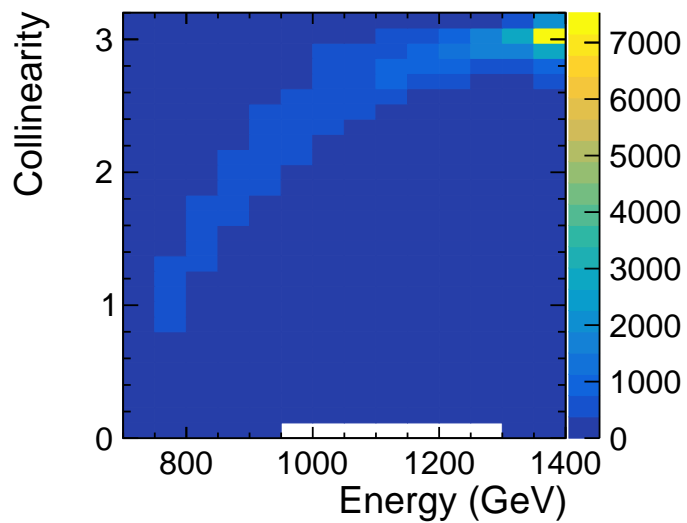
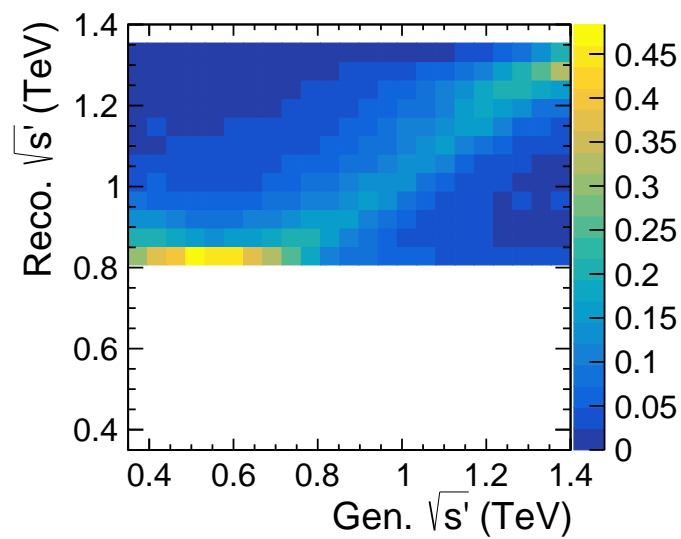
5.2.4.3 Collinearity

An alternative solution that was proposed was to use the collinearity (angular separation) of the $t\bar{t}$ pair as a way to measure $\sqrt{s'}$. For collisions occurring at the nominal collision energy, the total momentum of the collision should be zero and so the two

tops are produced back to back in the lab frame. If a photon is emitted before the electron positron collision occurs, the $t\bar{t}$ pair will have a none zero momentum and so will be boosted resulting in a reduced angular separation between the two tops. The scale of the boost (and thus the size of the angular separation) is proportional to the total momentum of the photon and so should be proportional to $\sqrt{s'}$. Extraction of $\sqrt{s'}$ is performed by first using one sample to determine the exact relationship between the collinearity and the generator $\sqrt{s'}$. This relationship is shown in Figure 5.27. A calibration curve is then generated by fitting the profile of this with a second order polynomial. The performance is then evaluated by taking a second event sample and using the calibration curve to map back from the collinearity to a reconstructed $\sqrt{s'}$. The resulting distribution for reconstructed $\sqrt{s'}$ vs generator $\sqrt{s'}$ is shown in Figure 5.28. Clearly this method is not as performant as the analytical method. One of the main reasons for this is that the collinearity should be measured between the two tops, however due to the neutrino not being reconstructed in the leptonic decay, one of the objects used for measuring the collinearity will be incomplete. This reduces the correlation between the collinearity and $\sqrt{s'}$. Further, as $\sqrt{s'}$ decreases and the tops become less well separated, the chance of reconstruction failures occurring increases. Namely, the jet finding approach used will start to mix parts of each top when trying to construct two fat jets and so the objects the collinearity is calculated for will no longer correspond to the generator level tops (see Section 5.2.2.1.) This explains the very poor performance for the lowest $\sqrt{s'}$ events.

5.2.4.4 Kinematic Fitting

The final approach considered was to use a kinematic fitter (MarlinKinFit v00-03[59]) to simultaneously fit the photon and neutrino four momenta. The fit has four free parameters- the neutrinos three momentum and the photons z momentum (it is still assumed that photons have negligible transverse momentum) and has six constraints- the total four momentum of the system, the mass of the leptonically W and that the masses of the two tops are consistent. It would be possible to replace

Figure 5.27: Collinearity of $t\bar{t}$ pairFigure 5.28: Reconstructed $\sqrt{s'}$ vs generator $\sqrt{s'}$ for collinearity method

the last constraint with a target mass for each top, however the current form has the benefit that it requires no prior knowledge of the mass of the top. The fit is passed five fit objects- the isolated lepton, two fat jets, neutrino and photon. It will then try and find a solution that satisfies all the fit constraints by varying the four momenta of the fit objects. In the case of the physically observable objects (the lepton and jets), the variation of the four momenta is limited according to the relevant detector resolutions:

$$\sigma_{EHad} = 35\% \sqrt{E} \quad (5.12)$$

$$\sigma_{EEM} = 20\% \sqrt{E} \quad (5.13)$$

$$\sigma_{\theta/\phi} = 10\% \quad (5.14)$$

The photon power spectrum is also set within the fit by setting the parameter b in the following formula:

$$\frac{dN}{dp_z} \propto \frac{1}{p_z^{1-b}} \quad (5.15)$$

A value of $b=0.5$ was found to give the best agreement for the reconstructed and generator $\sqrt{s'}$. The resulting performance is shown in Figure 5.29. Overall the performance is similar to that of the analytic method with a good agreement seen between the reconstructed and generator $\sqrt{s'}$ across the full $\sqrt{s'}$ spectrum. It was decided that this method shall be used for $\sqrt{s'}$ determination for the rest of the analysis. While the analytical method is as performant, it is potentially less robust than the kinematic fitting due to the fact it uses a fixed top mass and is unable to scale the four momenta of the measured particles to compensate for detector resolutions. For the rest of the analysis, the four momenta of all objects are taken to be those returned by the kinematic fit.

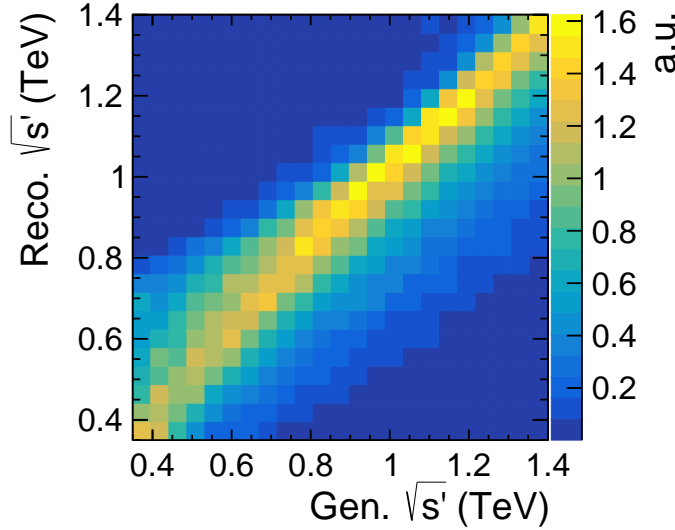


Figure 5.29: Reconstructed $\sqrt{s'}$ vs generator $\sqrt{s'}$ for kinematic fit method

5.2.5 Flavour Tagging

Flavour tagging was performed using LCFIPlus v00-05-02[49]. LCFIPlus makes use of three BDTs dedicated to searching for u/d/s (light), b and c quarks respectively, to provide a b-tag and c-tag indicating the probability of a jet containing a b or c quark. As the signal process contains two b jets, only the results of the b-tag are considered here. The BDTs were trained using 50,000 $ee \rightarrow Z\nu\nu, Z \rightarrow qq$ events each. The base performance of the BDTs was assessed using a further 150,000 $ee \rightarrow Z\nu\nu, Z \rightarrow qq$ events containing an even mixture of bb, cc and light quarks to measure the efficiency and purity that could be obtained. The results of this test (shown in Figure 5.30) indicate that in the case of $Z \rightarrow qq$ events high efficiencies and purities of $\sim 85\%$ can be achieved simultaneously. Before applying the flavour tagging to our analysis the events are first reclustered into four jets to try and capture the bjets separately from the light quark jets. This is done within the LCFIPlus package which uses the Durham algorithm by default. Ideally the BDTs would also be retrained using top events rather than Z, however due to limited sample sizes this was not a realistic option. The performance of the btagging for semileptonic top events was evaluated by comparing the highest and second highest b-tags assigned to any of the four jets in signal events to those in backgrounds. The results of this comparison are seen

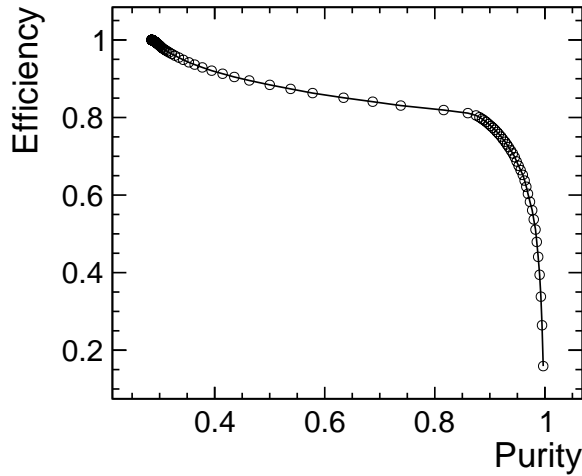


Figure 5.30: Purity vs efficiency for identifying b-jets, obtained from a sample of $Z \rightarrow \text{light}$, c and b quark events simulated at $\sqrt{s} = 1.4$ TeV

in Figure 5.31. It is clear that the btagging is consistently successful in finding the first b jet, but is less reliable for finding a second b jet. This is expected due to the topology of the event. The b jet produced by the leptonically decaying top should be well isolated from everything but the lepton which is identified and removed with high efficiency whereas the bjet from the hadronically decaying top will be close to two other jets meaning the jet finder is less likely to accurately associate the PFOs in that region to the correct initial quark. As a result the b jet from the leptonic side should be consistently reconstructed and tagged whereas the the b jet on the hadronic side will be less consistent as the efficiency for reconstructing the jet correctly is much lower. Despite the poorer performance of the second highest b-tag, both variables provide clear potential as discriminating variables for removing background.

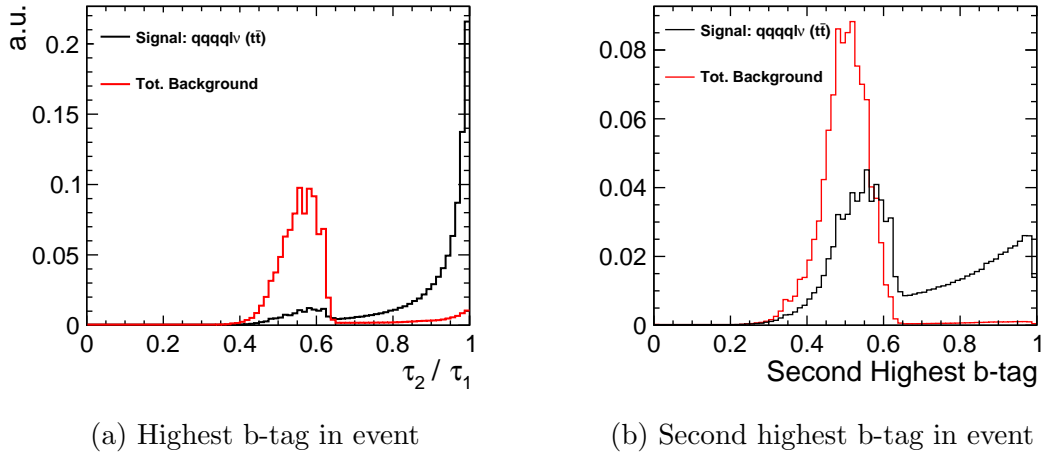


Figure 5.31: B-Tagging performance

5.3 Methods For Calculating A_{FB}^t

In it's simplest form, A_{FB}^t is defined as being:

$$A_{FB}^t = \frac{N_F - N_B}{N_F + N_B} \quad (5.16)$$

However for the purpose of measuring the asymmetry to the greatest precision possible, it can be better defined in terms of the differential top pair production cross section:

$$\frac{d\sigma}{d\cos\theta} \propto \frac{3}{8}(1 + \cos^2\theta)\sigma_U + \frac{3}{4}(1 - \cos^2\theta)\sigma_L + A_{FB}^t \cos\theta\sigma_{Tot} \quad (5.17)$$

where σ_U , σ_L and σ_{Tot} correspond to the unpolarised, longitudinally polarised and total cross section respectively and θ is the production angle of the top relative to the incoming electron[60]. This definition has three main benefits. Firstly it means A_{FB}^t can now be measured across several bins in theta. This inherently increases the precision to which it can be measured and reduces the sensitivity to boundary crossings between the forward and backward hemispheres that is present in the simpler definition. Secondly, A_{FB}^t is now sensitive to the shape of the $\cos\theta$

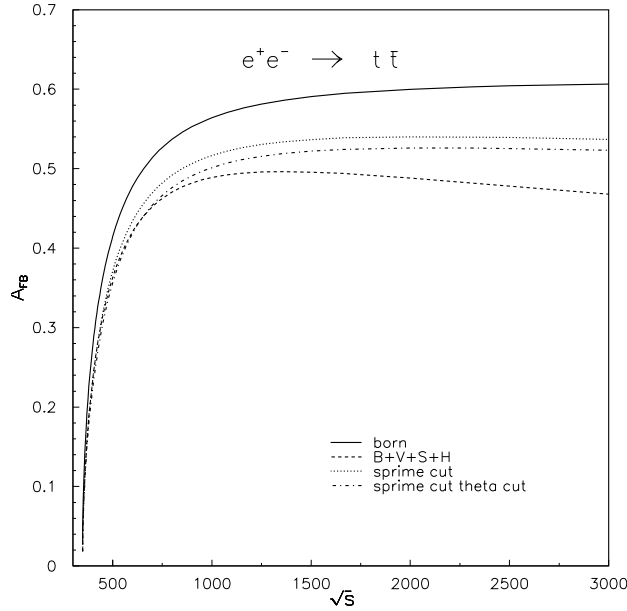


Figure 5.32: Predicted forward backward asymmetry as a function of collision energy[61].

distribution which means that it can be calculated for a reduced $\cos \theta$ range. This is important as we have already seen that the jet reconstruction is poor in the forward region and so it is desirable to exclude events in these regions. This is not possible to do with the simpler defintion because the asymmetry is actually largest in these forward regions (see Figure 5.33) and so placing an acceptance cut would introduce a large bias if just counting the total number of events in each hemisphere. Finally, using this fit approach it is also possible to simultaneously extract the total cross section for $t\bar{t}$ production which is equally useful in extracting the electroweak form factors of the $t\bar{t}X$ vertex.

As well as changing the method for extracting A_{FB}^t to increase the precision of the measurement, the information extracted can be further improved by binning the events in terms of the centre of mass of the collision. One can see from 5.32

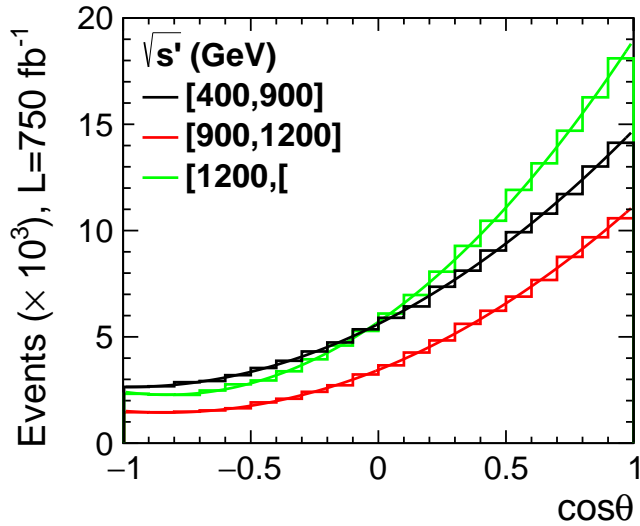


Figure 5.33: Generator level $\cos \theta$ distributions for each energy bin for -80% polarization with fit to Eq. 5.17

that A_{FB}^t varies greatly with energy. While the measurements performed during the 380 GeV and 3 TeV events will help characterise this shape, by making use of the long tail in the $\sqrt{s'}$ distribution at 1.4 TeV (see Section 5.2.4) it is possible to perform several measurements of A_{FB}^t in the central region across the turning point in the distribution which will help constrain any theory predicting a non SM A_{FB}^t . In particular the measurement will be performed in the ranges 400-900 GeV, 900-1200 GeV and >1200 GeV. The precision to which the cross section and A_{FB}^t can be extracted will decrease with energy due to the fact that the reconstruction techniques being applied are designed with the highest energy events in mind. In practice it is likely that a separate reconstruction technique will be developed for the lowest energy bin that will be based on resolving into four jets, however for now we present the precision achievable when using a single method across all three bins.

The expected $\cos \theta$ distributions at generator level are shown in Figure 5.33 along with their fits to Eq. 5.17 for the -80% electron polarization operation. The precision that can be expected using the fit and the simpler method for each energy assuming perfect event reconstruction is shown in Table 5.5. In all cases $\cos \theta$ is measured in the $t\bar{t}$ rest frame as this is where A_{FB}^t is maximal. To increase the number of

Energy (GeV)	σ (fb)	A_{FB}^t	ΔA_{FB}^t (Counting)	ΔA_{FB}^t (Fit)
$>=1200$	18.4	0.563	0.007	0.006
900-1200	11.0	0.547	0.009	0.008
400-900	16.6	0.457	0.008	0.007

Table 5.5: Precision attainable on A_{FB}^t during the -80% electron polarization stage assuming perfect event reconstruction for the simple counting method vs the fit method for extraction

available signal events, the angle is multiplied by the charge of the lepton so that events in which it is the antitop that decays hadronically the angle of the top can still be recovered. Note that this is only possible when measuring A_{FB}^t in the $t\bar{t}$ rest frame where the top and antitop are produced back to back.

5.4 Event Selection

Event selection is performed in three distinct stages- preselection, quality cuts and BDT selection, with each stage having it's own purpose. The preselection is designed to remove easily identifiable backgrounds with minimal reduction in the signal efficiency. Quality cuts are then applied to remove events in which the event reconstruction has failed such as when the fat jets have been incorrectly associated to the hadronically decaying top or lone b jet. The final selection is then performed using a pair of BDTs for each polarization that are trained to identify low and high energy signal events and reject any remaining backgrounds. The preselection cuts, quality cuts and choice of variables used by the BDTs were all optimised for the -80% electron polarization state integrated across the full energy range. As such there is likely still some improvement that could be made by individually reoptimising the cuts and variables used for each energy bin and each polarization state but this is not examined in this version of the analysis.

5.4.1 Preselection

The preselection cuts were designed to remove easily identifiable backgrounds without a significant reduction in the signal yield. The cuts used were as follows:

- One charged isolated lepton found
- Visible transverse momentum $> 200 \text{ GeV}$
- Energy of the hadronically decaying top $> 100 \text{ GeV}$
- Transverse momentum of the lone b jet $> 20 \text{ GeV}$
- Negative natural log of the jet resolution parameter at the transition from 2 to 3 jets, $-\ln y_{23}, < 7$
- $-\ln y_{34} < 9$
- $|\cos \theta|$ of the reconstructed top in the lab frame < 0.9

The resulting efficiency for the signal and background processes are shown in Tables 5.6 and 5.7. Clearly there is minimal loss of signal events while certain backgrounds can be suppressed to $\mathcal{O}(10^2)$.

5.4.2 Quality Cuts

The quality cuts were designed to remove events in which the reconstruction has failed to reconstruct the top or has assigned the wrong fat jet to be the hadronic top. Doing this helps reduce the migration effects discussed in Section 5.2.2.1 which result in a poor correlation between the reconstructed and generator $\cos \theta$ distributions. As such the cuts were optimised to reject events in which $|\cos \theta_{\text{Reco-Gen}}| > 0.05$. The best cuts found were as follows:

- Reconstructed hadronically decaying top mass $> 100 \text{ GeV}$

Process	Cross Section(fb)	Efficiency
$e^+e^- \rightarrow t\bar{t} \rightarrow qqqql\nu(l = e, \mu)$	46.8	9.67E-1
$e^+e^- \rightarrow t\bar{t} \rightarrow qqqql\nu(l = \tau)$	23.2	8.08E-1
$e^+e^- \rightarrow t\bar{t} \rightarrow qqqql\nu(\text{non } t\bar{t})$	72.3	8.22E-1
$e^+e^- \rightarrow qqqqqq$	116.4	7.56E-1
$e^+e^- \rightarrow qql\nu l\nu$	44.1	7.55E-1
$e^+e^- \rightarrow qqqq$	2304.0	2.75E-1
$e^+e^- \rightarrow qql\nu$	6975.0	1.69E-1
$e^+e^- \rightarrow qql l l$	2681.0	6.45E-2
$e^+e^- \rightarrow qq\nu\nu$	1395.0	6.85E-2
$e^+e^- \rightarrow qq$	4843.0	8.61E-2

Table 5.6: Efficiency for signal and background processes following pre-selection cuts for -80% polarization

Process	Cross Section(fb)	Efficiency
$e^+e^- \rightarrow t\bar{t} \rightarrow qqqql\nu(l = e, \mu)$	24.7	9.71E-1
$e^+e^- \rightarrow t\bar{t} \rightarrow qqqql\nu(l = \tau)$	12.3	8.15E-1
$e^+e^- \rightarrow t\bar{t} \rightarrow qqqql\nu(\text{non } t\bar{t})$	16.5	8.07E-1
$e^+e^- \rightarrow qqqqqq$	44.9	7.54E-1
$e^+e^- \rightarrow qql\nu l\nu$	15.3	7.87E-1
$e^+e^- \rightarrow qqqq$	347	3.07E-1
$e^+e^- \rightarrow qql\nu$	1640	1.17E-1
$e^+e^- \rightarrow qql l l$	2530	5.21E-2
$e^+e^- \rightarrow qq\nu\nu$	180	7.30E-2
$e^+e^- \rightarrow qq$	3170	6.03E-2

Table 5.7: Efficiency for signal and background processes following pre-selection cuts for +80% polarization

- Mass of the b jet from the leptonically decaying top < 100 GeV
- Pt of the hadronically decaying top > 100 GeV
- $0.2 < \cos \theta_{12} < 0.9$
- $y_{23} < 3$
- $| \text{Total } P_z | < 100$ GeV

Where θ_{12} is the angle between the two highest energy subjets of the three subjets in the hadronic fat jet. For reasons discussed later in Section 5.6 relating to minimising biases, an additional cut on the momentum of the isolated lepton > 70 GeV is also included for the lowest energy bin. As already noted, some improvement in the performance could be achieved by separately optimising the cuts for each energy bin and polarization. This is particularly true for variables such as $\cos \theta_{12}$ which are not lorentz invariant and so will remove more signal events in the lower energy bins than the higher ones, however no lorentz invariant equivalents to these cuts were found to provide as reliable discrimination against poorly reconstructed events. That being said, the efficiency is expected to be lower for the lower energy bins regardless as the jet reconstruction has already been shown to be less reliable for lower $\sqrt{s'}$ events and so the jets are less likely to have the correct kinematic properties of the generator level tops. I.e. the ratio $\frac{|\cos \theta_{\text{Reco-Gen}}| > X}{|\cos \theta_{\text{Reco-Gen}}| < X}$ will always be higher in the lower energy bins. Again this motivates an additional future study dedicated to reconstructing events in the lowest energy bin.

The resulting efficiency for the signal and background processes are shown in Tables 5.8 and 5.9.

This step is where the largest loss in signal efficiency occurs during the selection process. While this is undesirable, one can see from Figure 5.34 that the quality selection does provide a vast improvement in the agreement between the reconstructed and generator level $\cos \theta$ distributions. This is desirable as it reduces the chance of

Process	Cross Section(fb)	Efficiency
$e^+e^- \rightarrow t\bar{t} \rightarrow qqqql\nu(l = e, \mu)$		
E>=1200 GeV	18.4	3.67E-1
900<=E<1200 GeV	11.0	3.33E-1
400<=E<900 GeV	16.6	4.00E-2
$e^+e^- \rightarrow t\bar{t} \rightarrow qqqql\nu(l = \tau)$	23.2	2.52E-1
$e^+e^- \rightarrow t\bar{t} \rightarrow qqqql\nu(\text{non } t\bar{t})$	72.3	9.82E-2
$e^+e^- \rightarrow qqqqqq$	116.4	5.86E-2
$e^+e^- \rightarrow qql\nu l\nu$	44.1	5.25E-2
$e^+e^- \rightarrow qqqq$	2304.0	1.07E-2
$e^+e^- \rightarrow qql\nu$	6975.0	1.08E-3
$e^+e^- \rightarrow qql l$	2681.0	8.32E-4
$e^+e^- \rightarrow qq\nu\nu$	1395.0	1.77E-4
$e^+e^- \rightarrow qq$	4843.0	6.93E-3

Table 5.8: Efficiency for signal and background processes following pre-selection and quality cuts for -80% polarization.

Process	Cross Section(fb)	Efficiency
$e^+e^- \rightarrow t\bar{t} \rightarrow qqqql\nu(l = e, \mu)$		
E>=1200 GeV	9.84	3.45E-1
900<=E<1200 GeV	5.79	3.02E-1
400<=E<900 GeV	8.7	5.00E-2
$e^+e^- \rightarrow t\bar{t} \rightarrow qqqql\nu(l = \tau)$	12.3	2.52E-1
$e^+e^- \rightarrow t\bar{t} \rightarrow qqqql\nu(\text{non } t\bar{t})$	16.5	1.48E-1
$e^+e^- \rightarrow qqqqqq$	44.9	6.01E-2
$e^+e^- \rightarrow qql\nu l\nu$	15.3	8.77E-2
$e^+e^- \rightarrow qqqq$	347	1.64E-2
$e^+e^- \rightarrow qql\nu$	1640	5.87E-4
$e^+e^- \rightarrow qql l$	2530	6.15E-4
$e^+e^- \rightarrow qq\nu\nu$	180	3.01E-4
$e^+e^- \rightarrow qq$	3170	4.80E-3

Table 5.9: Efficiency for signal and background processes following pre-selection and quality cuts for +80% polarization.

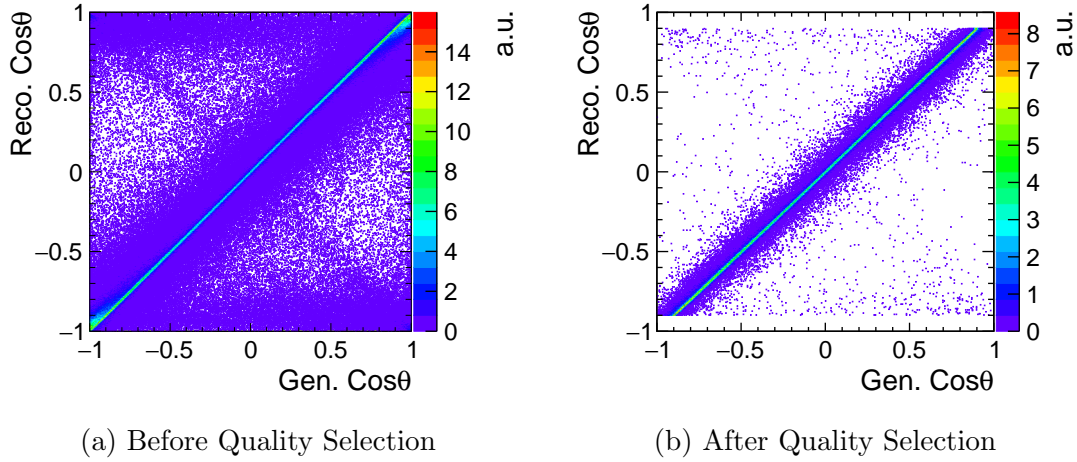


Figure 5.34: Effect of quality selection on agreement of $\cos \theta$ reco. vs gen.

a bias being introduced in A_{FB}^t from the misreconstruction of events. A discussion of possible remaining biases from this is presented in Section 5.6.

5.4.3 BDT Selection

The final stage of selection uses a multivariate approach to remove any remaining backgrounds. Two BDTs were trained for each polarization state where one is trained on events with a generator $\sqrt{s'} \geq 1.2$ TeV and the other is trained on events with $\sqrt{s'} < 1.2$ TeV. The selection itself is performed by placing a cut on the score from each BDT and selecting events which pass either cut in each energy bin. The choice of cut on each score is optimised for each energy bin in order to maximise the statistical significance, $S/\sqrt{S+B}$. This helps to improve the performance due to the fact the signal topology is quite different in the two energy regions due to the different boost factors. If only one BDT was used it would have to simultaneously identify events with both topologies making it harder to identify background events. With two BDTs, the high energy BDT is more capable of rejecting backgrounds with a topology similar to the low energy signal and vice versa. To further improve the BDT performance, only 6 fermion, qq and qqlv final states were included in the training as these are the most challenging to remove. Negligible amounts of other event were found to pass the BDT despite not being specifically trained against.

In all cases the BDT is trained on the 21 variables listed below. The mass of the reconstructed top is deliberately not included to prevent a possible bias towards the generator top mass. For each BDT, the relevant samples are split evenly between training and testing. In order to make optimal use of the limited samples available, for each BDT, an additional BDT is trained in which the samples are reversed so that all events can be used for training and for testing. Care is taken to ensure that no event trains and is tested by the same BDT.

- Total visible energy and transverse momentum
- Centre of mass of the event
- Energy and transverse momentum of hadronic fat jet
- Mass, τ_1 and τ_2/τ_1 of leptonic fat jet
- Relative angles of the three subjets within the hadronic fat jet
- Energy, transverse momentum and total momentum of the isolated lepton
- Number of lepton candidates with energy > 30 GeV
- Angular separation of the lepton and hadronic fat jet
- $-\ln(y_{23})$
- Major thrust of the event
- Energy of the leptonically decaying top
- Highest and next to highest btags

The resulting distributions of the BDT scores for each classifier are shown in Figure 5.35. A high degree of separation is seen in all cases, though it is more pronounced in the higher energy classifiers. The efficiencies and expected number of events after 750 fb^{-1} are shown for the high energy bins only in Tables 5.10 and 5.11. The equivalent results for the lower energy bins can be found in Appendix .2 along

with the distributions for each of the variables used for training the BDT. Overall it can be seen that a good signal to background ratio is achieved for a moderate signal efficiency in the higher energy bins. The background is dominated by 6 fermion final states, predominantly from $t\bar{t}$ and single top events as expected. Further improvements might be made if tau tagging was possible, however as already discussed in the previous chapter, an adequately performant tau finder has yet to be developed for CLIC.

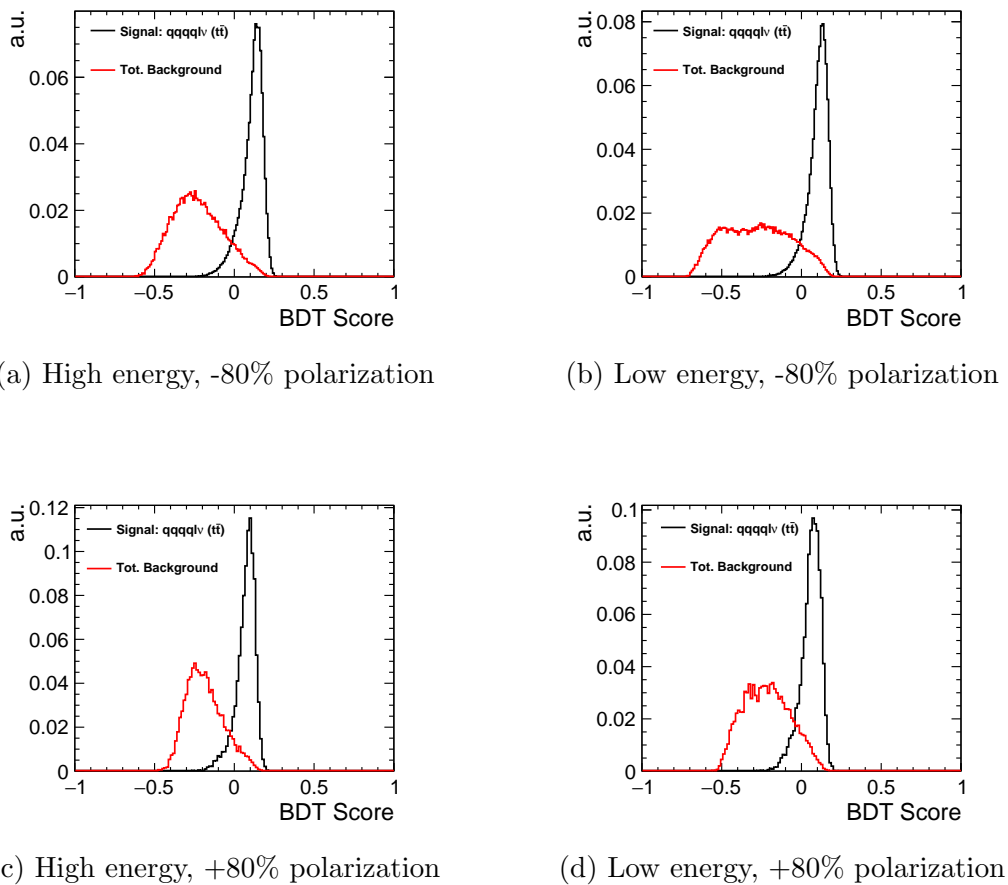


Figure 5.35: BDT performance for all four classifiers

5.5 Extraction of A_{FB}^t and cross section

As discussed earlier, the measurement of the cross section and A_{FB}^t can be performed simultaneously by fitting to Eq. 5.17. However before this can be done, corrections

Process	Cross Section (fb)	Efficiency Pre. & Quality	Efficiency BDT	N Expected
$e^+e^- \rightarrow t\bar{t} \rightarrow qqqql\nu(l = e, \mu)$				
E>=1200 GeV	18.4	3.67E-1	3.15E-1	4350
E<1200 GeV	28.4	3.11E-2	2.59E-2	550
$e^+e^- \rightarrow t\bar{t} \rightarrow qqqql\nu(l = \tau)$	23.2	1.20E-1	3.67E-2	640
$e^+e^- \rightarrow t\bar{t} \rightarrow qqqql\nu(\text{non } t\bar{t})$	72.3	4.80E-2	2.27E-2	1230
$e^+e^- \rightarrow qqqqqq$	116.4	2.23E-2	1.17E-3	100
$e^+e^- \rightarrow qql\nu l\nu$	44.1	1.48E-2	8.38E-3	280
$e^+e^- \rightarrow qqqq$	2304.0	4.45E-3	4.72E-5	80
$e^+e^- \rightarrow qql\nu$	6975.0	4.75E-4	1.04E-5	50
$e^+e^- \rightarrow qll$	2681.0	3.10E-4	1.19E-5	20
$e^+e^- \rightarrow qq\nu\nu$	1395.0	6.37E-5	<E-6	0
$e^+e^- \rightarrow qq$	4843.0	2.97E-3	4.83E-5	180
TotalBackground	18500	2.12E-3	2.26E-4	3140

Table 5.10: Efficiency for signal and background processes being classified as E > 1200 GeV following all stages of selection, and the expected number of events for 750 fb^{-1} for -80% polarization

Process	Cross Section (fb)	Efficiency Pre. & Quality	Efficiency BDT	N Expected
$e^+e^- \rightarrow t\bar{t} \rightarrow qqqql\nu(l = e, \mu)$				
E>=1200 GeV	9.84	3.45E-1	3.04E-1	2240
E<1200 GeV	14.9	3.26E-2	2.81E-2	310
$e^+e^- \rightarrow t\bar{t} \rightarrow qqqql\nu(l = \tau)$	12.3	1.25E-1	3.40E-2	310
$e^+e^- \rightarrow t\bar{t} \rightarrow qqqql\nu(\text{non } t\bar{t})$	16.5	7.07E-2	4.47E-2	550
$e^+e^- \rightarrow qqqqqq$	44.9	2.17E-2	1.27E-3	40
$e^+e^- \rightarrow qql\nu l\nu$	15.3	2.44E-2	1.59E-2	180
$e^+e^- \rightarrow qqqq$	347.0	7.13E-3	1.45E-4	40
$e^+e^- \rightarrow qql\nu$	1644.0	2.56E-4	1.59E-5	20
$e^+e^- \rightarrow qql l$	2529.0	2.13E-4	1.38E-5	30
$e^+e^- \rightarrow qq\nu\nu$	180.0	1.16E-4	<E-6	0
$e^+e^- \rightarrow qq$	3169.0	2.05E-3	5.45E-5	130
TotalBackground	7970	1.82E-3	2.71E-4	1620

Table 5.11: Efficiency for signal and background processes being classified as E > 1200 GeV following all stages of selection and the expected number of events for 750 fb⁻¹ for +80% polarization

must be made to account for remaining backgrounds and finite efficiencies. In both cases it is assumed that there is no statistical uncertainty introduced in these corrections as the statistical uncertainty can be made arbitrarily small by generating a sufficiently large event sample. Background subtraction was done assuming perfect background subtraction in each bin. The uncertainty on the background is instead accounted for later as a systematic effect. After the background has been subtracted, bin by bin efficiency corrections are applied to scale back to the generator distribution. By definition this means that the final distribution the fit is performed on will have the same content per bin as the generator distribution with only the uncertainty on each bin changing. Due to the large statistical sample available for the signal process, the efficiency corrections can be calculated by splitting the signal sample in two, evaluating the efficiency per bin in each sample and scaling by these efficiencies in the alternative sample.

Following these corrections the fit can finally be applied. Due to the fact a cut of $|\cos \theta| < 0.9$ is applied in the lab frame, the fit is only performed in this same range in the $t\bar{t}$ rest frame as there are a statistically insignificant number of events outside this range. The resulting fits, along with the $\cos \theta$ distribution before the corrections are applied are shown in Figure 5.36. The values for A_{FB}^t and the total cross section along with their uncertainties are extracted from the fit, where the correlated errors between parameters σ_u and σ_L are taken into account when determining the total cross section uncertainty. These values along with the generator values for A_{FB}^t and σ_{Total} are shown for each energy and beam polarization in Table 5.12.

Overall it is seen that the typical uncertainties achieved are at the few per cent level. Already this is an order of magnitude better than the precision seen at the LHC, $\mathcal{O}(30\%)[62]$, which is limited by the inability to distinguish tops produced via quark-quark interactions from those produced by gluon interactions. A factor of $\sim \sqrt{2}$ is seen between the equivalent results for each polarization, consistent with the factor of 2 difference in the $t\bar{t}$ cross section for each polarization. This indicates the reconstruction and event selection method is equally effective for both polarizations. The precision is seen to get worse for the lower energy bins. This is to be expected

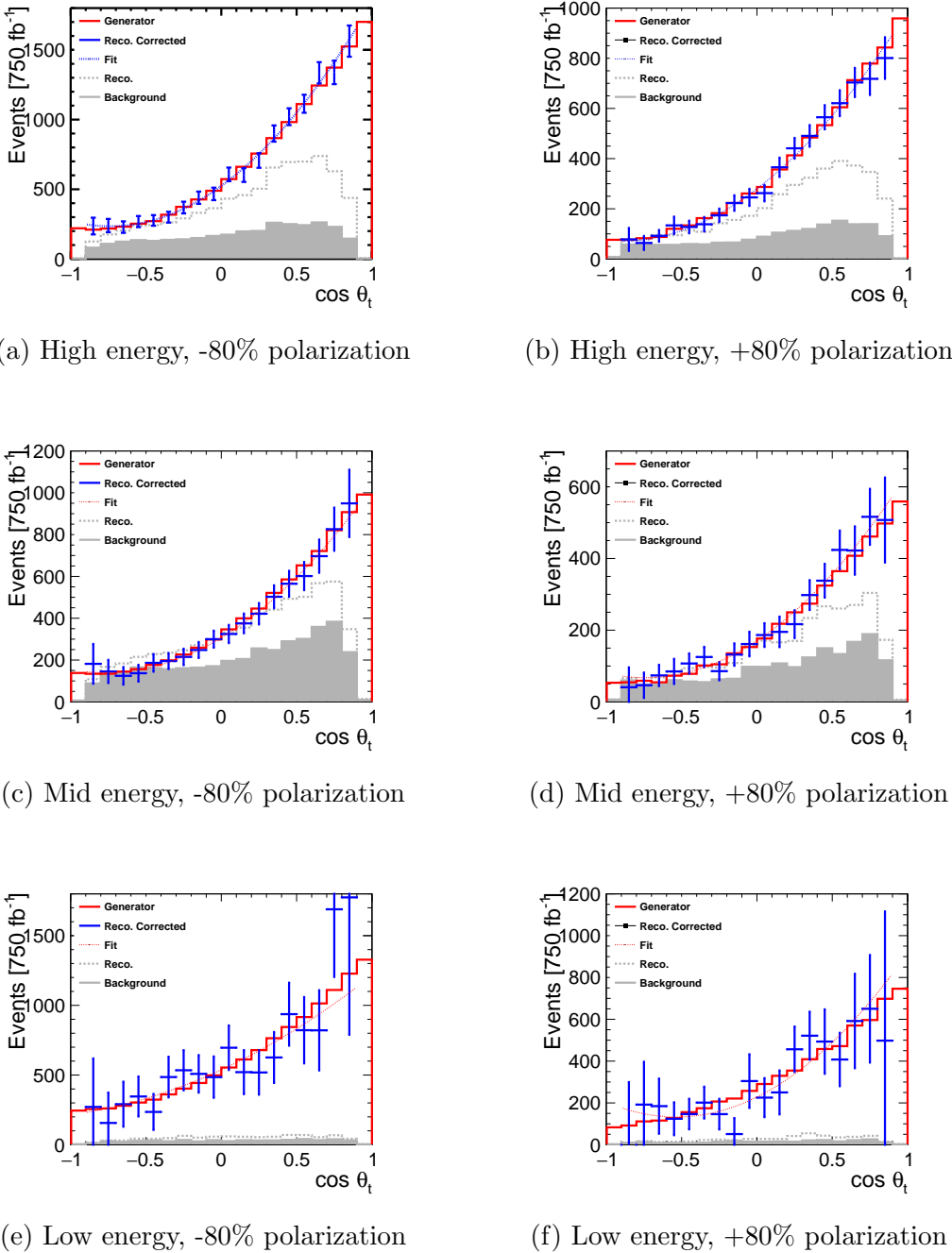


Figure 5.36: Angular distributions for all energy and polarization bins at generator, reconstructed and corrected levels along with the final fits from which A_{FB}^t and σ_{Total} are extracted. In all cases a luminosity of 750 fb^{-1} is assumed for each beam polarization.

Energy (GeV)	A_{FB}^t (Gen.)	A_{FB}^t (Reco.)	ΔA_{FB}^t	σ (Gen)(fb)	σ (Reco)(fb)	$\Delta\sigma$ fb)
$P(e^-)=-80\%$						
$>=1200$	0.563	0.563	0.018	18.4	18.4	0.37
900-1200	0.547	0.546	0.034	11.0	11.0	0.38
400-900	0.457	0.458	0.081	16.6	16.6	1.31
$P(e^-)=+80\%$						
$>=1200$	0.621	0.621	0.024	9.8	9.8	0.28
900-1200	0.605	0.589	0.045	5.8	5.9	0.29
400-900	0.525	0.514	0.105	8.7	8.6	0.83

Table 5.12: Values and statistical uncertainties for A_{FB}^t and cross section as extracted from performing a fit to $\cos\theta$ for each energy and polarization.

given that the reconstruction was designed with the focus of reconstructing events in which the top decay products are highly boosted. In the case of lower energy events the reconstruction is known to fail with neither fat jet corresponding to the complete decays products of the hadronic top. As a result these events typically fail the quality cuts leading to a low signal efficiency and so a large statistical uncertainty is introduced from performing large efficiency corrections before the final fit.

It should be noted that these results are consistent with those seen for the alternative version of this analysis performed by Lars Rickard Ström [2]. In this version of the analysis the lepton finding, top reconstruction, $\sqrt{s'}$ determination and event selection are all done in a completely different way to what is presented here, however the methods used for extracting the cross section and A_{FB}^t and the treatment of uncertainties are identical for both analyses. The expected precision for the cross section and A_{FB}^t in this alternative version of the analysis are shown in Table 5.13. The results from both analyses are seen to be consistent when accounting for the fact this version of the analysis has a slightly lower signal efficiency than the version described in this thesis.

Energy (GeV)	A_{FB}^t (Gen.)	A_{FB}^t (Reco.)	ΔA_{FB}^t	σ (Gen)(fb)	σ (Reco)(fb)	$\Delta\sigma$ fb)
$P(e^-)=-80\%$						
$>=1200$	0.563	0.561	0.021	18.4	18.4	0.5
$P(e^-)=+80\%$						
$>=1200$	0.621	0.618	0.023	9.8	9.9	0.31

Table 5.13: Values and statistical uncertainties for A_{FB}^t and cross section as extracted from the alternative version of the analysis performed by Lars Rickard Ström.

5.6 Systematics

On top of the statistical uncertainty there are several additional sources of uncertainty that arise from systematic effects. A description of each effect considered is given below.

5.6.1 Background Normalization

Following the event selection stage it was assumed that any remaining backgrounds could be removed without introducing an additional statistical uncertainty as this can be made arbitrarily small with a large enough sample size. While this is true, there will still be a theoretical uncertainty on the background cross sections which cannot be avoided. Here we assumed a conservative value of 5% on the dominant backgrounds ($qqqql\nu, qql\nu l\nu, qq$) While we assumed a lower value of 1% during our treatment of the Higgs analysis, it was deemed necessary to increase this value here as for backgrounds such as qq to resemble a six fermion final state requires the event to be in the tails of the kinematic distributions which are typically less well modelled. Assuming this value of 5% for the theoretical uncertainty on each background, the analysis was repeated twice for each dominant background, once where the background is scaled to be 5% greater than what is assumed in the subtraction step, once where it is 5% lower. The presence of the excess background (deficit in signal events) will have a significant impact on the fit results, particularly

Energy (GeV)	A_{FB}^t	ΔA_{FB}^t (Stat.)	ΔA_{FB}^t (Syst.)	σ (fb)	$\Delta\sigma$ (Stat.)(fb)	$\Delta\sigma$ (Syst.)(fb)
$P(e^-)=-80\%$						
$>=1200$	0.563	0.018	0.003	18.4	0.37	0.27
900-1200	0.546	0.034	0.006	11.0	0.38	0.28
400-900	0.458	0.081	0.006	16.6	1.31	0.46
$P(e^-)=+80\%$						
$>=1200$	0.621	0.024	0.003	9.8	0.28	0.13
900-1200	0.589	0.045	0.003	5.9	0.29	0.13
400-900	0.514	0.105	0.002	8.6	0.83	0.17

Table 5.14: Systematic uncertainties for A_{FB}^t and cross section arising from theoretical uncertainties on the background normalization.

in the cross section measurement. For each background the systematic uncertainty on the cross section and A_{FB}^t was taken to be half the difference between the values observed for $\pm 5\%$. The overall uncertainty from the background normalization was taken to be the sum in quadrature of all the individual background uncertainties. The results of this study are shown in Table 5.14.

One can see that the normalization uncertainty on A_{FB}^t is relatively insignificant, however it is larger for the cross section as expected. In both cases the uncertainty is still dominated by the statistical component rather than the systematic.

5.6.2 Background Shape

As well as an uncertainty on the overall background normalization, there will also be a theoretical uncertainty on the shape of the background distribution. This is important to consider as A_{FB}^t is entirely dependent on the shape of the $\cos\theta$ distribution. In order to quantify any effect this could have, a linear gradient was introduced in the total background distribution before the nominal background is subtracted from each bin. By a linear gradient it is meant that the $\cos\theta = 1$ bin

Energy (GeV)	A_{FB}^t	ΔA_{FB}^t (Stat.)	ΔA_{FB}^t (Syst.)	σ (fb)	$\Delta\sigma$ (Stat.)(fb)	$\Delta\sigma$ (Syst.)(fb)
$P(e^-)=-80\%$						
$>=1200$	0.563	0.018	0.006	18.4	0.37	0.04
900-1200	0.546	0.034	0.015	11.0	0.38	0.09
400-900	0.458	0.081	0.013	16.6	1.31	0.08
$P(e^-)=+80\%$						
$>=1200$	0.621	0.024	0.006	9.8	0.28	0.03
900-1200	0.589	0.045	0.012	5.9	0.29	0.05
400-900	0.514	0.105	0.009	8.6	0.83	0.04

Table 5.15: Systematic uncertainties for A_{FB}^t and cross section arising from theoretical uncertainties on the background shape.

would be scaled by X%, the $\cos\theta = -1$ bin by -X% and all bins inbetween are scaled according to a linear distribution going from -X to X. A value of 2% was chosen for the gradient. The result of applying this gradient is shown in Table 5.15.

The uncertainty on the background shape causes a larger effect on A_{FB}^t than on the cross section as expected. Ultimately the total uncertainty is still dominated by the statistical component.

5.6.3 Luminosity

It is anticipated that an uncertainty of 0.3% can be achieved on the luminosity measurement at CLIC. Incorrect measurement of the luminosity will directly affect the cross section measurement as $\sigma = \mathcal{L}/N$, however it also has an indirect effect from the fact the background subtraction will no longer be correct which can affect the A_{FB}^t measurement. The effect of the luminosity uncertainty is shown in Table 5.16. Ultimately this effect is seen to be small compared to the uncertainty from the background normalization or statistical component.

Energy (GeV)	A_{FB}^t	ΔA_{FB}^t (Stat.)	ΔA_{FB}^t (Syst.)	σ (fb)	$\Delta\sigma$ (Stat.)(fb)	$\Delta\sigma$ (Syst.)(fb)
$P(e^-)=-80\%$						
$>=1200$	0.563	0.018	0.001	18.4	0.37	0.10
900-1200	0.546	0.034	0.001	11.0	0.38	0.10
400-900	0.458	0.081	0.001	16.6	1.31	0.13
$P(e^-)=+80\%$						
$>=1200$	0.621	0.024	0.001	9.8	0.28	0.05
900-1200	0.589	0.045	0.001	5.9	0.29	0.05
400-900	0.514	0.105	0.001	8.6	0.83	0.06

Table 5.16: Systematic uncertainties for A_{FB}^t and cross section arising from finite precision on integrated luminosity.

5.6.4 Bias Towards Generator A_{FB}^t

It is possible that in performing the bin by bin efficiency corrections to account for misreconstructed events a bias could have been introduced in the reconstructed A_{FB}^t . One way that this can be checked is by looking at the signal efficiency as a function of $\cos\theta$. If the efficiency corrections are only acting to correct for detector effects and not introducing a bias this distribution should be symmetric with a lower efficiency in the high $|\cos\theta|$ regions due to the detector acceptance. The signal efficiencies for each bin are shown in Figures 5.37 and 5.38. Note that without placing a cut on the lepton momentum in the lowest $\sqrt{s'}$ bin, an asymmetric efficiency distribution is observed. This is a result of the fact the efficiency for correctly identifying the lepton is worse for lower momentum leptons (see Section 5.2.1) and so the chance of the top charge tagging being incorrect increases in this region. When the top charge is misidentified, the reconstructed angle in the $t\bar{t}$ rest frame will be in the wrong hemisphere. Due to a non zero A_{FB}^t there will be a net migration from the forward to backward regions. Thus when looking at the ratio of events in a bin to the number of events at generator level, the bins in the backward region will appear to have a higher efficiency than the forward region.

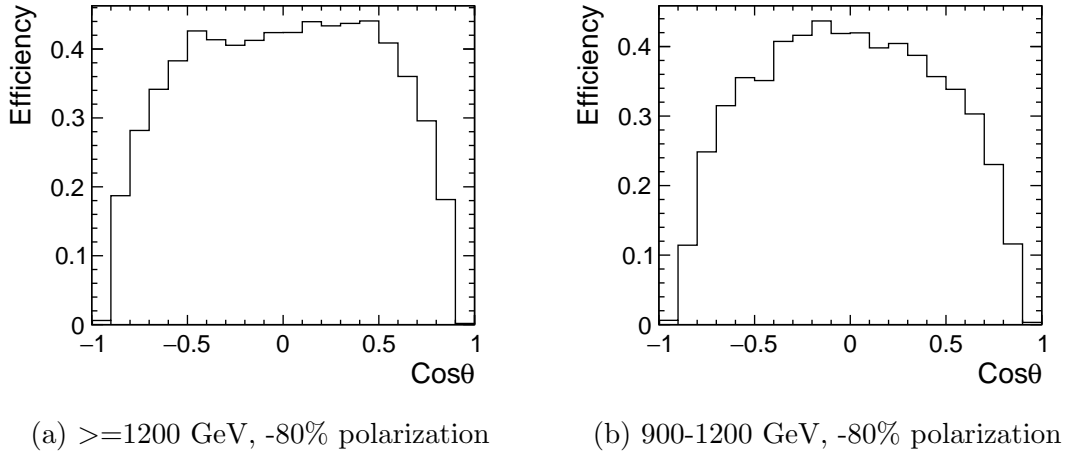


Figure 5.37: Efficiency for reconstructing signal events in the correct $\cos\theta$ bins

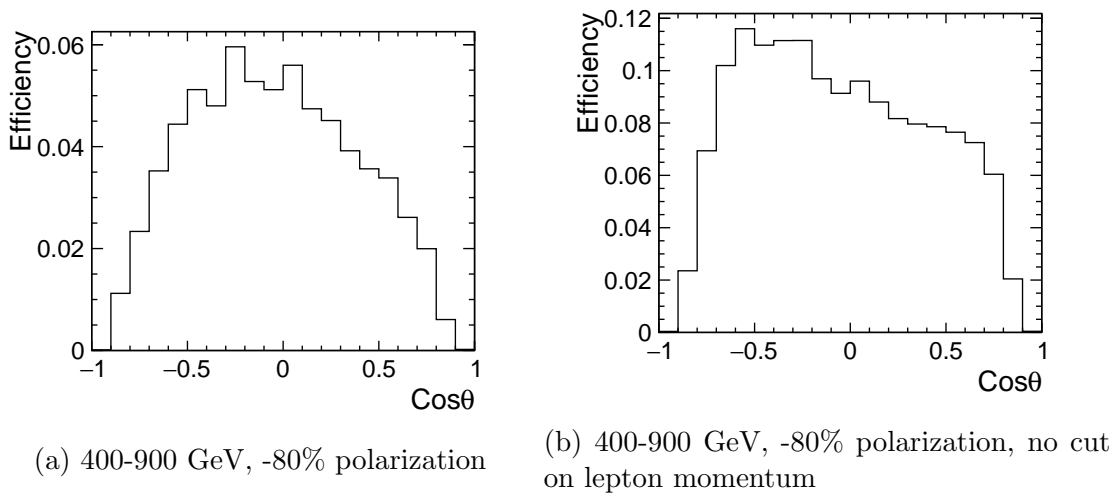
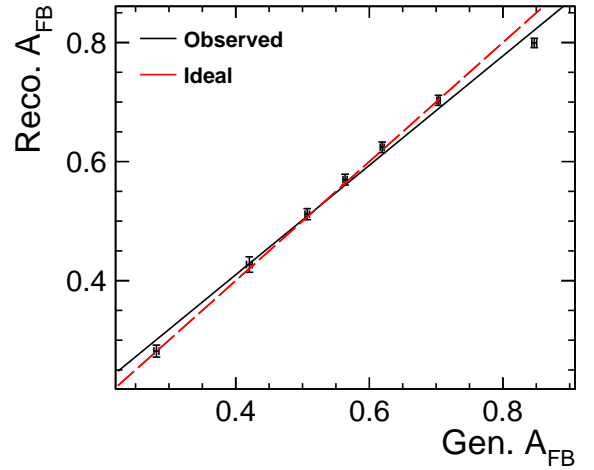
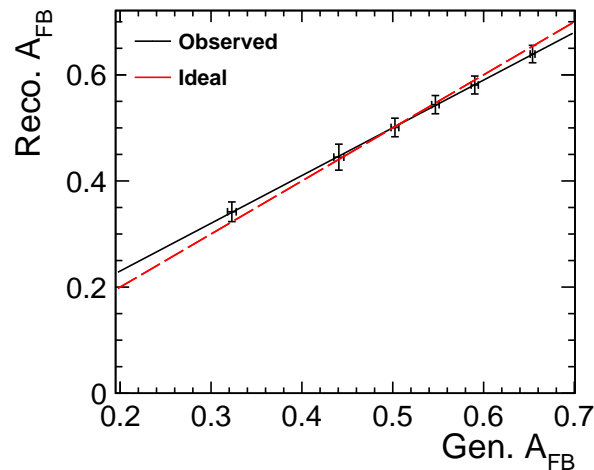


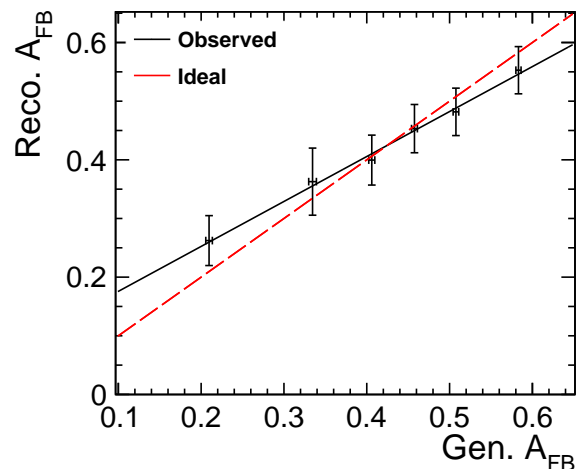
Figure 5.38: Efficiency for reconstructing signal events in the correct $\cos\theta$ bins

While the efficiencies do appear to be approximately symmetric, a more robust test could be performed by running the analysis on samples generated with a different A_{FB}^t and seeing what A_{FB}^t is obtained after reconstruction and event selection is performed. To avoid generating large new samples, samples with an alternative A_{FB}^t were produced by sampling the full signal sample using Eq. 5.17 with the desired A_{FB}^t as the probability density function. In all cases the signal efficiency corrections applied are those calculated for the nominal A_{FB}^t . To measure the bias a linear fit of the generator A_{FB}^t vs reconstructed A_{FB}^t was performed. In the ideal case these two quantities should be directly proportional returning a gradient of one. The distribution of the reconstructed and generator A_{FB}^t for each bin is shown in Figure 5.39.

In all cases a slight bias is seen with the high, middle and low energy fits yielding gradients of 9.2, 9.0 and 7.7 respectively. The fact the bias is largest in the lowest $\sqrt{s'}$ bin is to be expected as the efficiency corrections are largest in this bin. In all cases the fit reveals a bias towards the original generator values, with an A_{FB}^t greater than this being underestimated and vice versa. While this is not the ideal case, it should be noted that the relationship between the reconstructed and generator level A_{FB}^t is still linear and as such a simple mapping between the two can be applied to recover the generator level value. The fractional uncertainty introduced on A_{FB}^t from this additional correction corresponds to the fractional uncertainty on the gradient of the fits in Figure 5.39. It is further worth noting that the uncertainty on this fit has no dependence on measured values as the fit uses only simulated data. As such the uncertainties can in principle be made arbitrarily small with a large enough statistical sample. For now, the uncertainty is conservatively taken to be that seen for the current sample size for -80% polarization. For the +80% polarization the current sample sizes are significantly smaller and so would yield much higher uncertainties. As a result, it is assumed that the same fractional uncertainty on A_{FB}^t as seen for the -80% polarization could be achieved for the +80% polarization in future. The resulting uncertainty introduced on A_{FB}^t for each polarization is shown in Table 5.17.

(a) ≥ 1200 GeV

(b) 900-1200 GeV



(c) 400-1200 GeV

Figure 5.39: Correlation between the reconstructed and generator A_{FB}^t for each $\sqrt{s'}$ bin, -80% polarization.

Energy (GeV)	A_{FB}^t	ΔA_{FB}^t (Stat.)	ΔA_{FB}^t (Syst.)
$P(e^-)=-80\%$			
$>=1200$	0.563	0.018	0.014
900-1200	0.546	0.034	0.023
400-900	0.458	0.081	0.029
$P(e^-)=+80\%$			
$>=1200$	0.621	0.024	0.015
900-1200	0.589	0.045	0.024
400-900	0.514	0.105	0.032

Table 5.17: Systematic uncertainties accounting for bias in A_{FB}^t from signal efficiency corrections

The systematic effect of the bias is seen to produce the largest systematic uncertainty on A_{FB}^t , however it is still less than the statistical component.

5.6.5 Unquantified Effects

As well as the effects above which have been found to have significant contributions to the overall uncertainty on the measurements, several other effects have been examined but found to have negligible impacts on the final measurements and as such are not quantified here. There are three main effects of this type:

The first of these was the effect of the fit range. This was assessed by simply varying the range of $|\cos \theta|$ over which the fit is performed from 0.7 to 1.0 in 0.1 intervals. This was shown to change the statistical precision on the final result but not the central values for A_{FB}^t or the cross section. This is somewhat to be expected as the distribution still has the correct shape in the central region and so the fit should still extract the same values as are seen at generator level.

The second effect was from changing the values used for the BDT cut. Again this was found to only effect the uncertainty on the final results but not the central

value as it only changes the signal to background ratio, but as the background is subtracted anyway this has no effect on the final distribution, only on the statistical uncertainty of each bin.

The final effect was considered was the relative performance of the electron and muon signal channels. While this is not something that should change the final results, a large difference between the two channels could indicate an area for improvement in future. The performance of each channel was evaluated by excluding the other lepton channel from the analysis entirely and then looking at how the final fit results and their uncertainties changed, accounting for the slightly different cross sections for each channel. Ultimately it was found that the central values of the fits were in agreement but that the electron channel had a slightly worse uncertainty. This arises from the arguments already described in Section 5.2.1, which state that because the electron reconstruction only relies on two detector components (the tracker and ECAL) it has a higher chance of being missed or wrongly identified as a photon compared to the muon which penetrates the full detector. Events in which the electron is not correctly reconstructed will typically be removed by the quality cuts of the analysis leading to a reduced signal efficiency. Thankfully however, due to the fact the lepton finding presented here is based on the Pandora Particle ID (PID) of the particles, due to the ongoing efforts to improve Pandora it is likely that the efficiency in this channel will improve by the time the measurement can be performed.

As well as these effects that are not quantified as they are found to be negligible, there is one unquantified effect that should be taken into account when performing the measurement. As already mentioned, the centrally produced CLIC samples currently only use one event generator and hadronization handler (WHIZARD and PYTHIA). Ideally one would try several different monte carlo models for the analysis to see if there is a systematic effect from the modelling. This is particularly true here where the jet substructure variables used for event selection could be particularly sensitive to the hadronization modelling. Efforts have been made to remain as insensitive to the modelling as possible (such as using “microjets” rather than PFOs

for calculating these variables,) however the sensitivity is something that should be quantified in future.

5.6.6 Summary

The culmination of all the sources of uncertainty examined in the analysis is shown in Figure 5.18. One can see that the uncertainty on all quantities is ultimately dominated by the statistical uncertainty. It is possible that several of the systematic uncertainties could be reduced in future, particularly the signal efficiency bias that is dependent on the number of events generated. As such the values given here likely represent a conservative estimate of the systematic uncertainty.

5.7 Improvements

While the work here is considered complete, there are still potential improvements that could be made between now and the time at which the measurement would be performed. The most minor of these would be to optimise the quality cuts used for each energy bin. This might yield a slight improvement in the statistical precision for the lowest energy bins as this could improve the signal efficiency, however as the low signal efficiency is largely a result of the failed reconstruction of the top in this region, the improvement is unlikely to be large. A larger improvement could be achieved by instead entirely changing how the reconstruction of the tops is performed in this region. Because the decay products of the tops will be less collimated in this region, it may be possible to fully resolve all four quark jets within the event allowing for a more reliable reconstruction of the top that is less sensitive to overlapping fat jets. In practice this would likely warrant a dedicated study, separate to the higher $\sqrt{s'}$ analysis.

As already mentioned, one significant missing component from the study at the minute is an understanding of the systematic uncertainty associated with the hadroniza-

$P(e^-) = -80\%$							
Energy (GeV)	A_{FB}^t	Stat.	Systematic Effects				
			Total	Bias	Lumi.	Bkg Norm	Bkg Shape
≥ 1200	0.563	0.018	0.015	0.014	0.001	0.003	0.006
900-1200	0.546	0.034	0.028	0.023	0.001	0.006	0.015
400-900	0.458	0.081	0.032	0.029	0.001	0.006	0.013
$P(e^-) = +80\%$							
Energy (GeV)	σ (fb)	Stat.	Systematic Effects				
			Total	Bias	Lumi.	Bkg Norm	Bkg Shape
≥ 1200	18.41	0.37	0.29	–	0.10	0.27	0.04
900-1200	11.01	0.38	0.31	–	0.10	0.28	0.10
400-900	16.56	1.31	0.48	–	0.13	0.46	0.08

$P(e^-) = +80\%$							
Energy (GeV)	A_{FB}^t	Stat.	Systematic				
			Total	Bias	Lumi.	Bkg Norm	Bkg Shape
≥ 1200	0.621	0.024	0.016	0.015	0.001	0.003	0.006
900-1200	0.588	0.045	0.027	0.024	0.001	0.003	0.012
400-900	0.514	0.105	0.034	0.032	0.001	0.002	0.010
$P(e^-) = +80\%$							
Energy (GeV)	σ (fb)	Stat.	Systematic				
			Total	Bias	Lumi.	Bkg Norm	Bkg Shape
≥ 1200	9.84	0.28	0.14	–	0.05	0.13	0.03
900-1200	5.87	0.29	0.14	–	0.05	0.13	0.05
400-900	8.63	0.83	0.19	–	0.06	0.17	0.04

Table 5.18: Summary of statistical and systematic uncertainties for both polarizations and all energy ranges

tion modelling. While it is not currently possible to study this within the current ILCSoft framework, this is certainly something that will be investigated in future before the measurement is performed. On a related note of improving ILCSoft, further improvement could be made with the development of a tau finder package. Currently the signal channel only consists of states where the leptonic top produces an electron or muon. If taus could be reliably found, the signal cross section could optimistically be increased by a factor of $\sim 50\%$ by including the tau channel. This would also mean a reduction in the background as the tau channel would no longer be included.

A final potential improvement that has yet to be mentioned is the optimization of the luminosity split between each polarization. Currently it is assumed that the same integrated luminosity will be accrued for each beam polarization, however as can be seen in the current results, due to the lower cross section of the signal channel in the $+80\%$ polarization configuration the expected statistical precision for the variables measured for this polarization is worse. In order to perform a full optimization of the luminosity division it would be necessary to look both at the end effect on the precision of the electroweak form factors of the $t\bar{t}X$ vertex as well the effect on the wider CLIC physics programme. As such it is not clear what the optimal division should be, however it is likely that an even split between both run configurations is not optimal.

5.8 Conclusions

In summary, we have presented an analysis looking at the measurement of the top forward backward asymmetry and $t\bar{t}$ cross section with the aim of probing the electroweak form factors of the $t\bar{t}X$ vertex. To maximise the available information the analysis was split into six bins corresponding to three different energy ranges and two different beam polarizations. Events were reconstructed using large radius fat jets to account for the highly collimated nature of the top decay products, and

Energy (GeV)	$A_{FB}^t \pm \text{Stat.} \oplus \text{Syst.}$	$\sigma \pm \text{Stat.} \oplus \text{Syst.}$
<hr/>		
P(e^-)=-80%		
>=1200	$0.563 \pm 0.018 \oplus 0.015$	$18.41 \pm 0.37 \oplus 0.29$
900-1200	$0.546 \pm 0.034 \oplus 0.028$	$11.01 \pm 0.38 \oplus 0.31$
400-900	$0.458 \pm 0.081 \oplus 0.032$	$16.56 \pm 1.31 \oplus 0.48$
<hr/>		
P(e^-)=+80%		
>=1200	$0.621 \pm 0.024 \oplus 0.016$	$9.84 \pm 0.28 \oplus 0.14$
900-1200	$0.588 \pm 0.045 \oplus 0.027$	$5.87 \pm 0.29 \oplus 0.14$
400-900	$0.514 \pm 0.105 \oplus 0.034$	$8.63 \pm 0.83 \oplus 0.19$

Table 5.19: Final summary of the expected precisions attainable from the $t\bar{t}$ analysis.

the substructure of these fat jets was used to perform event selection. The event selection was performed in two main sections. Initially cuts are applied to remove easily identifiable backgrounds and events in which the reconstruction has failed. Following this a pair of BDTs are used to remove remaining background events with one BDT trained to select high energy events and the other trained on low energy events. The selection was found to give high efficiencies for high energy bins and significantly lower efficiency for lower energy bins due to poor jet reconstruction at this scale. The cross section and A_{FB}^t are extracted using a second order fit to the production angle of the top following the subtraction of any remaining backgrounds and correction for finite signal efficiency. The results of applying this method are summarised in Table 5.19. A detailed study of various systematic effects revealed that in all cases the uncertainty is dominated by the statistical component with the dominant systematic contributions for the cross section and A_{FB}^t coming from the background normalization and bias introduced during efficiency corrections respectively. The final precision was found to be an order of magnitude better than what is seen at the LHC[62] and is consistent with results obtained for an alternative version of the analysis[2] when accounting for the lower signal efficiency of the alternative version.

CHAPTER 6

Digital Calorimetry

6.1 Introduction

As mentioned in Section 2.4.1.3, several alternatives exist for the ECAL design of ILD. Here we present details of a proposed fully digital ECAL that simply counts the number of pixels above threshold rather than measuring the energy deposited in each pixel. This works based on the fact that the number of particles produced by an electromagnetic shower is proportional to the energy of the incident particle producing it.

The digital approach has several potential benefits. Fundamentally it should allow for a slight improvement in the energy resolution as it is less sensitive to uncertainties arising from landau fluctuations and varying path lengths as the particle traverses the active material. In order to observe every particle within a shower any choice of DECAL technology must have an extremely high granularity ($\mathcal{O}(50\mu m)$). This

ultra high granularity has the potential to improve the performance of particle flow algorithms by allowing for better pattern recognition and association of tracks to ECAL deposits. Lastly, as will be discussed below, the natural choice of technology will be to use CMOS MAPS. As this is the same technology as is proposed for the inner tracking systems this would allow a uniform technology solution to be used across multiple detector components. It is also a cheaper technology option than that used by the alternative ECAL designs due to the prevalence of CMOS in commercial products.

While the digital option provides these benefits it does come with one potential flaw referred to as saturation. In a digital calorimeter, if two particles pass through the same pixel, only one hit will be registered and so the total number of particles in the shower (and thus the energy of the shower) will be underestimated. The density of an EM shower scales according to the energy of the showering particle. As a result the rate of multiple occupancy in the pixels will increase with energy leading to a non linear relationship between a particles energy and the number of hits it generates within the detector. In practice this problem can be avoided by ensuring that the granularity of the detector is always greater than the density of the electromagnetic showers. For typical ILC energies the density of the showers is estimated to be $\mathcal{O}(100)$ particles/mm² and so a granularity of at least $50 \times 50 \mu\text{m}^2$ is required to ensure only one particle hits each pixel. Note that in the analogue case this problem does not occur as the energy deposited in the pixel is what is measured and this scales with the number of particles passing through the pixel.

The requirement on the granularity is what ultimately leads to the decision to use a MAPS based technology. For ILD, using $50 \times 50 \mu\text{m}^2$ pixels requires the use of $\mathcal{O}(10^{12})$ pixels. Having separate readout electronics, along with cooling and power supplies for each cell becomes impractical and produces large dead space within the detector. By using MAPS technology the electronics can instead be integrated into the silicon of the pixels leading to a more compact structure. CMOS is then chosen as it is a cheap, well understood and commercial process for producing MAPS structures. The typical layout of a CMOS MAPS pixel is shown in Figure 6.1. In practice this

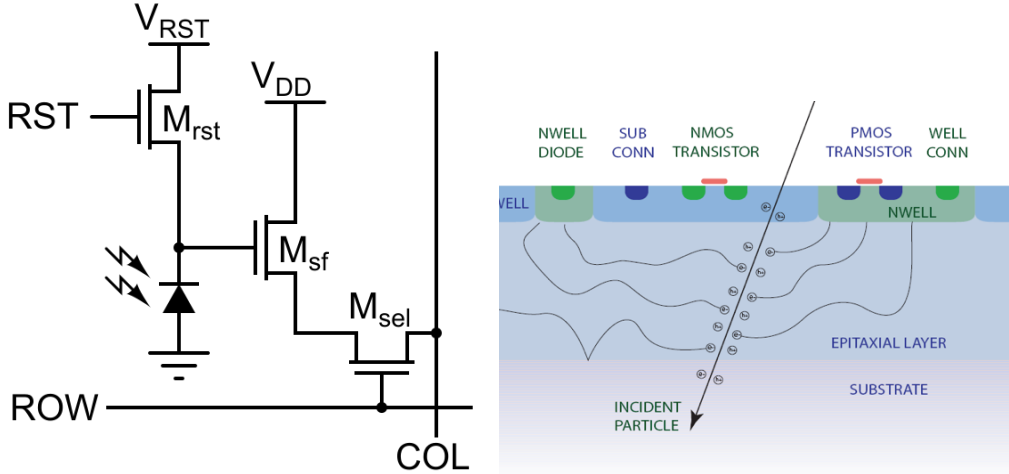


Figure 6.1: Left: Schematic of the simplest layout for a CMOS sensor using just three transistors. The first transistor, M_{rst} , acts as a switch to reset the charge collected at the diode. M_{sf} allows the charge of the diode to be measured and amplified without removing the charge. Finally M_{sel} controls when the signal is read out from the pixel. Right: physical layout of a typical CMOS pixel sensor.

simple design is found to be unsatisfactory for use in particle physics due to the low signal yield due to parasitic losses to the PMOS transistor. A process referred to as INMAPS was developed at Rutherford Appleton Laboratory (RAL)[63] which uses the addition of a deep p well around the PMOS transistor to mitigate the signal loss. The layout of this variation is shown in Figure 6.2. Two sensors based on the deep p well design have already been produced (TPAC[64] and CHERWELL[65]) and used to show the validity of this approach for producing a DECAL[66]. In both cases the test pixels were based on a $50 \times 50 \mu\text{m}^2$ design.

Here we will present simulation studies looking at the optimization of the pixel dimensions for the sensors when including variation levels of realism such as noise, deadspace and clustering.

6.2 Event Generation and Detector Simulation

Simulation of the DECAL was performed in the GEANT4 based ILCSoft application, Mokka v08-05. The model used was based on an existing model for ILD, ILD_v01_05,

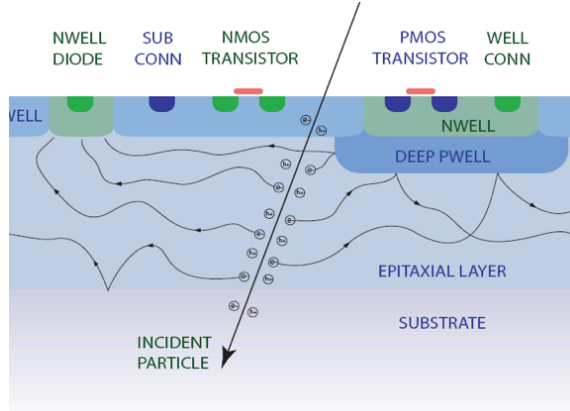


Figure 6.2: CMOS MAPS sensor including deep p well implant to prevent parasitic losses to the PMOS transistor[65]

and so includes the high level of detail implemented for the ILD letter of intent studies[26] e.g. realistic geometries including support structures. The design was then adapted in three main ways. Firstly, the $300\ \mu\text{m}$ thick active layer of silicon is divided into a thin active epitaxial layer ($10\text{-}20\ \mu\text{m}$) and a deeper passive layer of silicon ($280\text{-}290\ \mu\text{m}$). The thin active layer represents what would be used in a typical CMOS MAPS sensor while the deeper passive layer is only included to prevent the need for changing the detailed layer structure of the existing model. In practice such a deep passive silicon layer would not be used. Secondly, the pixel pitch was reduced down to $5\times 5\ \mu\text{m}^2$. This is smaller than can realistically be manufactured at present, however by using a narrow pixel pitch during the simulation the pixels can later be grouped together into larger virtual pixels with realistic dimensions preventing the need for simulating events at every pixel pitch required for the study and saving considerable processing time. The final change implemented was to remove the guard ring structures present in the analogue design. In the analogue design the guard rings are $1\ \text{mm}$ metal rings placed around wafers of 18×18 pixels. For the digital case these structures are not required and would result in a large amount of dead space in the detector due to the considerably narrower pixel pitch. On top of this the magnetic field present for ILD was turned off so that only the intrinsic ECAL performance would be measured.

Once the geometry was implemented, events were generated using the built in Mokka

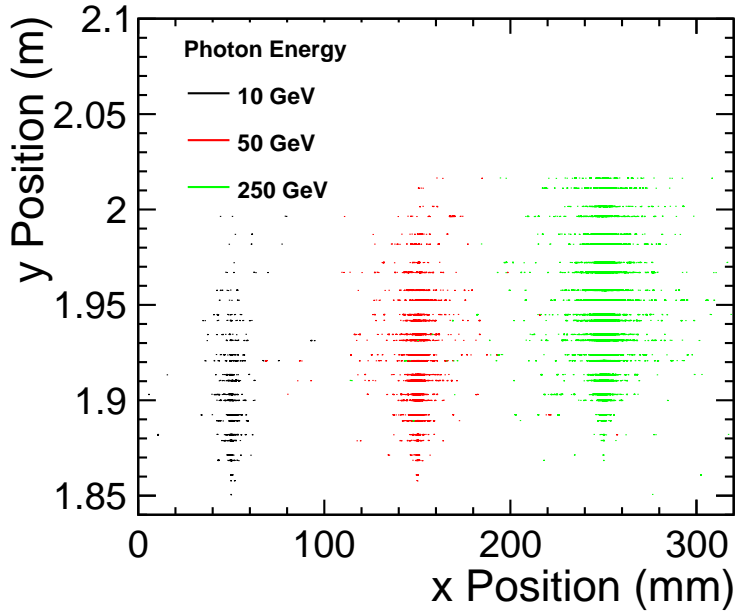


Figure 6.3: Example of how EM showers look in a DECAL with $10 \times 10 \mu\text{m}^2$ pixels for various photon energies. The y coordinate here represents the radial distance from the centre of the full detector.

particle gun to fire photons through the ECAL. When doing this the gun was placed perpendicular to the ECAL surface and immediately in front of the ECAL to prevent showers forming earlier in the detector from interactions with the inner components such as the tracker. Photon were produced in 10 GeV intervals between 10 GeV and 100 GeV. For each energy, 10,000 events were generated to produce a large enough statistical sample to work with. Events were then generated using five different epitaxial thicknesses between 12 and 20 μm . Additional samples were generated at 250 GeV representing the maximum energy possible at ILC. In this case only 5000 events were generated per epitaxial layer due to the considerably longer simulation times. In total this corresponds to a total of $\sim 500,000$ events generated. An example of what these events look like in the detector is shown in Figure 6.3.

In order to be realistic, thresholds were applied on the energy deposited in a pixel as in practice this is always necessary to remove hits coming from electrical/thermal noise. The amount of energy deposited by a particle in a thin layer of material will typically follow a landau distribution. The threshold was chosen to be half of the

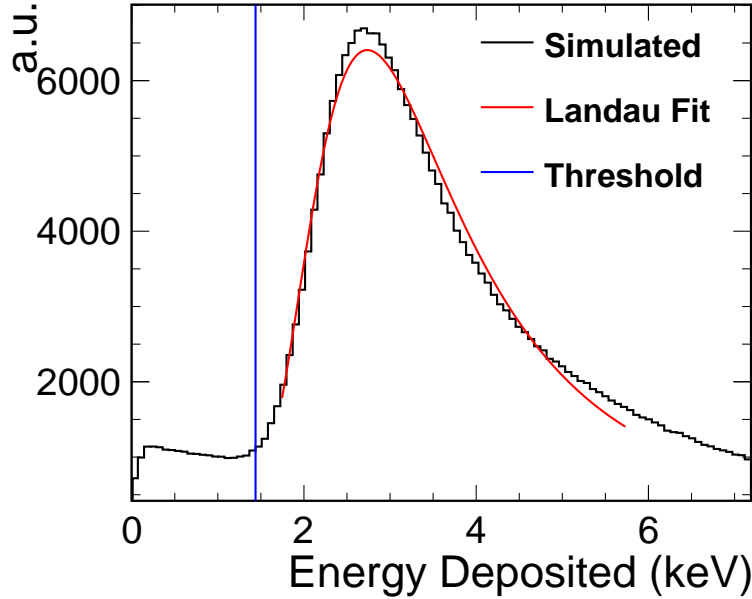


Figure 6.4: Energy deposited in a $100 \times 100 \mu\text{m}^2$ pitch, $12 \mu\text{m}$ thick pixel by a 10 GeV photon. The landau fit and resulting choice of threshold are also shown.

most probable value (MPV) of the landau distribution to provide a balance between the amount of signal loss and potential background acceptance. The value of the MPV was found by fitting the energy ditributions measured in the simulation. For doing this, 10 GeV photons and $100 \times 100 \mu\text{m}^2$ pitch pixels were used to prevent influence from saturation or from boundary effects where a particle deposits low amounts of energy from crossing the boundary between two pixels within one layer. As the amount of energy depsoited depends only on the epitaxial layer thickness and not the pixel pitch, the thresholds were only evaluated once for each epitaxial thickness then applied uniformly across all pitches. An example of one of the fits used in determining the threshold is shown in Figure 6.4.

6.3 Pixel Design Optimization

Ultimately the performance of any calorimeter is measured by the energy resolution, σ_E/E , it can achieve. As such it is important to explain how this is defined for a

digital calorimeter. Naively one could work on the basis that the energy of a particle is proportional to the number of particles produced in a shower and so define the resolution to be σ_N/N where N is the number of hits in the detector. While this is theoretically true, it fails to account for the fact the number of particles produced in the shower may not be proportional to the number of hits measured due to effects such as multiple occupancies. A more reliable definition of the resolution has been found to come from first creating a calibration curve defining the relationship between the true energy of a particle, then using this curve to map back from the number of particles to a reconstructed energy for a particle. The energy resolution is then calculated by performing a gaussian fit to the reconstructed particle energies and defining the resolution to be $\sigma_{E,Gaus}/E$. In the case of a perfect detector, this resolution should be equivalent to σ_N/N as N is linearly proportional to E . In all cases, the calibration curves are produced using one fifth of the statistical sample and the remaining four fifths are used to evaluate the energy resolution. Examples of how these calibration curves look for different pixel configurations are shown in Figure 6.5. For wider pixels it is observed that the energy to hits relationship becomes non linear indicating detector saturation is occurring.

Having generated the calibration curves, the energy resolution was then determined for every photon energy and pixel configuration. The performance for each pixel configuration is evaluated by performing a second order polynomial fit to σ_E/E vs $1/\sqrt{E}$ (see Figure 6.6). This method allows the parameters a , b and c to be extracted in accordance with Eq. 6.1, where a is the stochastic term, b is the noise term and c is the constant/leakage term. Typically the resolution of an ECAL can be expected to be dominated by the stochastic term.

$$\frac{\sigma_E}{E} = \frac{a}{\sqrt{E}} \oplus \frac{b}{E} \oplus c \quad (6.1)$$

The values of a , b and c for every pixel configuration are shown in Figures 6.7, 6.8 and 6.9. One can see that the stochastic and noise terms dominate the overall resolution, however they show very different dependencies on the pixel configuration.

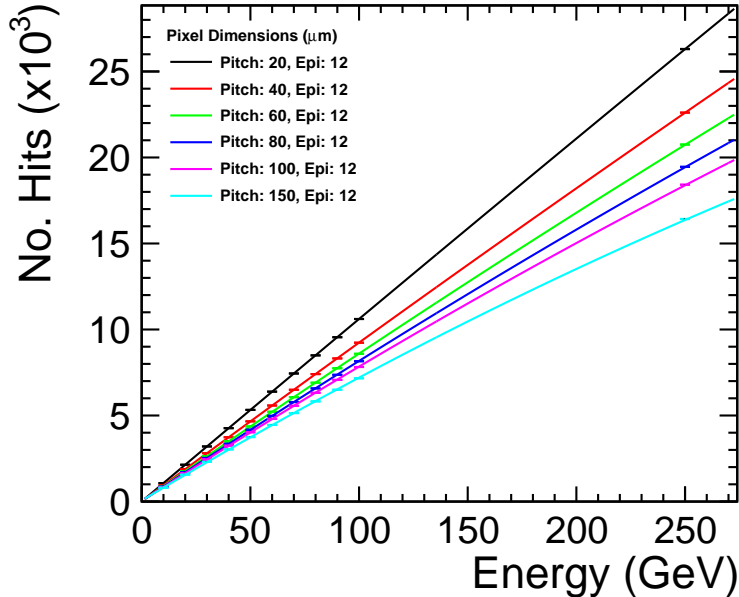


Figure 6.5: Calibration curves describing the relationship between the number of pixel hits observed and the energy of the incident particle for various pixel configurations.

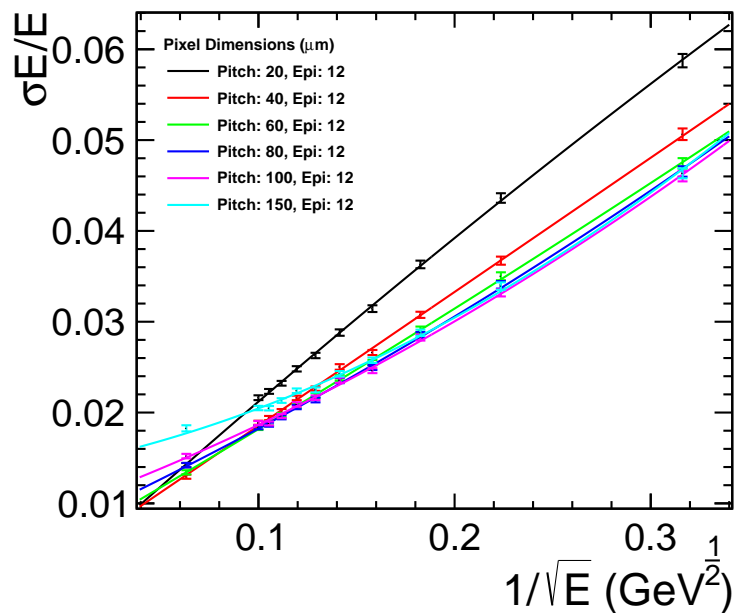


Figure 6.6: Energy resolution curves describing the variation of the energy resolution with the energy scale

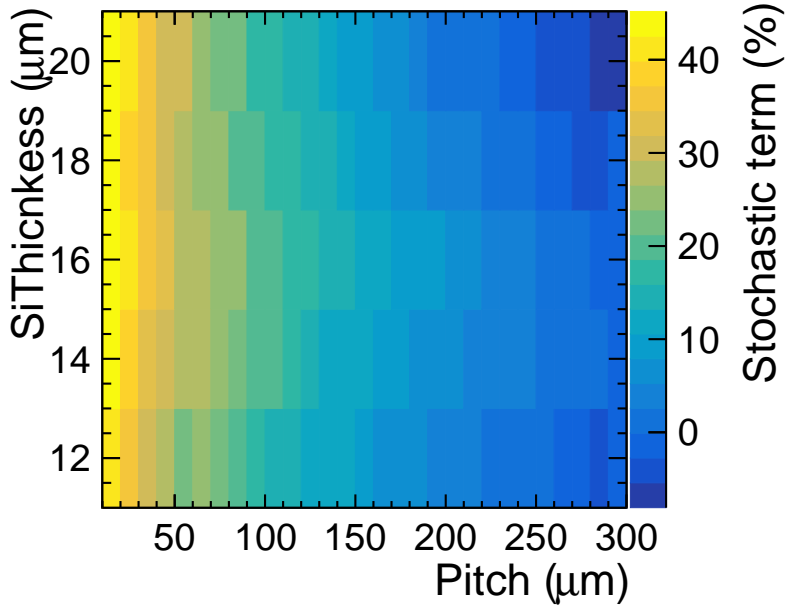


Figure 6.7: Stochastic term of the energy resolution fits for all pixel configurations

The stochastic is seen to be lowest for wider pixel pitches whereas the noise term is lowest for the narrower pitches. One can trivially explain the distribution in the noise term as arising from saturation effects as for wider pixels the granularity of the detector will be less than the density of the EM showers. This results in a non linear response for the detector which gets translated into a non linear energy resolution and so a large second order term in the $1/\sqrt{E}$ fit. Further evidence for this explanation can be seen in Figure 6.10 which shows the occupancy per pixel for 100 GeV events increases with pixel pitch. This effect is also easily seen in Figure 6.6 where for the wider pixels the performance is reasonably consistent for lower energies but diverges at the highest energies where saturation begins to occur making the resolution worse and introducing a second order term to the distribution.

To understand the stochastic term requires examination of the landau distributions as shown in Figures 6.11 and 6.12. One can see that as the aspect ratio decreases, a secondary peak appears in the energy deposition distribution at low energies. This is a result of particles crossing between pixels and so leaving only a fraction of the expected energy per layer in each pixel. The result of the boundary crossings is that

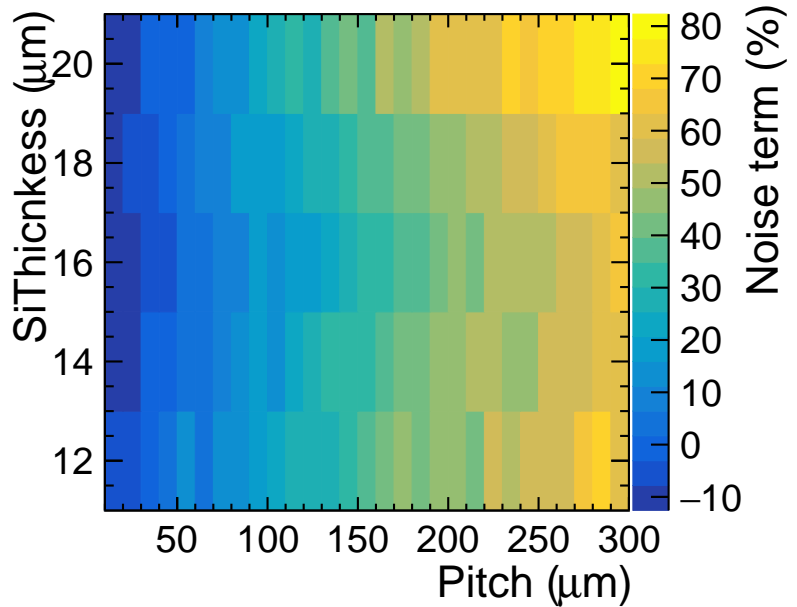


Figure 6.8: Noise term of the energy resolution fits for all pixel configurations

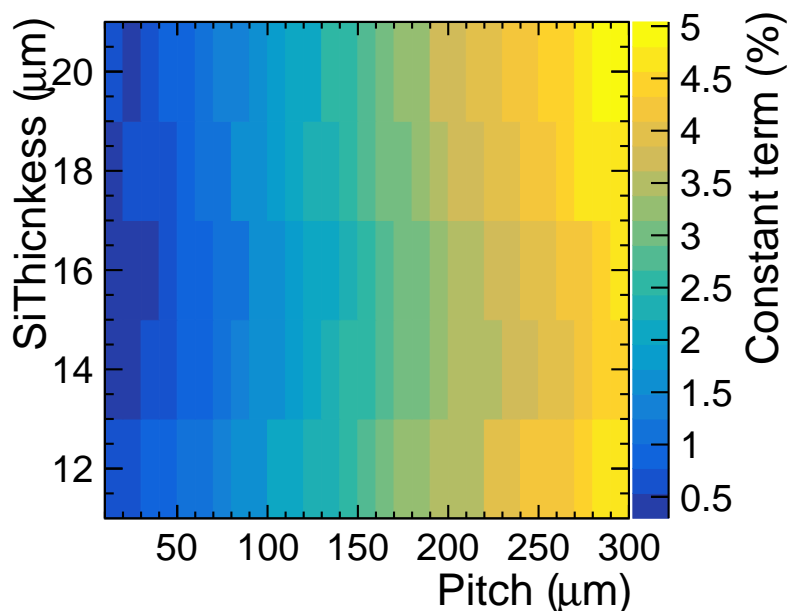


Figure 6.9: Constant term of the energy resolution fits for all pixel configurations

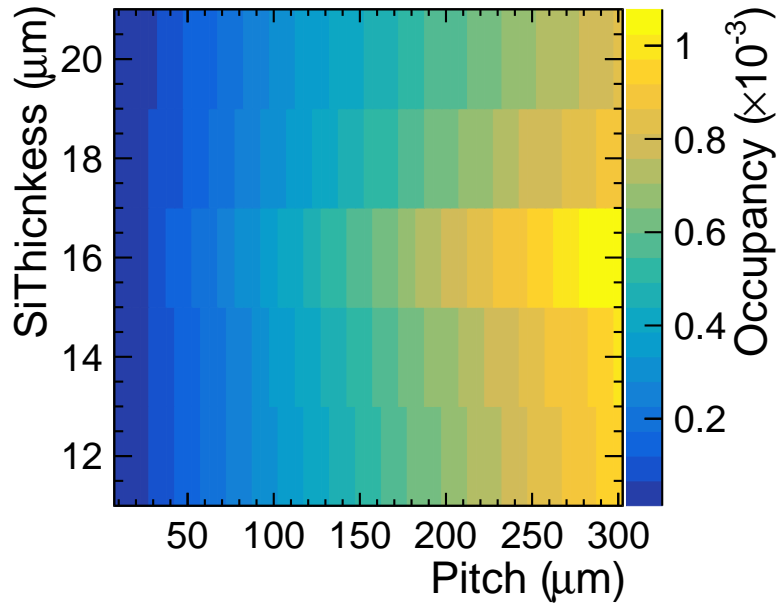


Figure 6.10: Pixel occupancy for 100 GeV photons.

there is a greater fluctuation on the number of pixels above threshold as rather than consistently observing one hit per particle per layer, it is possible to also get no hits if the deposits across both pixels are below threshold, or more likely an additional hit from both deposits being above threshold.

The optimal pixel configuration should provide a balance between the boundary crossing and multiple occupancy effects. Because the saturation level is a function of the incident particle energy, the optimal design will vary depending on the energy scale the detector is intended to be used at. For lower energy scales a wider pixel is optimal as the saturation is inherently low due to the low shower density and the wide pitch will then minimise boundary crossings. For higher energies the saturation rate will dominate and so a narrower pixel is preferred. In both cases a thinner pixel is preferred to minimise boundary crossings. The net resolutions observed at three different energy scales are shown in Figures 6.13, 6.14 and 6.15. The variation in the optimal configuration is seen to agree with that predicted from the above boundary crossing and occupancy considerations.

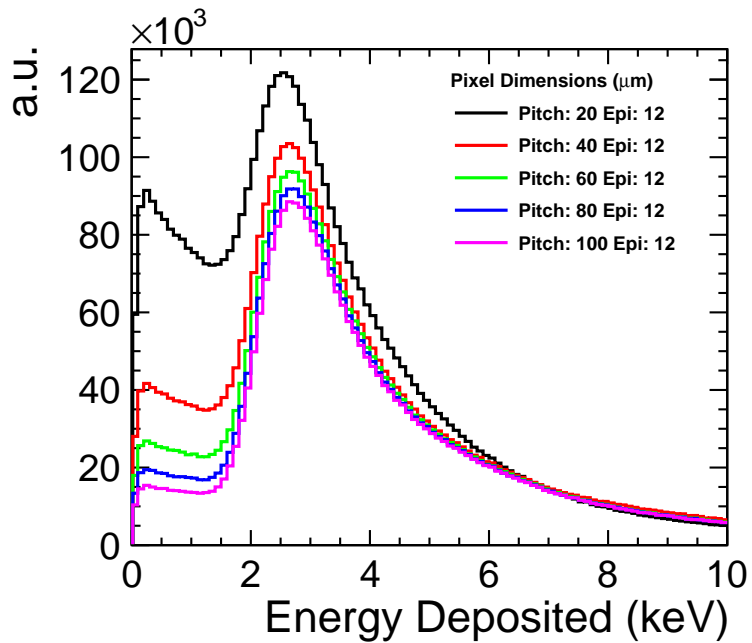


Figure 6.11: Variation in the landau distributions for 10 GeV photons as a function of the pixel pitch. All distributions normalised to unity.

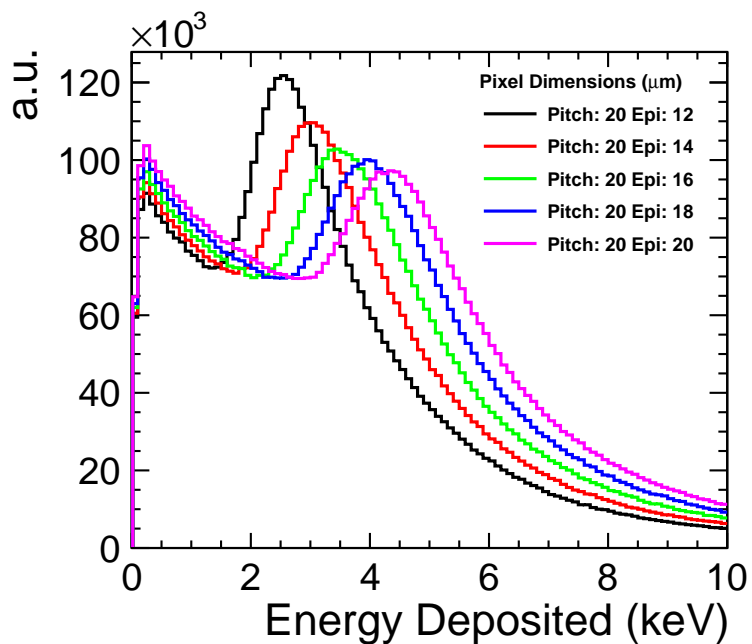


Figure 6.12: Variation in the landau distributions for 10 GeV photons as a function of the epitaxial thickness. All distributions normalised to unity.

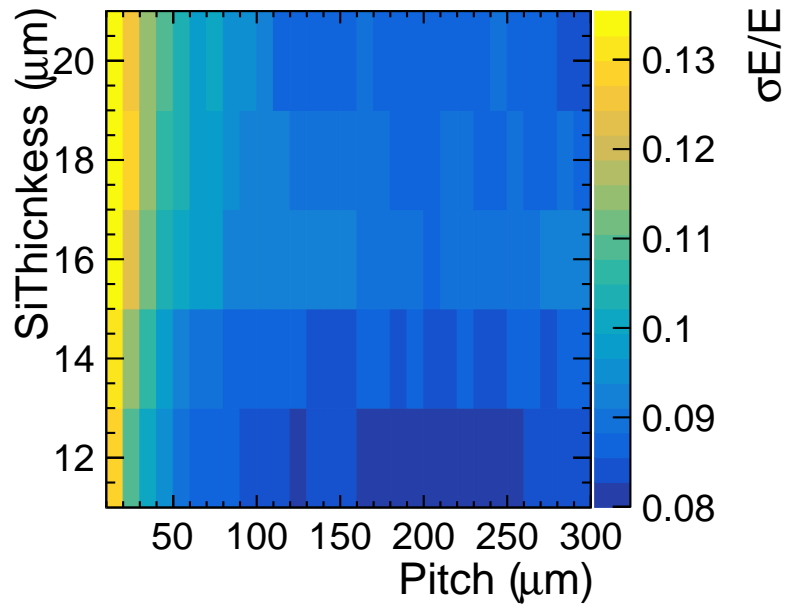


Figure 6.13: Energy resolution for 10 GeV photons.

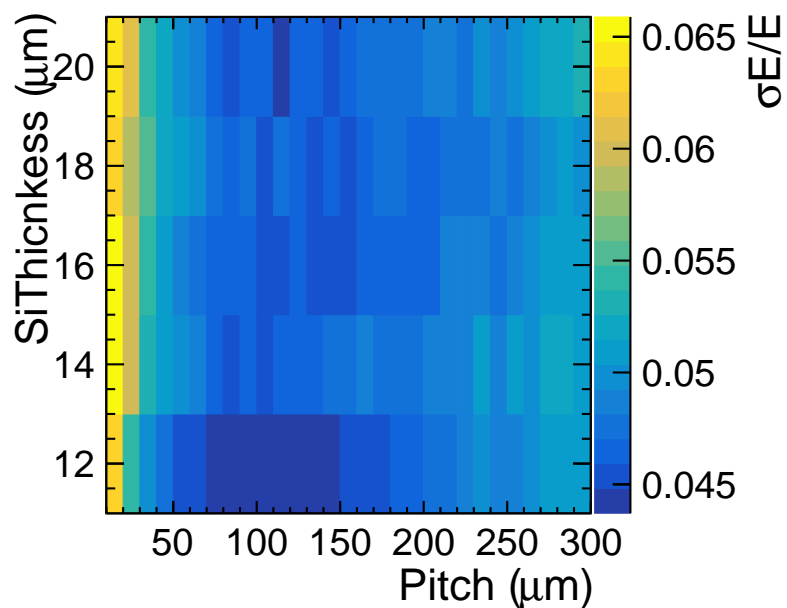


Figure 6.14: Energy resolution for 50 GeV photons.

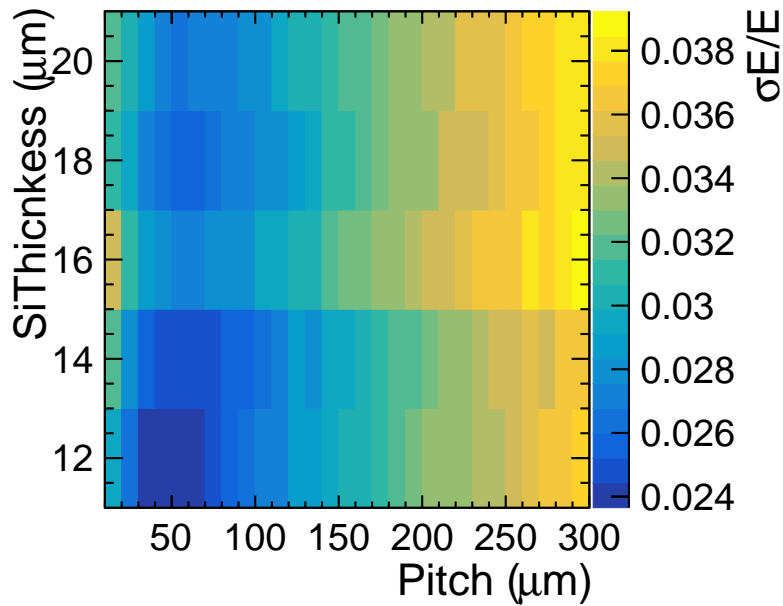


Figure 6.15: Energy resolution for 250 GeV photons.

6.4 DigiMAPs

While the above simulations highlight the dominant effects that must be considered in designing a digital calorimeter, they remain somewhat unrealistic. In particular they lack effects such as charge collection efficiencies within the pixels, thermal/electronic noise and the effects of clustering. These effects are not possible to study within standard GEANT4 simulations, instead they are added in later using a package referred to as DigiMAPs developed by the CALICE collaboration. This package takes the output hits from MOKKA, applies the effects of added levels of realism to remove/create new hits, then outputs an updated collection of hits for analysis. The effects that have been considered are listed below.

- Charge spread: When a particle deposits energy within a pixel it does so by producing electron hole pairs within the material which are then collected by diodes. In practice, there will be a finite efficiency for collecting the deposited charge which will depend on how the collection diodes are placed throughout the pixel and where the particle enters the pixel. Modelling of the charge

collection requires detailed TCAD simulations performed using external software. Within DigiMAPS, the modelling of this is provided for only one pixel configuration corresponding to a pixel with $50 \mu\text{m}$ pitch, $18 \mu\text{m}$ epitaxial thickness and four charge collection diodes arranged in a square. DigiMAPS used the efficiency map for this configuration to apply an efficiency scaling on the energy deposited by a particle based on where within the pixel it enters. Unfortunately the software required to create the efficiency maps is not readily available and so it was not possible to examine how the charge efficiency impacts any other pixel configuration.

- **Noise Effects:** It is possible for noise to be produced either from thermal fluctuations within the silicon or from the electronics associated with the diode and readout systems. For DECAL applications it is expected that the noise will follow a poisson distribution with a mean of 30 electron hole pairs per pixel. This noise is typically problematic as it can result in fake hits being produced in pixels with no signal contribution leading to overcounting of hits, however it can also be beneficial in the case of genuine hits where it can push hits with low energy deposits above the threshold preventing them from being missed. As such, in later plots the noise contributions will be split into the cases where noise is only added to pixels containing signal deposits and when it is added to all pixels throughout the detector.
- **Dead space:** In order to accomodate the necessary electronics required for each pixel, there will typically be a certain amount of dead space per pixel which will be insensitive to any particles hitting it. Within DigiMAPS this is accounted for by ignoring hits within the first 10% of the width of each pixel.
- **Threshold spread:** Due to imperfections in the pixel manufacturing process, pixels will typically show a non uniform response to incoming particles. This effect is normally minimised via a calibration procedure known as trimming which effectively corresponds to measuring the response of each pixel and setting the thresholds accordingly to get a uniform response. For the level of logic available within proposed DECAL designs it is expected that this procedure will

leave only a 1% non uniformity in the pixel response. This is accounted for within DigiMAPS by applying a gaussian spread to the threshold of each pixel with a width of 1%.

- Clustering: In any realistic experiment, the energy resolution of a calorimeter will not be taken to be the sum of all energy deposited within the calorimeter, instead some level of pattern recognition will be done to remove noise events and group signal hits to reduce the volume of data being read from the detector. This process is referred to as clustering. Here we use a very simplistic clustering method to illustrate the benefits it can have. For each hit the number of immediately adjacent hits are counted. If all 8 adjacent pixels contain hits, the pixel is deemed a cluster and the neighbouring hits are discarded. If no adjacent pixels are hit then the pixel will simply be declared a cluster by itself. If 1-7 of the adjacent pixels have hits, each neighbour is examined and assigned a score corresponding to the number of its neighbours that contain hits. The scores of the original hit and all its neighbours are compared and the pixel with the highest score is declared to be a cluster and its neighbours are removed.

To understand how the effect these different factors have on the energy resolution, the energy resolution for a specific pixel configuration and photon energy ($50 \mu\text{m}$ pitch, $18 \mu\text{m}$ epi, 20 GeV photons) is plotted as a function of the threshold applied to the pixels after each additional level of realism is included. This is shown in Figure 6.16. In the most simplistic case with no effects added, one can see that the choice of threshold has little effect in the range examined as the threshold range is far below the peak in the landau, with only a small improvement seen for higher thresholds where the effect of boundary crossings is reduced. Adding charge spreading results in less energy being deposited in the pixel, effectively lowering the landau peak. As such, the resolution is seen to get worse as the threshold increases as a large proportion of the signal hits are being removed by the threshold. It is also possible that charge can diffuse into neighbouring pixels resulting in an increased number of fake hits and so a greater fluctuation on the number of pixels fired. The

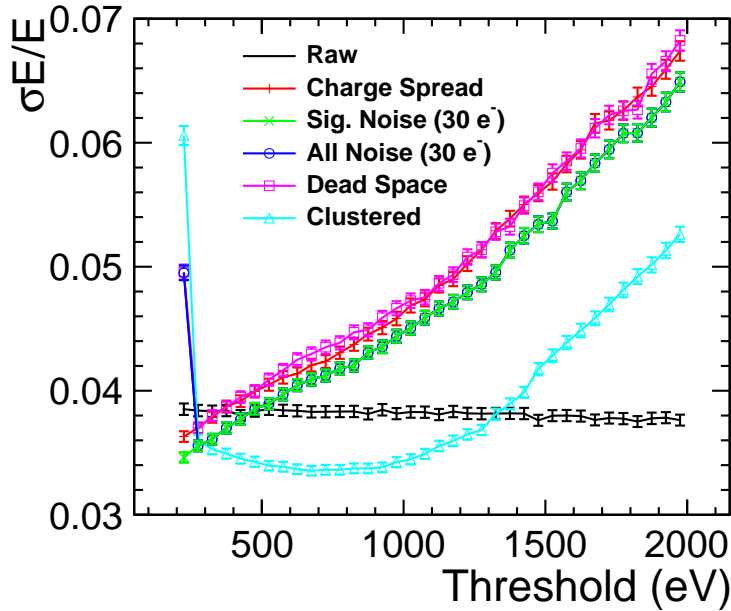


Figure 6.16: Variation in the energy resolution as a function of the threshold applied after each DigiMAPS effect is added. The effects are added sequentially in the order displayed in the legend.

effect of noise is broken down into the cases where the noise is only added to genuine signal hits and where it is added to all pixels. One can see that adding noise to the signal hits results in an improved performance as less hits are lost due to the threshold. Including noise in all the pixels has little effect at higher thresholds as the threshold is above the energy generated by the noise and so no additional hits are being created. For very low thresholds, hits can be generated from the noise alone which results in a significantly worse resolution. Including dead space has the effect of making the resolution worse across all thresholds as it simply results in consistent undercounting of the number of hits in the detector. Adding clustering improves the resolution for all but the lowest thresholds (where the hits are dominated almost entirely by noise effects,) even providing better performance than the raw pixel counting with minimal realism. The broad optimal resolution range after clustering also shows that the detector should be relatively insensitive to threshold variations between pixel. The improved resolution performance is a result of the clustering removing additional hits caused by the charge spread or boundary crossings leading to the number of hits measured being a more consistent and accurate

representation of the true number of pixels hit by the shower. Note that while this improvement is observed for the particular energy and pixel configuration shown above, it is expected that for wider pixels and higher energies, the clustering will ultimately result in the resolution getting worse as when the detector is close to saturation genuine hits will start to occur in adjacent cells and so the clustering will remove genuine hits. Ultimately this reduced performance might be avoidable in future by developing a more sophisticated clustering algorithm that uses pattern recognition to identify whether a hit is likely to be from an EM shower or just from noise.

6.4.1 Pixel Design Optimization Revisited

After the additional levels of realism have been included, it is important to evaluate the impact they have on the optimal pixel configuration. Note that the charge spread is not included here as the necessary sub-pixel simulations required as input for each pixel configuration do not exist. The resulting distributions for the stochastic, noise and constant terms are shown in Figures 6.17, 6.18 and 6.19.

Note that in some cases the resolution is seen to become negative, particularly for wider pixel dimensions. This occurs when the resolution becomes so dominated by non linearities that the fit fails to accurately determine the resolution parameters. As such these regions are immediately ruled out as possible design choices.

Again, to determine the optimal pixel configuration a relevant energy scale must be chosen as many of the effects controlling the resolution have a strong energy dependency. The resolution observed at the three working points of 10 GeV, 50 GeV and 250 GeV are shown in Figures 6.21, 6.22 and 6.23. One can see that the net effect of including these effects is to shift the optimal resolution point to a narrower pixel pitch. This is predominantly a result of the clustering algorithm being included as highlighted by Figure 6.20 which shows the optimal resolution point at 10 GeV is relatively unchanged when including all DigiMAPS effects except the

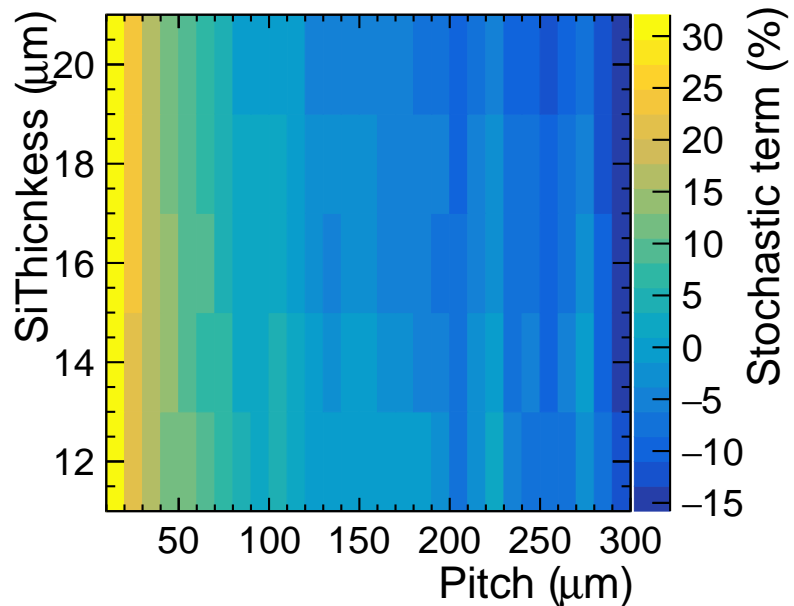


Figure 6.17: Stochastic term of the energy resolution fits for all pixel configurations when including clustering, noise, dead space and threshold spread.

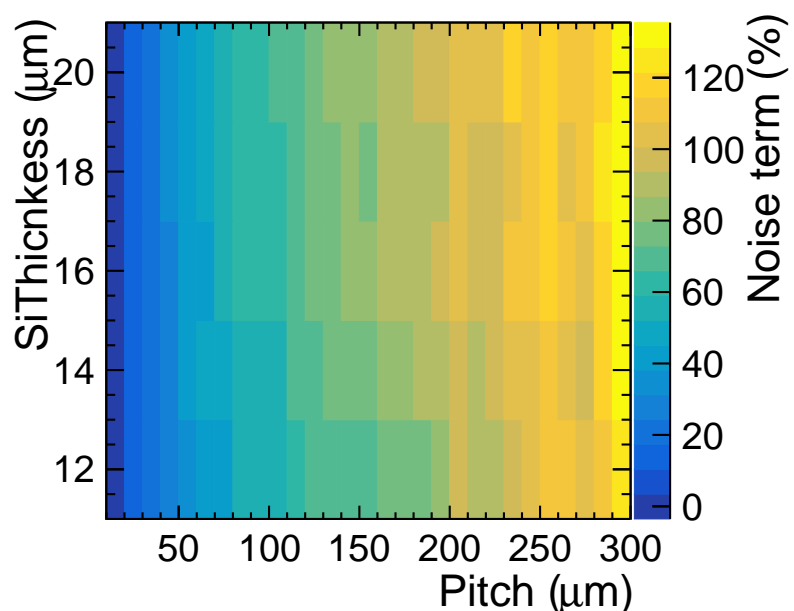


Figure 6.18: Noise term of the energy resolution fits for all pixel configurations when including clustering, noise, dead space and threshold spread.

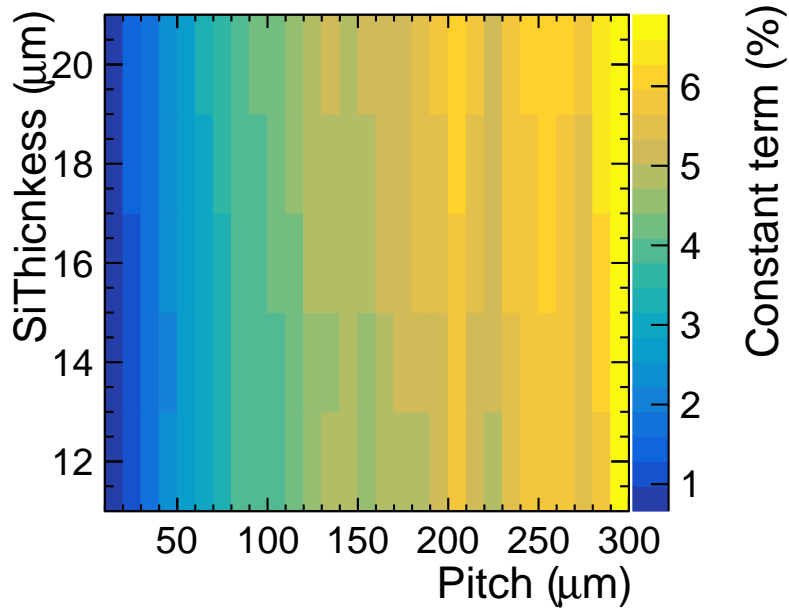


Figure 6.19: Constant term of the energy resolution fits for all pixel configurations when including clustering, noise, dead space and threshold spread.

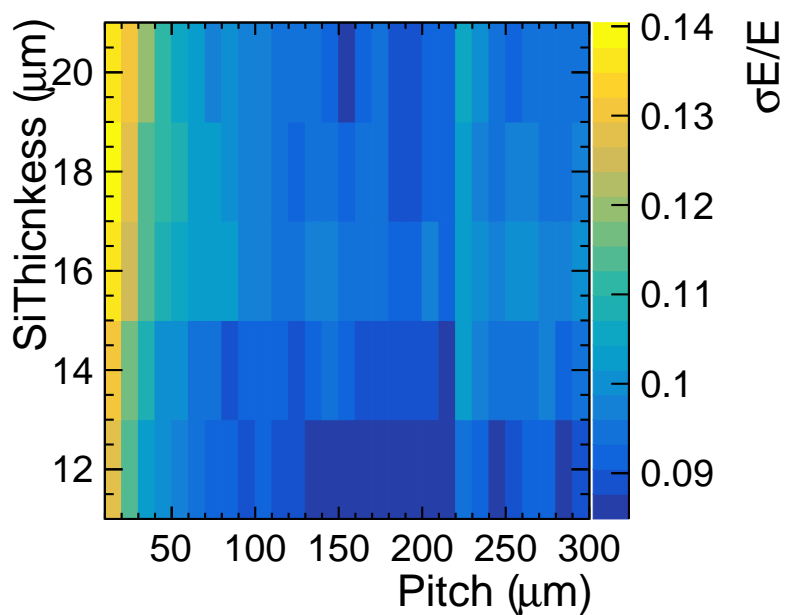


Figure 6.20: Energy resolution for 10 GeV photons after DigiMAPS is applied but without clustering.

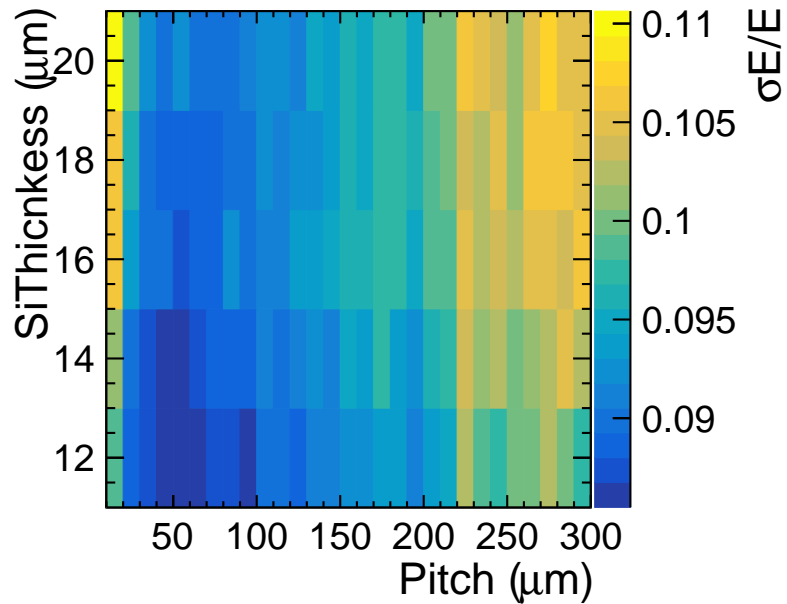


Figure 6.21: Energy resolution for 10 GeV photons after DigiMAPS is applied.

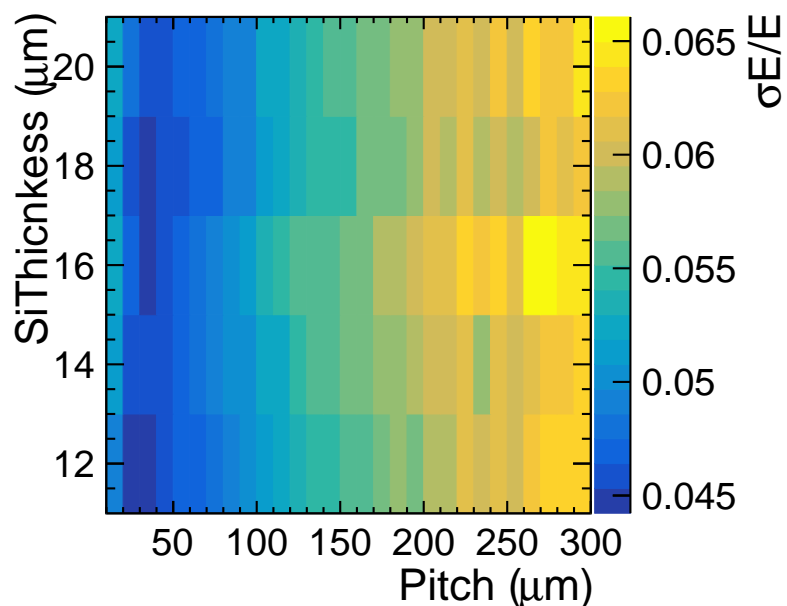


Figure 6.22: Energy resolution for 50 GeV photons after DigiMAPS is applied.

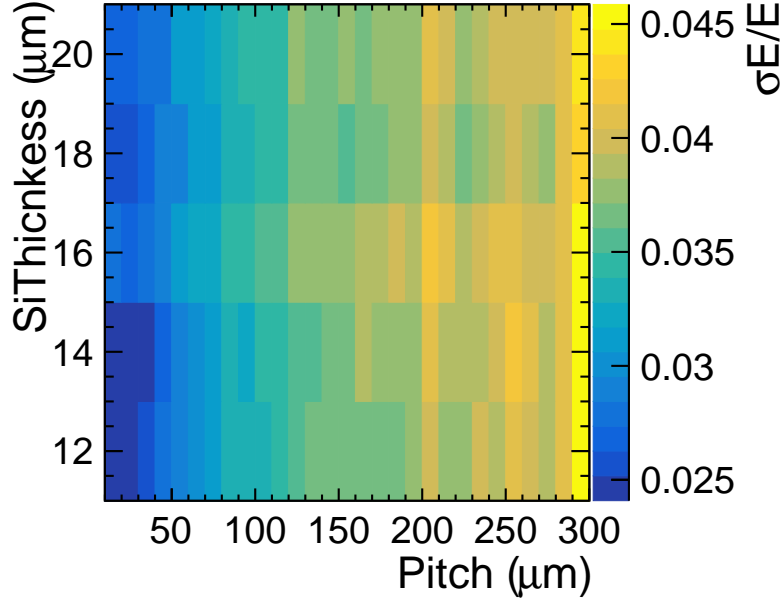


Figure 6.23: Energy resolution for 250 GeV photons after DigiMAPS is applied.

clustering. This is to be expected as in Figure 6.16 it is observed that the effects other than clustering and charge spread approximately cancel each other out.

The shift in the optimal region when performing clustering is due to a combination of effects. Firstly the clustering will be helping to remove excess hits from boundary crossings which normally pushes the optimal point towards wider pixel pitches. Secondly, for wider pixels it is more likely that two adjacent pixels will have genuine contributions from the EM shower which can be merged by the clustering algorithm leading to undercounting. Both of these effects act to make the resolution better for narrower pixels and worse for wider pixels. One can see that at 250 GeV the optimal working point now corresponds to pixel ranges below what is considered within this study. For the typical energy scale for the ILC, ~ 50 GeV, the optimal pixel configuration is found to be at $30 \mu m$ pitch, $12 \mu m$ epi thickness as shown in Figure 6.22. The resulting resolution is found to be:

$$\frac{\sigma_E}{E} = \frac{16.1\%}{\sqrt{E}} \oplus \frac{0.5\%}{E} \oplus 0.4\% \quad (6.2)$$

This is comparable to the performance observed for the analogue SiW equivalent proposed for ILD which sees a resolution of $(16.6 \pm 0.1) / \sqrt{E(\text{GeV})} \oplus (1.1 \pm 0.1)\%$ noting that the effect of charge spread has not been included here.

6.5 Future Improvements

As we have already seen that the resolution is dominated by the effects of boundary crossings and saturation it is important to consider how these might be mitigated. It has already been shown the boundary crossings effects can be reduced by including clustering to group adjacent pixels together preventing overcounting, however no method has been shown for reducing the saturation. One possible solution would be to change to a semi digital design in which multiple threshold level were present per pixel. This would require a slightly more sophisticated pixel design but could provide some power for distinguishing pixels through which only one particle has passed from those which have multiple contributions. It should also be noted that the studies presented here are still only using an adaptation of the existing ILD analogue ECAL design. It is unlikely that this represents the optimal design for a digital calorimeter. In particular, a DECAL might benefit from changing the absorbing material to one with a larger Moliere radius to produce a less dense shower and so less saturation. While this should provide a better single particle resolution, it may result in a worse jet resolution as showers could start to overlap. As such, further study is required to find the optimal material choices for a DECAL.

While the studies here allow considerable progress to be made in designing a digital calorimeter, there is still much to be done to fully evaluate how it could perform as part of a full detector. In particular for simulation studies additional effects must be considered such as magnetic fields and angular dependencies. Currently all events are simulated with no magnetic field and with all particles entering the ECAL at an angle of 90° . This suppresses any angular dependence on the performance of the DECAL. For example, the angle at which a particle enters the detector will change

the amount of material traversed in both the absorber and active layers, effectively changing the number of interaction lengths a particle will see per layer. This can lead to miscounting of the number of particles passing through the detector. This is not as big an issue for analogue calorimeters where the energy of the hits are measured and scaled by a sampling fraction which is relatively insensitive to the angle of the incident particle. Regarding the magnetic field, additional complications can arise from low momentum particles being trapped between active layers and so not leaving sufficient hits in the detector, or from higher momentum particles being curved back into layers they have already traversed causing extra hits to be recorded.

Ideally the effect of charge spreading should be considered in performing the design optimization. As seen in Figure 6.16 this can cause a large effect on the energy resolution however this had to be ignored in the optimization studies due to the inability to perform the necessary sub pixel simulations with DigiMAPS. However examining the effect of charge spread would require a dedicated optimization study of its own as there are multiple diode configurations which could be used with the optimal diode layout ultimately depending on the pixel dimensions itself. As such it makes more sense to settle on an optimal pixel geometry first and then design the pixel substructure to maximise the charge collection efficiency for this geometry.

In the longer term the ultimate aim will be to implement the DECAL into the particle flow algorithms used for ILD. At the beginning of this chapter it was postulated that the higher granularity of the DECAL could improve particle flow performance however without implementing this the scale of any improvements cannot be known.

6.6 Conclusion

Here we have examined the potential for implementing a digital calorimeter within the ILD geometry by studying the single particle energy resolution for various pixel pitches and epitaxial thicknesses. Initially studies were performed by simplying measuring raw energy deposits within the calorimeter as determined by GEANT4.

This allowed the two main driving factors for optimizing the pixel configuration to be identified. For lower energy scales the resolution is dominated by boundary crossings where a single particle passes through multiple pixels within one layer leading to an overestimate of the number of particles in the shower and so a wider, shallower pixel is preferred. At higher energies the resolution is dominated by saturation effects where the number of particles in the shower is underestimated due to the EM shower being denser than the granularity of the detector and so narrower pixels provide better performance. Following this, studies were performed using the DigiMAPS package to add additional levels of realism to the simulations. In particular this allowed effects such as charge diffusion, dead space, noise, threshold spreads and clustering to be examined. The combined impact of these additional effects (neglecting the charge spread due to computational restraints) on the energy resolution was studied as a function of pixel pitch and epitaxial layer thickness. Overall the resolution was found to be degraded by the effects of threshold spread and dead space however this was balanced out by the effect of pixel noise which improved the resolution by pushing the energy deposits from tracks to above the threshold applied. The most dominant of the added effects was found to be the clustering, which resulted in a net improvement in the energy resolution by removing excess hits caused by boundary crossings. This resulted in the optimal pixel configuration moving to narrower pixels than were preferred before the clustering is applied. For the maximum energy expected at ILC, 250 GeV, the optimal working point was found to be outside the range studied here, $< 10 \mu m$. However, for the typical energy scale of particles at the ILC, 50 GeV, the optimal resolution was found to occur for $30 \mu m$ pitch, $12 \mu m$ epi thickness pixels. This configuration gave a net resolution of:

$$\frac{\sigma_E}{E} = \frac{16.1\%}{\sqrt{E}} \oplus \frac{0.5\%}{E} \oplus 0.4\% \quad (6.3)$$

Which is comparable to the performance seen for the fully optimised design of the analogue SiW intended for use in ILD.

CHAPTER 7

Conclusion

With the growing need to decide upon which future colliders should be built to ensure a smooth transition post LHC, it is vital that the relative merits of each proposed collider are examined. Here we have presented the potential impact that a lepton collider such as CLIC can have on precision measurements of the standard model. In the Higgs sector we have shown how the combination of several measurements can provide access to model independent measurements of the Higgs couplings, something not possible at hadron colliders. In particular we have shown how one of these measurements, $\sigma_{H\nu\bar{\nu}} \times BR(H \rightarrow WW^*)$, might be performed at 1.4 TeV using the semileptonic decay channel and collecting 1.5 ab^{-1} of data. This yielded an expected precision of:

$$\delta\sigma_{H\nu\bar{\nu}} \times BR(H \rightarrow WW^*) = 1.34\%_{Stat} \oplus 1.37\%_{Syst}$$

Combining this with measurements performed with the fully hadronic channel shows an expected statistical precision of 1.0%, typical of what can be expected for many

Energy (GeV)	$A_{FB}^t \pm \text{Stat.} \oplus \text{Syst.}$	$\sigma \pm \text{Stat.} \oplus \text{Syst.}$
<hr/>		
P(e ⁻)=-80%		
>=1200	$0.563 \pm 0.018 \oplus 0.015$	$18.41 \pm 0.37 \oplus 0.29$
900-1200	$0.546 \pm 0.034 \oplus 0.028$	$11.01 \pm 0.38 \oplus 0.31$
400-900	$0.458 \pm 0.081 \oplus 0.032$	$16.56 \pm 1.31 \oplus 0.48$
<hr/>		
P(e ⁻)=+80%		
>=1200	$0.621 \pm 0.024 \oplus 0.016$	$9.84 \pm 0.28 \oplus 0.14$
900-1200	$0.588 \pm 0.045 \oplus 0.027$	$5.87 \pm 0.29 \oplus 0.14$
400-900	$0.514 \pm 0.105 \oplus 0.034$	$8.63 \pm 0.83 \oplus 0.19$

Table 7.1: Final summary of the expected precisions attainable from the $t\bar{t}$ analysis.

measurements of Higgs properties at CLIC.

A study measuring the top forward backward asymmetry and $t\bar{t}$ cross section was also shown as a means of probing the ttX vertex for hints of BSM physics contributions. This study was performed under the assumption that CLIC would operate with an even luminosity split between operation with an electron beam polarization of +80% and -80%. Due to the energy and polarization dependence of A_{FB}^t and $\sigma_{t\bar{t}}$ and the presence of a large tail in the energy spectrum of collisions at CLIC, the analysis was performed in six bins corresponding to the combinations of two polarization states and three energy ranges to maximise the information extracted. Event reconstruction and selection was performed using techniques based on fat jet and jet substructure which have not been implemented in a lepton collider before. Ultimately the final results were extracted by performing a second order polynomial fit to the distribution of the top production angle. The resulting uncertainties for each bin are shown in Table 7.1 and are found to be approximately an order of magnitude better than what is seen at the LHC[62]. A detailed study of various systematic effects revealed that the in all cases the uncertainty is dominated by the statistical component with the dominant systematic contributions for the cross section and A_{FB}^t coming from the background normalization and bias introduced during efficiency corrections respectively. In future these results will be combined

with measurements from other top studies performed by CLIC to evaluate the precision to which the electroweak form factors of the ttX can be measured.

Lastly we have examined the possibility for using a DECAL at the ILC as an alternative to the analogue SiW calorimeter. Such a device would use CMOS MAPS technology to provide an ultra high granularity capable of measuring every particle present within an EM shower providing potential benefits for use with particle flow techniques and potential cost reductions. The resolution of a DECAL was found to be dominated by two competing effects. At low energy boundary crossings dominate leading to a worse performance for designs based on narrower, deeper pixels. For higher energy saturation occurs as the EM shower becomes denser than the detectors granularity leading to worse performance for wider pixels. When using DigiMAPS to apply additional levels of realism such as charge diffusion, dead space, noise, threshold spreads and clustering it was found that the clustering helped mitigate the impact of boundary crossings leading to a general performance for narrow pixels thin pixels. For the typical enegy scale of the ILC the optimal piuxel desgin was found to occur when using $30 \mu m$ pitch, $12 \mu m$ epi thickness pixels. This design yielded an energy resolution of:

$$\frac{\sigma_E}{E} = \frac{16.1\%}{\sqrt{E}} \oplus \frac{0.5\%}{E} \oplus 0.4\% \quad (7.1)$$

Which is comparable to the performance seen for the fully optimised design of the analogue SiW intended for use in ILD.

REFERENCES

- [1] H. Abramowicz *et al.*, “Higgs physics at the CLIC electronpositron linear collider,” *Eur. Phys. J.*, vol. C77, no. 7, p. 475, 2017.
- [2] H. et al, “Top quark physics at the clic electron positron collider,” *Paper in Preparation*, 2018.
- [3] G. Aad *et al.*, “Observation of a new particle in the search for the Standard Model Higgs boson with the ATLAS detector at the LHC,” *Phys. Lett. B*, 2012.
- [4] S. Chatrchyan *et al.*, “Observation of a new boson at a mass of 125 GeV with the CMS experiment at the LHC,” *Phys. Lett.*, vol. B716, pp. 30–61, 2012.
- [5] V. Khachatryan *et al.*, “Precise determination of the mass of the Higgs boson and tests of compatibility of its couplings with the standard model predictions using proton collisions at 7 and 8 TeV,” *Eur. Phys. J.*, vol. C75, no. 5, p. 212, 2015.
- [6] G. Aad *et al.*, “Measurements of the Higgs boson production and decay rates and coupling strengths using pp collision data at $\sqrt{s} = 7$ and 8 TeV in the ATLAS experiment,” *Eur. Phys. J.*, vol. C76, no. 1, p. 6, 2016.
- [7] G. Aad *et al.*, “Measurements of the Higgs boson production and decay rates and constraints on its couplings from a combined ATLAS and CMS analysis of the LHC pp collision data at $\sqrt{s} = 7$ and 8 TeV,” *JHEP*, vol. 08, p. 045, 2016.
- [8] V. Trimble, “Existence and Nature of Dark Matter in the Universe,” *Ann. Rev. Astron. Astrophys.*, vol. 25, pp. 425–472, 1987.
- [9] C. Patrignani *et al.*, “Review of Particle Physics,” *Chin. Phys.*, vol. C40, no. 10, p. 100001, 2016.

- [10] H. Baer, V. Barger, P. Huang, D. Mickelson, A. Mustafayev, and X. Tata, “Radiative natural supersymmetry: Reconciling electroweak fine-tuning and the Higgs boson mass,” *Phys. Rev.*, vol. D87, no. 11, p. 115028, 2013.
- [11] S. Dawson *et al.*, “Working Group Report: Higgs Boson,” in *Proceedings, 2013 Community Summer Study on the Future of U.S. Particle Physics: Snowmass on the Mississippi (CSS2013): Minneapolis, MN, USA, July 29-August 6, 2013*, 2013.
- [12] K. Fujii *et al.*, “Physics Case for the International Linear Collider,” *arXiv:1506.05992 [hep-ex]*, 2015.
- [13] M. Bogomilov *et al.*, “Lattice design and expected performance of the Muon Ionization Cooling Experiment demonstration of ionization cooling,” *Phys. Rev. Accel. Beams*, vol. 20, no. 6, p. 063501, 2017.
- [14] M. J. Boland *et al.*, “Updated baseline for a staged Compact Linear Collider,” 2016.
- [15] T. Behnke, J. E. Brau, B. Foster, J. Fuster, M. Harrison, J. M. Paterson, M. Peskin, M. Stanitzki, N. Walker, and H. Yamamoto, “The International Linear Collider Technical Design Report - Volume 1: Executive Summary,” 2013.
- [16] R. Lipton, “Muon Collider: Plans, Progress and Challenges,” in *Particles and fields. Proceedings, Meeting of the Division of the American Physical Society, DPF 2011, Providence, USA, August 9-13, 2011*, 2012.
- [17] M. Koratzinos, “FCC-ee accelerator parameters, performance and limitations,” in *International Conference on High Energy Physics 2014 (ICHEP 2014) Valencia, Spain, July 2-9, 2014*, 2014.
- [18] C.-S. S. Group, “CEPC-SPPC Preliminary Conceptual Design Report. 1. Physics and Detector,” 2015.
- [19] T. Behnke, J. E. Brau, B. Foster, J. Fuster, M. Harrison, J. M. Paterson, M. Peskin, M. Stanitzki, N. Walker, and H. Yamamoto, “The International Linear Collider Technical Design Report - Volume 1: Executive Summary,” *arXiv:1306.6327 [physics.acc-ph]*, 2013.
- [20] P. Lebrun, L. Linssen, A. Lucaci-Timoce, D. Schulte, F. Simon, S. Stapnes, N. Toge, H. Weerts, and J. Wells, “The CLIC Programme: Towards a Staged e+e- Linear Collider Exploring the Terascale : CLIC Conceptual Design Report,” *arXiv:1209.2543 [physics.ins-det]*, Sept. 2012.
- [21] W. Kilian, T. Ohl, and J. Reuter, “WHIZARD: Simulating Multi-Particle Processes at LHC and ILC,” *Eur. Phys. J.*, vol. C71, p. 1742, 2011.
- [22] S. Jadach, J. H. Kuhn, and Z. Was, “TAUOLA: A Library of Monte Carlo programs to simulate decays of polarized tau leptons,” *Comput. Phys. Commun.*, vol. 64, pp. 275–299, 1990.

- [23] T. Sjostrand, S. Mrenna, and P. Z. Skands, “PYTHIA 6.4 Physics and Manual,” *JHEP*, vol. 05, p. 026, 2006.
- [24] P. Mora de Freitas and H. Videau, “Detector simulation with MOKKA / GEANT4: Present and future,” in *Linear colliders. Proceedings, International Workshop on physics and experiments with future electron-positron linear colliders, LCWS 2002, Seogwipo, Jeju Island, Korea, August 26-30, 2002*, pp. 623–627, 2002.
- [25] M. Thomson, “Particle flow calorimetry and the pandorapfa algorithm,” *Nuclear Instruments and Methods in Physics Research Section A: Accelerators, Spectrometers, Detectors and Associated Equipment*, vol. 611, no. 1, pp. 25 – 40, 2009.
- [26] T. Abe *et al.*, “The International Large Detector: Letter of Intent,” 2010.
- [27] H. Aihara, P. Burrows, M. Oreglia, E. L. Berger, V. Guarino, J. Repond, H. Weerts, L. Xia, J. Zhang, Q. Zhang, *et al.*, “SiD Letter of Intent,” 2009.
- [28] Y. Giomataris, P. Rebougeard, J. P. Robert, and G. Charpak, “MICROMEGAS: A High granularity position sensitive gaseous detector for high particle flux environments,” *Nucl. Instrum. Meth.*, vol. A376, pp. 29–35, 1996.
- [29] F. Sauli, “GEM: A new concept for electron amplification in gas detectors,” *Nucl. Instrum. Meth.*, vol. A386, pp. 531–534, 1997.
- [30] D. E. Groom, “Passage of particles through matter: in Review of Particle Physics (RPP 1998),” *Eur. Phys. J.*, vol. C3, pp. 144–151, 1998.
- [31] J. Beringer *et al.*, “Review of Particle Physics (RPP),” *Phys. Rev.*, vol. D86, p. 010001, 2012.
- [32] J. A. Ballin, R. Coath, J. P. Crooks, P. D. Dauncey, A.-M. Magnan, Y. Mikami, O. D. Miller, M. Noy, V. Rajovic, M. Stanitzki, K. D. Stefanov, R. Turchetta, M. Tyndel, E. G. Villani, N. K. Watson, J. A. Wilson, and Z. Zhang, “Design and performance of a CMOS study sensor for a binary readout electromagnetic calorimeter,” *Journal of Instrumentation*, vol. 6, p. 5009, May 2011.
- [33] I. Bozovic-Jelisavcic, H. Abramowicz, P. Bambade, T. Jovin, M. Pandurovic, B. Pawlik, C. Rimbault, I. Sadeh, and I. Smiljanic, “Luminosity Measurement at ILC,” 2010.
- [34] F. Pitters, “The CLIC Detector Concept,” 2018.
- [35] M. Szleper, “The Higgs boson and the physics of WW scattering before and after Higgs discovery,” 2014.
- [36] P. W. Higgs, “Broken symmetries and the masses of gauge bosons,” *Phys. Rev. Lett.*, vol. 13, pp. 508–509, Oct 1964.

- [37] F. Englert and R. Brout, “Broken symmetry and the mass of gauge vector mesons,” *Phys. Rev. Lett.*, vol. 13, pp. 321–323, Aug 1964.
- [38] C. Durig, K. Fujii, J. List, and J. Tian, “Model Independent Determination of HWW coupling and Higgs total width at ILC,” in *International Workshop on Future Linear Colliders (LCWS13) Tokyo, Japan, November 11-15, 2013*, 2014.
- [39] “Measurements of the Higgs boson production and decay rates and constraints on its couplings from a combined ATLAS and CMS analysis of the LHC pp collision data at $\sqrt{s} = 7$ and 8 TeV,” Tech. Rep. ATLAS-CONF-2015-044, CERN, Geneva, Sep 2015.
- [40] “Projected Performance of an Upgraded CMS Detector at the LHC and HL-LHC: Contribution to the Snowmass Process,” in *Proceedings, 2013 Community Summer Study on the Future of U.S. Particle Physics: Snowmass on the Mississippi (CSS2013): Minneapolis, MN, USA, July 29-August 6, 2013*, 2013.
- [41] P. Langacker, “The Physics of Heavy Z' Gauge Bosons,” *Rev. Mod. Phys.*, vol. 81, pp. 1199–1228, 2009.
- [42] M. S. Amjad *et al.*, “A precise characterisation of the top quark electro-weak vertices at the ILC,” *Eur. Phys. J.*, vol. C75, no. 10, p. 512, 2015.
- [43] G. A. et al, “Measurement of the b quark forwardbackward asymmetry around the z_0 peak using an inclusive tag,” *Physics Letters B*, vol. 546, no. 1, pp. 29 – 47, 2002.
- [44] S. Schael *et al.*, “Precision electroweak measurements on the Z resonance,” *Phys. Rept.*, vol. 427, pp. 257–454, 2006.
- [45] C. R. Schmidt, “Top quark production and decay at next-to-leading order in $e+ e-$ annihilation,” *Phys. Rev.*, vol. D54, pp. 3250–3265, 1996.
- [46] D. Schulte, “Beam-Beam Simulations with GUINEA-PIG,” Mar 1999.
- [47] “Monte carlo samples for clic higgs studies.”
- [48] M. Cacciari, G. P. Salam, and G. Soyez, “FastJet User Manual,” *Eur. Phys. J.*, vol. C72, p. 1896, 2012.
- [49] T. Suehara and T. Tanabe, “LCFIPlus: A Framework for Jet Analysis in Linear Collider Studies,” *Nucl. Instrum. Meth.*, vol. A808, pp. 109–116, 2016.
- [50] A. Hoecker, P. Speckmayer, J. Stelzer, J. Therhaag, E. von Toerne, H. Voss, M. Backes, T. Carli, O. Cohen, A. Christov, D. Dannheim, K. Danielowski, S. Henrot-Versille, M. Jachowski, K. Kraszewski, A. Krasznahorkay, Jr., M. Kruk, Y. Mahalalel, R. Ospanov, X. Prudent, A. Robert, D. Schouten, F. Tegenfeldt, A. Voigt, K. Voss, M. Wolter, and A. Zemla, “TMVA - Toolkit for Multivariate Data Analysis,” *ArXiv Physics e-prints*, Mar. 2007.

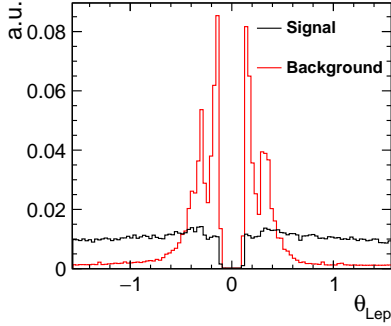
- [51] Y. Coadou, “Boosted Decision Trees and Applications,” *EPJ Web Conf.*, vol. 55, p. 02004, 2013.
- [52] A. Muennich, “TauFinder: A Reconstruction Algorithm for Tau Leptons at Linear Colliders,” Oct 2010.
- [53] “CLIC Conceptual Design Report: Physics and Detectors at CLIC,” 2012.
- [54] D. W. Miller, “Jet substructure in ATLAS,” in *Particles and fields. Proceedings, Meeting of the Division of the American Physical Society, DPF 2011, Providence, USA, August 9-13, 2011*, 2011.
- [55] M. Cacciari, G. P. Salam, and G. Soyez, “The Anti-k(t) jet clustering algorithm,” *JHEP*, vol. 04, p. 063, 2008.
- [56] M. Boronat, J. Fuster, I. Garcia, E. Ros, and M. Vos, “A robust jet reconstruction algorithm for high-energy lepton colliders,” *Phys. Lett.*, vol. B750, pp. 95–99, 2015.
- [57] J. Thaler and K. Van Tilburg, “Identifying Boosted Objects with N-subjettiness,” *JHEP*, vol. 03, p. 015, 2011.
- [58] D. Krohn, T. Liu, J. Shelton, and L.-T. Wang, “A Polarized View of the Top Asymmetry,” *Phys. Rev.*, vol. D84, p. 074034, 2011.
- [59] B. List and J. List, “MarlinKinfit: An Object–Oriented Kinematic Fitting Package,” *LC Notes*, 2009.
- [60] J. Jersák, E. Laermann, and P. M. Zerwas, “Electroweak production of heavy quarks in e^+e^- annihilation,” *Phys. Rev. D*, vol. 25, pp. 1218–1228, Mar 1982.
- [61] J. Fleischer, A. Leike, T. Riemann, and A. Werthenbach, “Electroweak one loop corrections for e+ e- annihilation into t anti-top including hard bremsstrahlung,” *Eur. Phys. J.*, vol. C31, pp. 37–56, 2003.
- [62] Y. Bai and Z. Han, “Improving the Top Quark Forward-Backward Asymmetry Measurement at the LHC,” *JHEP*, vol. 02, p. 135, 2012.
- [63] J. A. Ballin, J. P. Crooks, P. D. Dauncey, A. . Magnan, Y. Mikami, O. D. Miller, M. Noy, V. Rajovic, M. M. Stanitzki, K. D. Stefanov, R. Turchetta, M. Tyndel, E. G. Villani, N. K. Watson, and J. A. Wilson, “Monolithic Active Pixel Sensors (MAPS) in a quadruple well technology for nearly 100% fill factor and full CMOS pixels,” *ArXiv e-prints*, July 2008.
- [64] J. A. Ballin *et al.*, “TPAC: A 0.18 micron MAPS for digital electromagnetic calorimetry at the ILC,” in *Proceedings, 2008 IEEE Nuclear Science Symposium, Medical Imaging Conference and 16th International Workshop on Room-Temperature Semiconductor X-Ray and Gamma-Ray Detectors (NSS/MIC 2008 / RTSD 2008): Dresden, Germany, October 19-25, 2008*, pp. 2224–2227, 2008.

- [65] J. Mylroie-Smith, S. Kolya, J. Velthuis, A. Bevan, G. Inguglia, J. Headspith, I. Lazarus, R. Lemon, J. Crooks, R. Turchetta, and F. Wilson, "First tests of cherwell, a monolithic active pixel sensor: A cmos image sensor (cis) using 180nm technology," *Nuclear Instruments and Methods in Physics Research Section A: Accelerators, Spectrometers, Detectors and Associated Equipment*, vol. 731, pp. 137 – 140, 2013. PIXEL 2012.
- [66] T. Price *et al.*, "First radiation hardness results of the TeraPixel Active Calorimeter (TPAC) sensor," *JINST*, vol. 8, p. P01007, 2013.

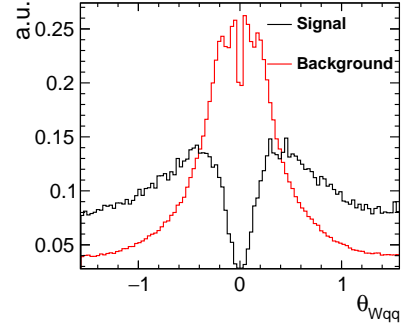
Appendices

.1 Appendix A: Higgs Results

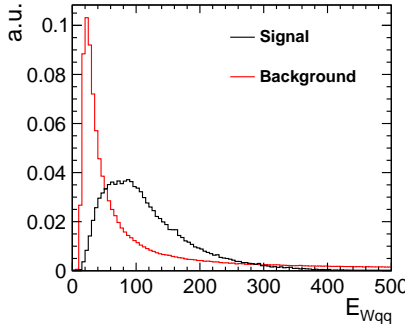
Here we show the signal and background distributions for the input variables used for training the BDT for our Higgs analysis. In all cases the plots are normalised to unity and show the raw distributions before preselection cuts are applied.



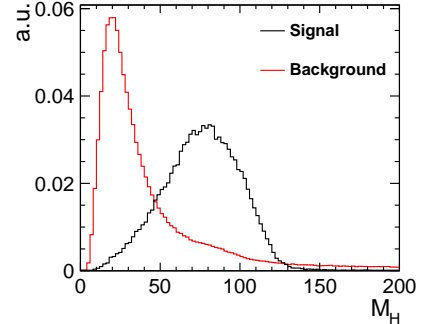
(a) Angle of lepton relative to beam axis



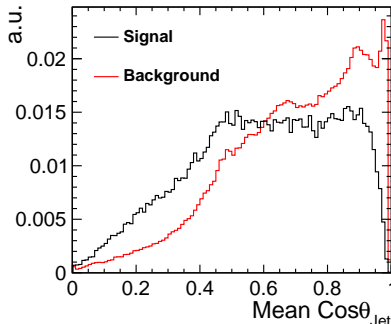
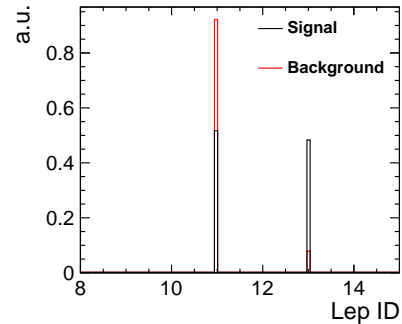
(b) Angle of W relative to beam axis



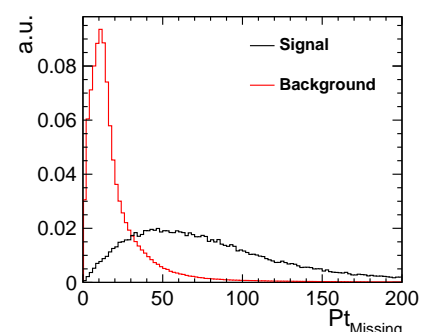
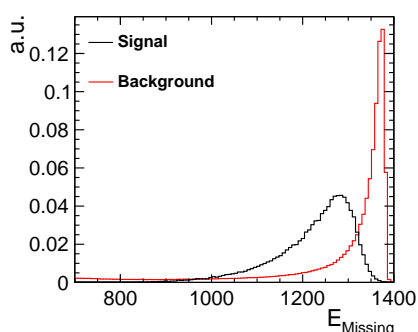
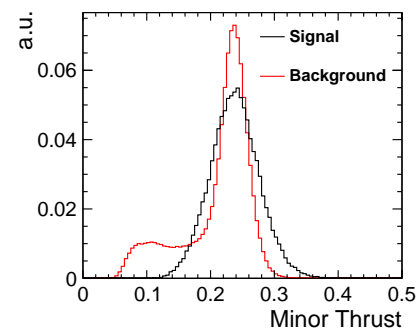
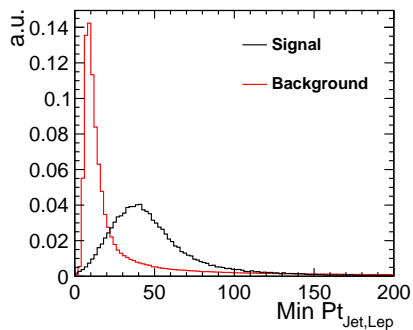
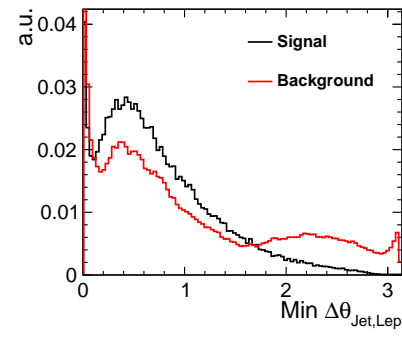
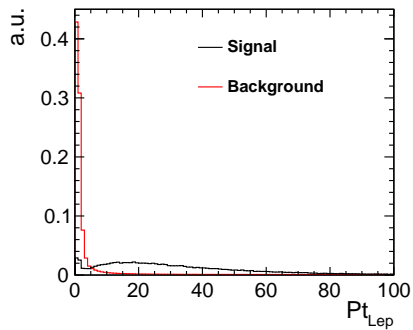
(c) Energy of hadronically decaying W

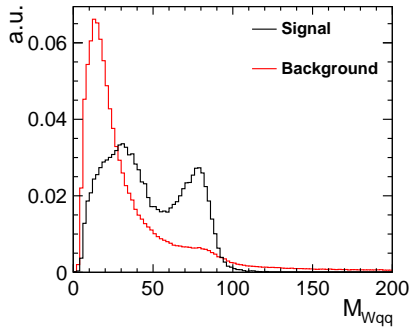
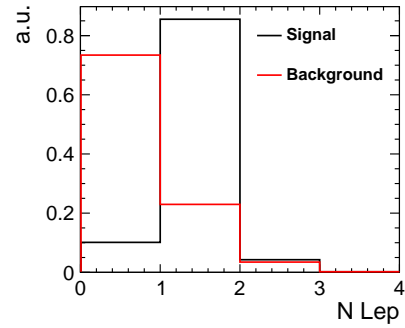


(d) Reconstructed Higgs mass

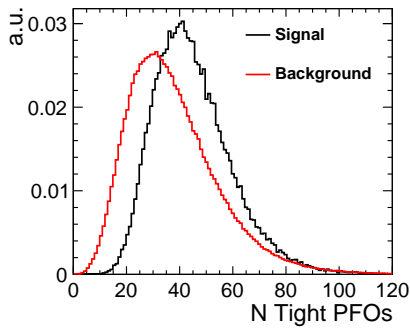
(e) Average $\cos\theta$ of jets

(f) Lepton PID

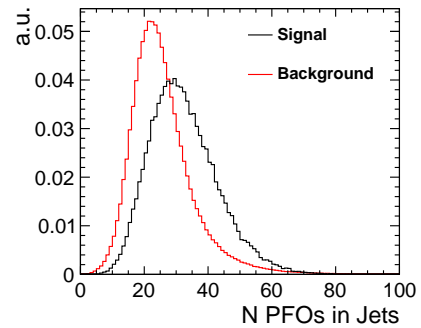



 (m) Mass of hadronically decaying W


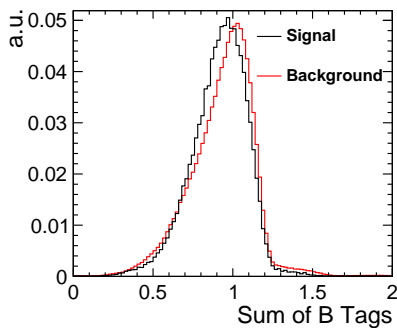
(n) Number of reconstructed leptons



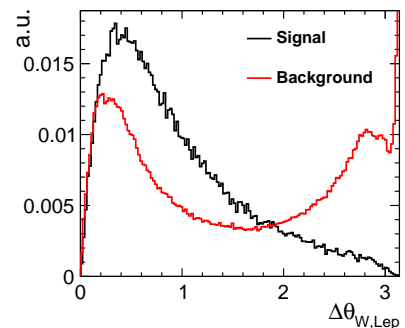
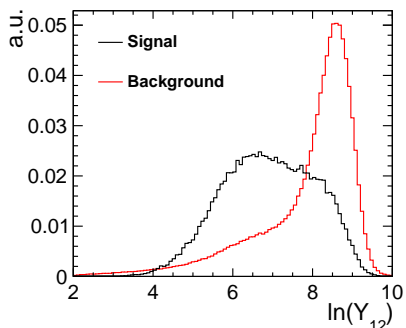
(o) nPFOs passing tight timing cuts

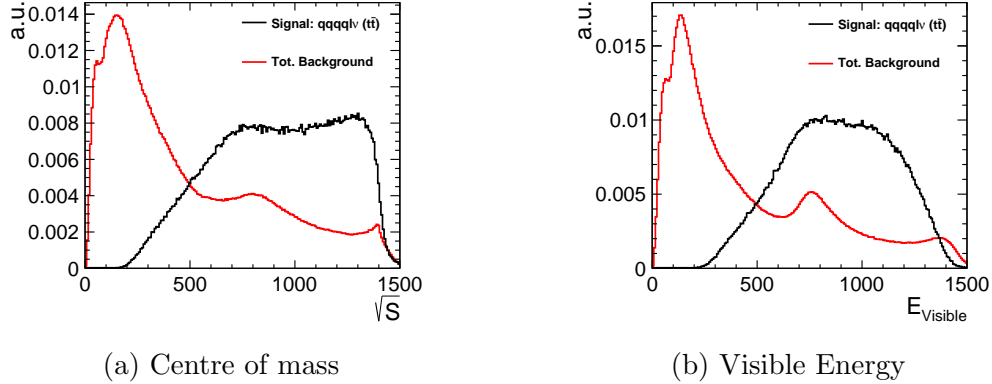


(p) nPFOs assigned to jets



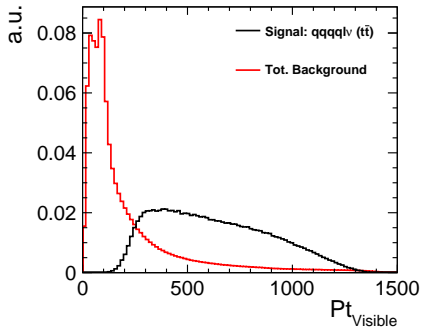
(q) Sum of two highest b-tags


 (r) Angular Separation of the W and lepton

 (s) Jet Resolution Parameter Y_{12}

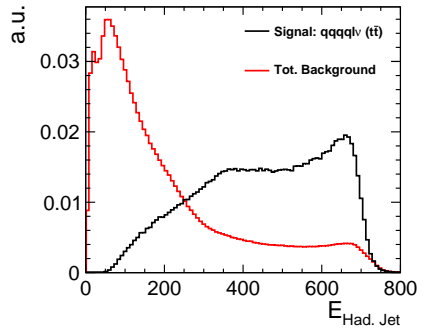


.2 Appendix B: Top Results

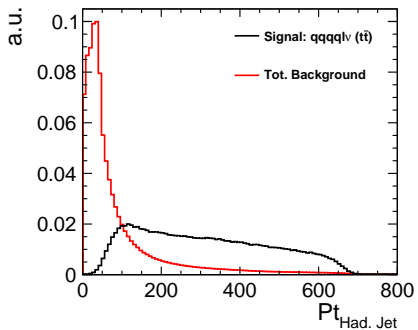
Here we show the signal and background distributions for the input variables used for training the BDT for our top analysis. In all cases the plots are normalised to unity and show the raw distributions before preselection cuts are applied. Efficiencies for the lower $\sqrt{S'}$ bins following each stage of selection are also shown.



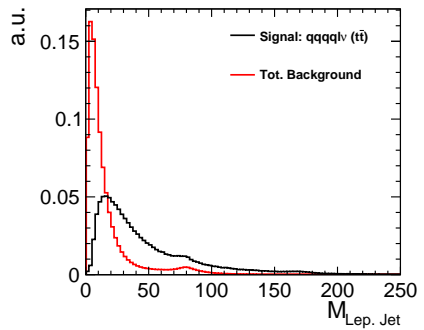
(c) Visible Transverse Momentum



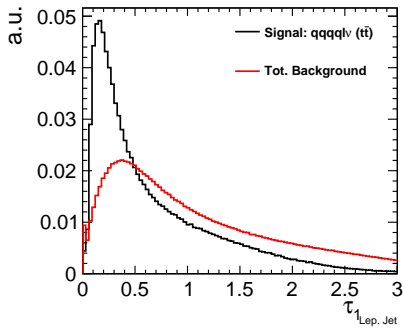
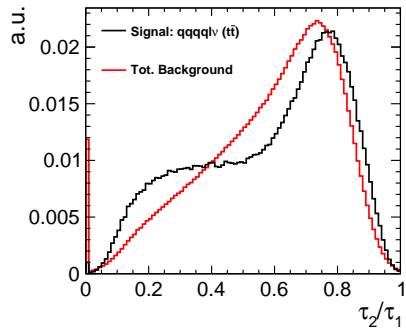
(d) Energy of hadronic fat jet

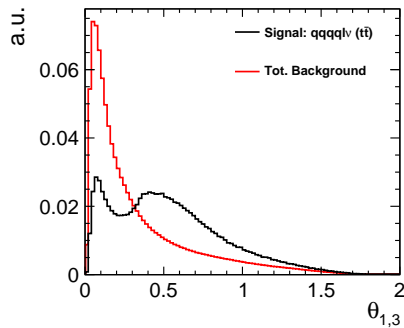
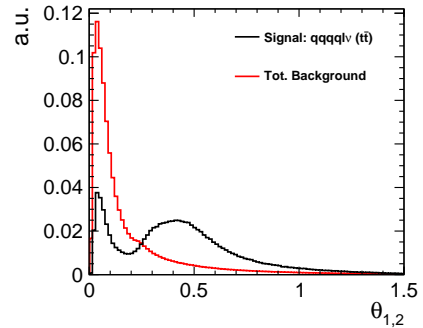
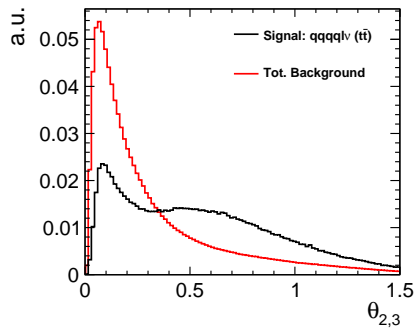
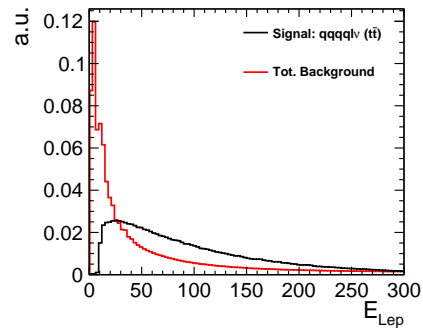


(e) Transverse momentum of hadronic fat jet

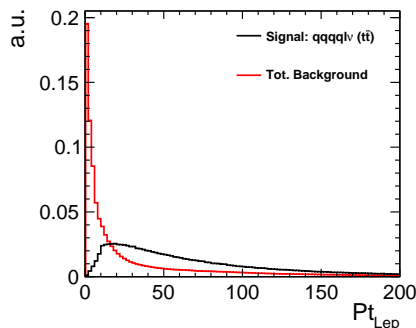


(f) Mass of leptonic fat jet

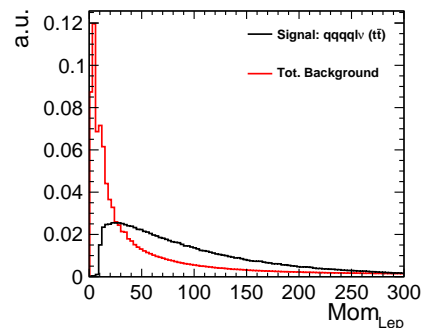

 (g) Leptonic fat jet τ_1

 (h) Leptonic fat jet τ_2/τ_1

(i) $\theta_{1,3}$ (j) $\theta_{1,2}$ (k) $\theta_{2,3}$ 

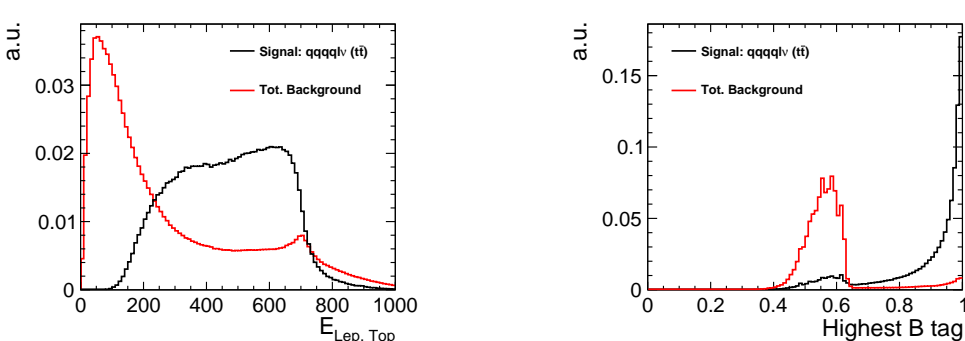
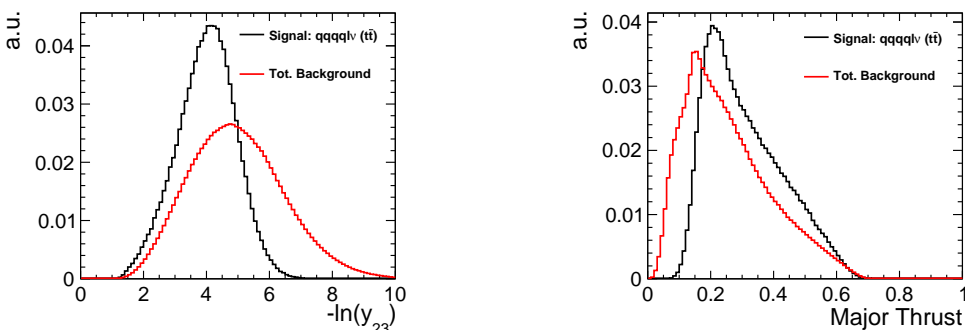
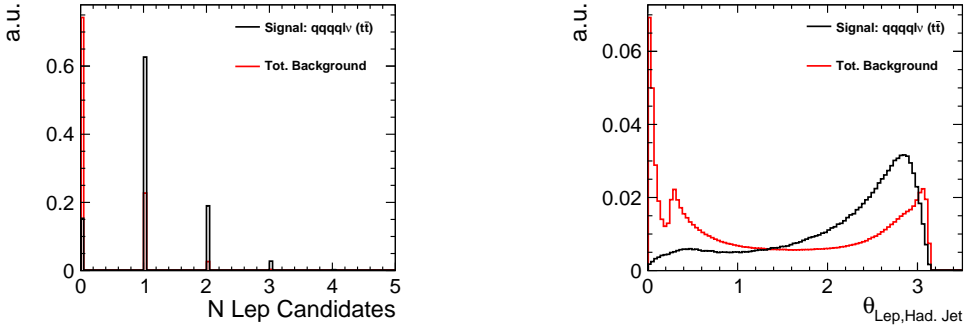
(l) Lepton Energy

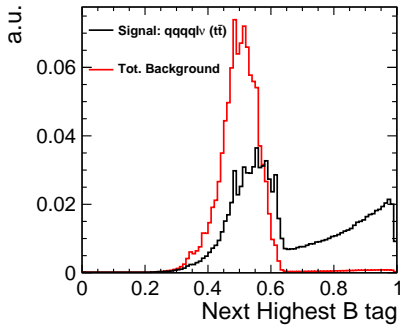


(m) Lepton transverse momentum



(n) Lepton momentum





(u) Second Highest B tag

Process	Cross Section (fb)	Efficiency Presel. & Quality	Efficiency BDT	N Expected
$e^+e^- \rightarrow t\bar{t} \rightarrow qqqql\nu (l = e, \mu)$				
900 < E < 1200 GeV	11.0	3.33E-1	2.85E-1	2350
E < 900, E >= 1200 GeV	35.8	6.31E-2	5.03E-2	1250
$e^+e^- \rightarrow t\bar{t} \rightarrow qqqql\nu (l = \tau)$	23.2	1.03E-1	3.55E-2	620
$e^+e^- \rightarrow t\bar{t} \rightarrow qqqql\nu (\text{non } t\bar{t})$	72.3	3.71E-2	1.83E-2	990
$e^+e^- \rightarrow qqqqqq$	116.4	2.45E-2	1.95E-3	170
$e^+e^- \rightarrow qql\nu l\nu$	44.1	3.00E-2	1.87E-2	620
$e^+e^- \rightarrow qqqq$	2304.0	2.39E-3	5.23E-5	90
$e^+e^- \rightarrow qql\nu$	6975.0	4.17E-4	1.33E-5	70
$e^+e^- \rightarrow qql l$	2681.0	2.40E-4	1.53E-5	30
$e^+e^- \rightarrow qq\nu\nu$	1395.0	9.10E-5	1.27E-5	10
$e^+e^- \rightarrow qq$	4843.0	1.83E-3	8.03E-5	290
TotalBackground	18500	1.60 E-3	3.06E-4	4246

Table 2: Efficiency for signal and background processes being classified as 900 < E < 1200 GeV following all stages of selection, and the expected number of events for 750 fb⁻¹ for -80% polarization

Process	Cross Section (fb)	Efficiency Presel. & Quality	Efficiency BDT	N Expected
$e^+e^- \rightarrow t\bar{t} \rightarrow qqqql\nu(l = e, \mu)$				
900<E<1200 GeV	5.8	3.02E-1	2.57E-1	1120
E<900, E>=1200 GeV	18.9	5.46E-2	4.45E-2	630
$e^+e^- \rightarrow t\bar{t} \rightarrow qqqql\nu(l = \tau)$	12.3	9.54E-2	2.62E-2	240
$e^+e^- \rightarrow t\bar{t} \rightarrow qqqql\nu(\text{non } t\bar{t})$	16.5	9.54E-2	3.27E-2	510
$e^+e^- \rightarrow qqqqqq$	44.9	2.80E-2	2.03E-3	70
$e^+e^- \rightarrow qql\nu l\nu$	15.3	4.84E-2	2.70E-2	310
$e^+e^- \rightarrow qqqq$	347.0	3.88E-3	1.24E-4	30
$e^+e^- \rightarrow qql\nu$	1644.0	2.08E-4	1.78E-5	20
$e^+e^- \rightarrow qql l$	2529.0	1.63E-4	1.11E-5	20
$e^+e^- \rightarrow qq\nu\nu$	180.0	1.62E-4	2.31E-5	3
$e^+e^- \rightarrow qq$	3169.0	1.42E-3	9.16E-5	220
TotalBackground	7980	1.56E-3	3.26E-4	1950

Table 3: Efficiency for signal and background processes being classified as 900<E<1200 GeV following all stages of selection and the expected number of events for 750 fb⁻¹ for +80% polarization

Process	Cross Section (fb)	Efficiency Presel. & Quality	Efficiency BDT	N Expected
$e^+e^- \rightarrow t\bar{t} \rightarrow qqqql\nu(l = e, \mu)$				
400 < E < 900 GeV	16.6	4.00E-2	3.62E-2	450
E < 400, E >= 900 GeV	30.2	4.90E-3	3.88E-3	90
$e^+e^- \rightarrow t\bar{t} \rightarrow qqqql\nu(l = \tau)$	23.2	6.49E-3	2.94E-3	50
$e^+e^- \rightarrow t\bar{t} \rightarrow qqqql\nu(\text{non } t\bar{t})$	72.3	4.16E-3	2.56E-3	140
$e^+e^- \rightarrow qqqqqq$	116.4	2.63E-3	4.51E-4	40
$e^+e^- \rightarrow qql\nu l\nu$	44.1	6.75E-3	4.90E-3	160
$e^+e^- \rightarrow qqqq$	2304.0	1.67E-4	7.65E-6	10
$e^+e^- \rightarrow qql\nu$	6975.0	5.14E-5	1.73E-6	10
$e^+e^- \rightarrow qll$	2681.0	4.09E-5	5.12E-6	10
$e^+e^- \rightarrow qq\nu\nu$	1395.0	1.09E-5	3.64E-6	4
$e^+e^- \rightarrow qq$	4843.0	1.53E-4	1.52E-5	60
TotalBackground	18500	1.52E-4	4.12E-5	570

Table 4: Efficiency for signal and background processes being classified as 400 < E < 900 GeV following all stages of selection, and the expected number of events for 750 fb⁻¹ for -80% polarization

Process	Cross Section (fb)	Efficiency Presel. & Quality	Efficiency BDT	N Expected
$e^+e^- \rightarrow t\bar{t} \rightarrow qqqql\nu(l = e, \mu)$				
400<E<900 GeV	8.7	5.00E-2	4.59E-2	300
E<400, E>=900 GeV	16.0	5.10E-3	4.17E-3	50
$e^+e^- \rightarrow t\bar{t} \rightarrow qqqql\nu(l = \tau)$	12.3	6.53E-3	3.27E-3	30
$e^+e^- \rightarrow t\bar{t} \rightarrow qqqql\nu(\text{non } t\bar{t})$	16.5	6.32E-3	4.63E-3	60
$e^+e^- \rightarrow qqqqqq$	44.9	2.89E-3	4.81E-4	20
$e^+e^- \rightarrow qql\nu l\nu$	15.3	1.33E-2	8.55E-3	100
$e^+e^- \rightarrow qqqq$	347.0	3.27E-4	4.67E-5	10
$e^+e^- \rightarrow qql\nu$	1644.0	4.36E-5	7.93E-6	10
$e^+e^- \rightarrow qql l$	2529.0	2.22E-5	5.54E-6	10
$e^+e^- \rightarrow qq\nu\nu$	180.0	1.16E-5	<E-6	10
$e^+e^- \rightarrow qq$	3169.0	7.40E-5	5.84E-6	10
TotalBackground	7970	1.35E-4	4.98E-5	300

Table 5: Efficiency for signal and background processes being classified as 400<E<900 GeV following all stages of selection and the expected number of events for 750 fb⁻¹ for +80% polarization